Direct Solar Absorption Nanofluids for Forward Osmosis Desalination

Muhammad Amjad

Submitted in accordance with the requirements for the degree of

Doctor of Philosophy

The University of Leeds

School of Chemical and Process Engineering

March 2018

The candidate confirms that the work submitted is his own, except where work which has formed part of jointly-authored publications has been included. The contribution of the candidate and the other authors to this work has been explicitly indicated below. The candidate confirms that appropriate credit has been given within the thesis where reference has been made to the work of others.

Acknowledgements

I would like to express my deepest gratitude to my supervisor Professor Dongsheng Wen for his continued encouragement, guidance and support for the realization of this research work. His timely and efficient feedback, suggestions and supervision helped me shape this work into its final form.

I am grateful to the University of Engineering and Technology, Lahore Pakistan for funding this research work.

I am thankful to Prof. Xiaoze Du, Prof. Jinaliang Xu and Prof. Leping Zhou from North China Electric Power University, Beijing for availing their research facilities and necessary support to do a part of the experiments. I also acknowledge the support from Dr. Ghulam Raza, Dr. Jabbar Gardy and Mr. Shahid Pervaiz for their continued help and support in the process of synthesis and characterization of the nanoparticles used in this work.

I am also thankful to my technical support team Peter Dawson, Susanne Patel, Ben Douglas, Robert Simpson and Diane Cochrane for their support during my research work at different occasions. I am also thankful to my research group members for their motivation, acknowledgement and appreciation of my work.

Finally, I am always indebted to my family for their understanding the importance of this work and supporting me in all ups and downs with encouragement, love, patience and prayers. I place on record, my sincere gratitude to my parents, wife, daughter and son for their patience, prayers, moral support and consistent encouragement throughout my work.

Abstract

Solar energy is the most abundant and easily accessible source of renewable energy, however, its efficient use is not an easy task. Absorption of solar energy directly by the working fluid is an emerging trend in solar collection, known as direct solar absorption. On the other hand, almost one-third of the world population is living in water stressed conditions and this figure is expected to increase to two-third in next ten years duration. Desalination of sea and brackish water and reclamation of wastewater is being progressively practiced worldwide to augment the limited potable water supplies through different techniques. Forward osmosis (FO) is an emerging desalination technology, which operates under the internal osmotic gradient across the FO membrane. Current FO technique lacks the availability of proper draw solutions that have high osmotic pressure, minimum reverse solute flux and easy regeneration.

This work develops a unique and novel concept of combining the solar energy, nanoparticles and FO to produce potable water in arid areas, far away from the grids. Two independent functions i.e. osmotic pressure and direct solar absorption are developed for the first time onto purposely formulated nanofluids for FO solar desalination. The direct solar absorptive nanofluid based novel draw solutions (NDS) are aimed at developing sufficiently high osmotic pressure for enhanced water flux across FO membrane and, at the same time, to absorb solar energy efficiently for their regeneration.

A number of nanofluids were formulated and characterized in terms of their morphology, structure and elemental composition. The characterized nanofluids were investigated experimentally for their direct solar absorption behaviour and FO

performance. A unique composite of direct absorptive nanofluid and osmotically active matter was developed that sufficiently performed the proposed two functions in FO solar desalination.

In direct solar absorption and steam generation experiments, nine nanofluids were examined and an enhancement in bulk photothermal efficiency (PTE) of about 95%, 100% and 105% over the base fluid was observed with gold, silver and carbon nanofiber (CNF) nanofluids respectively. The most absorptive carbon nanofiber based nanofluid was surface functionalized for osmotic pressure enhancement and experimented as NDS for FO performance in terms of osmotic pressure, water flux, reverse solute flux and water recovery. The NDS developed sufficient osmotic pressure and an enhancement of 80% in water flux was observed over 1M salt solution used as reference. The reverse solute flux of the NDS was negligible and the quality of product water was within the potable water standards.

The experimental results proved that the nanofluid based direct solar absorptive novel draw solutions can sufficiently develop osmotic pressure to permeate water across the FO membrane and can significantly enhance the potable water generation using solar energy. Moreover, the absence of nanoparticles in the product water and being its quality within the range of potable water standards, proved these novel draw solutions a potential candidate for future FO solar desalination in arid areas.

Keywords

Direct absorption, forward osmosis, draw solution, nanoparticle, desalination, solar energy

List of publications

- **Muhammad Amjad**, Ghulam Raza, Yan Xin, Shahid Pervaiz, Jinliang Xu, Xiaoze Du, and Dongsheng Wen, ‘Volumetric solar heating and steam generation via gold nanofluids’, Applied Energy, 206 (2017), 393-400.

The candidate as a primary author of this publication performed all the experiments and led the drafting of the publication. Yan Xin helped in setting up the experimental setup, Ghulam Raza and Shahid Pervaiz helped in synthesis and characterization of nanoparticles. Jinliang Xu and Xiaoze Du improved the review. Dongsheng Wen supervised the work, gave intensive suggestions in explaining the results and finalizing the paper.

- **Muhammad Amjad**, Yang Yang, Ghulam Raza, Hui Gao, Jun Zhang, Leping Zhou, Xiaoze Du, and Dongsheng Wen, 'Deposition Pattern and Tracer Particle Motion of Evaporating Multi-Component Sessile Droplets', Journal of Colloid and Interface Science, 506 (2017), 83-92.

The candidate as a primary author of this publication conceived the idea, performed all the experiments and led the drafting of the publication. The candidate and Ghulam Raza synthesized and characterized nanoparticles. Yang Yang calculated the particle velocity, Hui Gao and Jun Zhang helped in refining the review along with Leping Zhou and Xiaoze Du. Dongsheng Wen supervised the work, gave intensive suggestions in explaining the results, finalizing and proof reading the paper.

- **Muhammad Amjad**, Haichuan Jin, Xiaoze Du, and Dongsheng Wen, ‘Experimental photothermal performance of nanofluids under concentrated solar flux’, Solar Energy Materials and Solar Cells, 187 (2018),255-262.

- The candidate as a primary author of this publication formulated and characterized the nanofluids, performed all the experiments and led the drafting of the publication. Haichuan Jin performed some simulation and Xiaoze Du helped explaining the results and improving the discussion section. Dongsheng Wen supervised the work, gave intensive suggestions in explaining the results, finalizing and proof reading the paper.
- **Muhammad Amjad**, Aimen Zeiny, Ghulam Raza, Lizhan Bai, Zhongliang Hu, Dongsheng Wen, 'Photothermal conversion characteristics of direct solar absorption nanofluids', Joint Conference of 5th UK-China and 13th UK Particle Technology Forum Leeds, 12-15 July 2015, Leeds, UK.

The candidate as a primary author of this work, formulated the nanofluids, performed all the experiments and presented this work orally in the conference. Aimen Zeiny, Ghulam Raza, Lizhan Bai and Zhongliang Hu helped in characterizing the nanofluids and provided necessary support during the experimentation. Dongsheng Wen supervised the work.

- **Muhammad Amjad**, Ghulam Raza, Aimen Zeiny, Lizhan Bai, Dongsheng Wen, 'Effect of gold doping on photothermal conversion behaviour of TiO_2 for direct absorption solar collection', The 22nd Joint Annual Conference of CSCST and SCI, 19 September, 2015, Birmingham, UK.

The candidate as a primary author of this work, formulated the nanofluids, performed all the experiments and presented this work orally in the conference. Ghulam Raza, Aimen Zeiny and Lizhan Bai helped in characterizing the nanofluids and provided necessary support during the experimentation. Dongsheng Wen supervised the work.

- **Muhammad Amjad**, Ghulam Raza, Shahid Pervaiz, Haichuan Jin, Xiaoze Du, Dongsheng Wen, 'Experimental Investigation of Photothermal Conversion Characteristics of Metallic Nanofluids', The 9th International Symposium on Heat Transfer (ISHT-9), 15-19 August, 2016, Beijing, China.

The candidate as a primary author of this work, formulated the nanofluids, performed all the experiments and presented this work orally in the conference. Ghulam Raza, Shahid Pervaiz and Haichuan Jin helped in characterizing the nanofluids and provided necessary support during the experimentation. Xiaoze Du gave suggestions to explain the results and Dongsheng Wen supervised the work.

- **Muhammad Amjad**, Ghulam Raza, Shahid Pervaiz, Dongsheng Wen, 'Osmosis pressure enhancement of novel draw solutions for forward osmosis desalination', 3rd International Conference on Desalination using Membrane Technology, 2-5 April 2017, Gran Canaria, Spain.

The candidate as a primary author of this work performed all the experiments, analysed the data and presented this work orally in the conference. Ghulam Raza and Shahid Pervaiz supported in synthesizing and characterizing the nanofluids. Dongsheng Wen supervised the work and gave intensive suggestions in explaining the results.

Conference Posters

- **Muhammad Amjad**, Ghulam Raza, Shahid Pervaiz, Dongsheng Wen, 'Solar steam generation using direct absorbing nanoparticles', UK Particle Technology Forum organised by IChemE, held on 29 March 2017 in University of Birmingham, Birmingham, UK.

The candidate and Ghulam Raza formulated the nanoparticles and Shahid Pervaiz helped in characterizing the prepared suspension. The candidate performed all the experiments, analysed the data and presented this work as a poster in the conference. Dongsheng Wen supervised the work and gave intensive suggestions in explaining the results.

- **Muhammad Amjad**, Dongsheng Wen, 'Novel forward osmosis water desalination based on direct absorptive nanoparticles', 4th Water Research Conference, The Role of Water Technology Innovation in the Blue Economy, 10-13 September 2017, Waterloo, Ontario, Canada.

The candidate as a primary author of this work, formulated the novel draw solutions, performed all the experiments, analysed the data and presented this work as a poster in the conference. Dongsheng Wen supervised the work and helped in refining the discussion and finalizing the publication.

Table of Contents

List of Tables

List of Figures

Nomenclature

AAS	Atomic Absorption Spectrometry
AC-FS	Active Layer facing Feed Solution
AM	Air mass filter
CCA	Constant Contact Angle
CCD	Charge Coupled Device
CCR	Constant Contact Radius
CECP	Concentrative External Concentration Polarization
CNF	Carbon Nano Fibre
CNTs	Carbon Nanotubes
CP	Concentration Polarization
DANFs	Direct Absorption Nanofluids
DAQ	Data Acquisition
DASC	Direct Absorption Solar Collection/Collector
DI Water	Deionized Water
DICP	Dilutive Internal Concentration Polarization
DLS	Dynamic Light Scattering
DNA	Deoxyribonucleic acid
DS	Draw Solution
ECP	External Concentration Polarization

ED	Electro Dialysis
EDS	Energy dispersive X-ray Spectroscopy
EG	Ethylene Glycol
EMCCD	Electron Multiplying Charge Coupled Device
FM	freezing melting
FO	Forward Osmosis
FPSC	Flat Plate Solar Collector
FS	Feed Solution
FTIR	Fourier Transform Infrared
gMH	$gm^{-2}h^{-1}$
GNPs	Gold Nanoparticles
GOR	Gained Output Ratio
GONP	Graphene Oxide Nano Platelets
HDH	Humidification De-Humidification
HTFs	Heat Transfer Fluids
HTI	Hydration Technologies Inc.
ICP	Internal Concentration Polarization
JIS	Japanese Industrial Standards
K/CNF	Potassium functionalized Carbon Nano Fibre
LMH	$Lm^{-2}h^{-1}$
MD	Membrane Distillation

MED	Multi Effect Distillation
MnPIV	Multilayer Nanoparticle Image Velocimetry
MNPs	Magnetic Nanoparticles
MSF	Multi Stage Flashing
MWCNT	Multi Walled Carbon Nano Tubes
MWCNTs	Multi Walled Carbon Nanotubes
NDS	Novel Draw Solution
NIR	Near Infra-Red
NPs	Nanoparticles
PAA	Poly-Acrylic Acid
PEG	Poly Ethylene Glycol
PG	Propylene Glycol
ppm	Parts per Million
PRO	Pressure Retarded Osmosis
PTE	Photothermal efficiency
PTFE	Polytetrafluoroethylene
PV	Photovoltaic
PVD	Passive Vacuum Desalination
RO	Reverse Osmosis
RPM	Revolutions Per Minute
SAR	Specific Absorption Rate

SDS	Sodium Dodecyl Sulphate
SEM	Scanning Electron Microscopy
SPR	Surface Plasmon Resonance
SSF	Single Stage Flashing
TC	Thermocouple
TDS	Total Dissolved Solids
TEG	Tri Ethylene Glycol
TEG-K/CNF	Hybrid of TEG and K/CNF
TEM	Transmission Electron Microscopy
TGA	Thermo Gravimetric Analysis
TIR	Total Internal Reflection
TIRFM	Total Internal Reflection Fluorescence Microscopy
TPs	Tracer Particles
TREG	Tri-Ethylene Glycol
TSC	Tri Sodium Citrate
UV-Vis	Ultraviolet to visible
XRD	X-ray Diffraction
[HMIM][NTf2]	1-hexyl-3-methylimidazolium bis(trifluoromethylsulfonyl)imide
[HMIM]BF4	1-hexyl-3-methylimidazolium tetra fluoroborate

Symbols

η_{PTC}	Photothermal conversion efficiency
A_a	Area of the aperture
J_s	Reverse solute flux ($gm^{-2}h^{-1}$)
J_w	Water flux ($Lm^{-2}h^{-1}$)
L_v	Latent heat of vaporization
V_0	Initial droplet volume
V_n	Normalized volume
V_t	Instantaneous droplet volume
c_n	Specific Heat Capacity of nanofluid (J/kgK)
c_p	Specific Heat Capacity (J/kgK)
c_w	Specific Heat Capacity of water (J/kgK)
m_n	Mass of nanoparticles (kg)
m_v	Mass of the condensed vapours
$\Delta\bar{T}$	Average temperature difference
ΔP	Hydraulic pressure difference (atm)
$\Delta\pi$	Osmotic pressure difference (atm)
ΔT	Temperature difference
Δc	Concentration gradient (mg/L)
π	Osmotic pressure (atm)

A	Coefficient of membrane permeability ($Lm^{-2}h^{-1}atm$)
B	Constant for solute permeability of the membrane
H	Enthalpy (kJ/kg)
dt	Change in time
m	Mass (kg)
η	Efficiency

Chapter 1
Introduction

1.1 Current global water scenario

Water is an essential commodity for the survival and existence of all living beings on earth. In comparison to its importance, the proportion of potable water is very small and becoming scarce with every passing day. The earth is about 70% as water and about 98% of this water is salty and not drinkable. About 87% of the remaining 2% drinkable water is either frozen in icecaps and glaciers or mixed with soil as moister. The survival of all living beings is dependent on this left over quantity of drinkable water which is approximately 0.25% only (**Fig.1.1**) and is believed to be sufficient to meet this need [1]. But unfortunately, the distribution of this water is not even all over the planet and is not available when and where needed.

The resources of fresh drinking water are almost constant since the very first day of life on earth but the rapidly increasing world population is causing these resources to decline at much higher rates to fulfil water needs. In addition to this, the industrialization and economic growth are also polluting portable water resources [1, 2]. As a result, currently about 40% of the world population is facing drinking water shortage severely and this figure is expected to be increased to 60% by the year 2025.

1.2 Water desalination, solar energy and forward osmosis

In order to meet the growing demand of fresh water, a number of techniques are being used to convert salted seawater or brackish water in arid areas of the world into drinkable water. These techniques can broadly be categorized into two classes: one in which water is passed through a membrane under high pressure without phase change like reverse osmosis (RO) or osmotic pressure gradient is involved like forward osmosis (FO) and the other in which phase change is involved. The latter category includes; solar stills, single stage flashing (SSF), multi stage flashing (MSF), humidification/dehumidification (HDH), multi effect distillation (MED), membrane distillation (MD), passive vacuum desalination (PVD), freezing melting (FM) desalination, etc. [3].

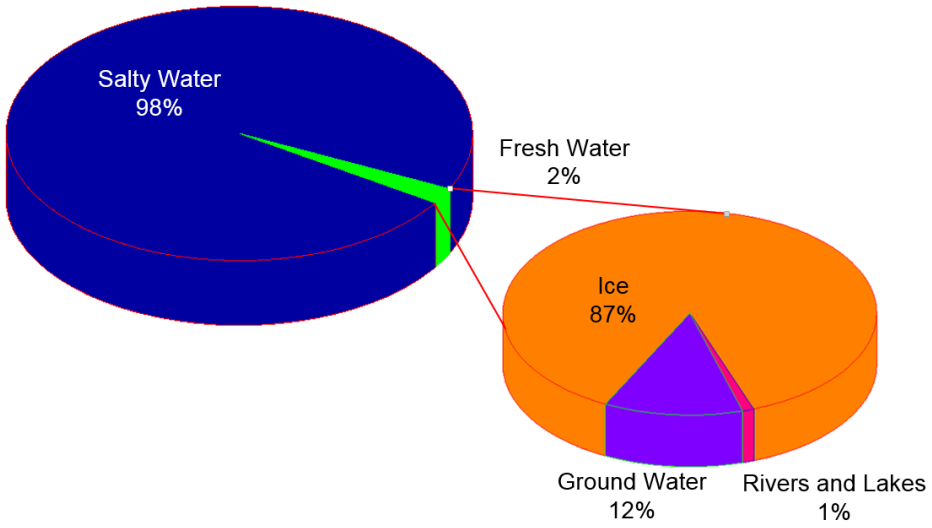

Figure 1. 1 World water distribution

Broadly speaking, two types of energy resources can be used to run the above mentioned water desalination processes namely; non-renewable and renewable. Oil rich countries like Gulf countries and others use non-renewable energy sources like oil and gas to desalinate sea water through reverse osmosis and multi effect

evaporation. About 300,000 barrels of crude oil equivalent per day is being consumed by 30 or so water desalination plants in Saudi Arabia and the same is the case with other Gulf countries including Algeria and Libya [4]. Though these countries have huge gas and oil reservoirs as low-priced energy sources, fossil energy consumption is causing a serious threat to the environment as a result of CO_2 emission. Also there are some areas which are far away from the energy grid lines or where energy is too much expensive or could not be supplied easily.

Owing to these factors, countries like Saudi Arabia and other oil rich countries have shown great interest in using renewable energies in water desalination processes. The drinking water needs can easily be met using local renewable energy source. Areas with high solar irradiation intensities are usually water scarce. This solar energy can be a major driving force for the sea or brackish water desalination process. Hence solar energy driven water desalination plants or units are a suitable option for meeting the potable water needs in remote and sunny areas.

Water desalination is an energy intensive process as compared to other conventional water treatment processes. But forward osmosis (FO) is a low grade energy operated process in which the driving force is the osmotic pressure gradient across a semipermeable membrane. Forward osmosis has grabbed the attention of researchers in past few years with the developments in FO membrane. Very less chance of membrane fouling as compared to RO, high rates of salt rejection by FO membranes and easy solution of concentrated brines produced by other desalination processes are the benefits of FO [5] other than its low grade energy operation [6]. But a suitable draw solution with high osmotic pressure gradient as compared to feed water and ease of its regeneration are the greatest challenges in commercialization of FO desalination technology.

Direct absorption solar collection concept is based on the absorption of solar energy directly by the working fluid instead of being absorbed by an absorbing surface and then transferred to the working fluid by convection as in conventional solar thermal collectors. The efficiency of direct absorption solar collectors can be significantly enhanced by dispersing different nanoparticles in the working fluid (Chapter 4 and Chapter 5). Nanofluids are engineered colloidal suspensions of nanoparticles in a base fluid and can be used as working fluid for direct collection of solar thermal energy and their application as draw solution in forward osmosis (Chapter 6).is a new development.

1.3 Why nanoparticles?

The material properties are significantly different at the nanoscale than that of bulk material. The size dependent material properties are ruled by the so called quantum effect at the nanoscale where size of the particle ranges from 1-100 nm. The surface area of the nanoparticles is phenomenally higher than the same mass of bulk material and this can be explained with the help of a simple example as shown in **Fig. 1.2** [7]. The surface area of a cube of solid material having 1 cm side length (volume as 1 cm^3) is 6 cm^2. 10^{21} cubes with 1 nm side length (each with surface area as 6 nm^2) will be required to fill the same 1 cm^3 volume thus generating the total surface area equal to 6 m^2 and 6000 m^2 respectively. It can be simply said that only 1 cm^3 volume of cubic nanoparticles gives a total surface area which is one-third times the area of a football ground.

With exponentially increased surface area per mass of a material at nanoscale, a large amount of material comes in contact with the surroundings which greatly

improves its reactivity. One of the most interesting use of quantum effect at the nano level is to tune the material properties of interest.

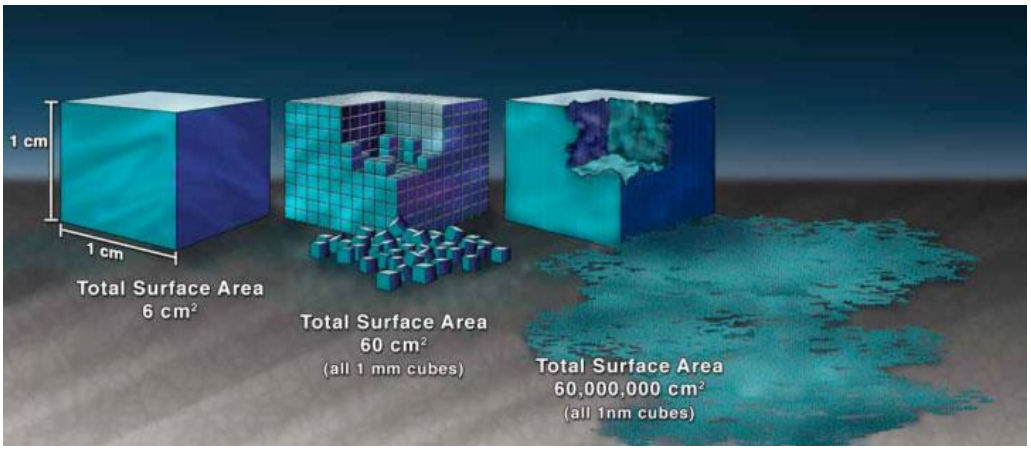

Figure 1. 2 An illustration of the increased surface area in nanomaterials.

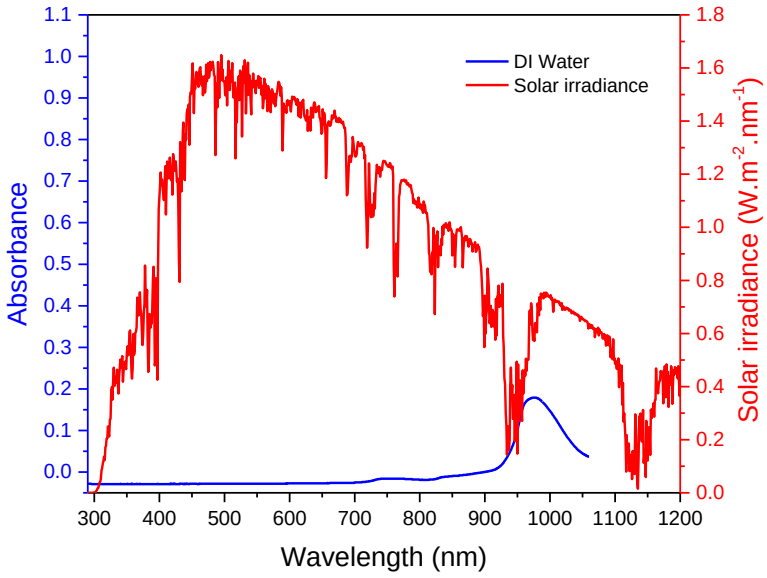

Figure 1. 3 Spectra of absorbance of deionized water and solar irradiance in visible to infrared wavelength.

Fig. 1.3 gives solar irradiance spectrum in visible to near infrared regions where most of the solar energy is contained [8] and the absorbance of the most of conventional heat transfer fluids (HTFs) like water is very poor in this range [9, 10].

Nanoparticles of different materials can be suspended in water in order to tune the property of high solar absorptivity to capture solar energy efficiently. Also the volumetric solar energy absorption minimizes the radiative heat loss by trapping the solar radiations.

On the other hand, during FO process, the salts being used as conventional draw solutions get dissociated in water and their ions are likely to pass through the FO membrane due to their significantly smaller size as compared to membrane pore size. The draw solution becomes less affective with increasingly salt ions leakage thereby reducing the osmotic pressure and finally the water flux across the FO membrane. Nanoparticles based novel draw solutions can overwhelm this leakage issue and can sustain the osmotic pressure and water flux for longer durations with the added advantage of minimum reverse solute flux due to their bigger size as compared to size of salt ions. In addition to enhanced osmotic pressure and reduced solute reversal, the nanofluid based novel draw solutions can efficiently absorb solar energy directly for their regeneration and easy product water recover.

1.4 Research objectives

This work aims to develop nanofluid based novel draw solutions for FO desalination applications. Properly engineered, these draw solutions could provide efficient solar energy absorption, sufficient osmosis pressure, and enhanced water flux yet with easy regeneration characteristics. The hypothesis of the research work can be stated as;

“Do the nanofluid based novel draw solutions enhance direct solar absorption for volumetric solar heating and steam generation significantly and develop sufficiently high osmotic pressure with minimum reverse flux to produce potable water?”

The hypothesis statement can be broken down into the following distinct research objectives;

- To synthesize and characterize various nanofluids for efficient direct solar energy absorption and steam generation, and to develop nanoparticle-polymer hybrids having high osmotic pressure together with high solar absorption as novel draw solutions for FO desalination.
- To investigate the performance of the characterized nanofluids based on direct solar absorption on bulk fluid volume as well as at micro droplet level.
- To analyse the capability of characterized nanofluids for direct steam generation under a concentrated solar flux and to analyse the entrainment of nanoparticles under vigorous boiling.
- To evaluate the osmotic pressure, water flux and reverse solute flux of the characterized nanofluids as new draw solutions by developing a laboratory scale forward osmosis desalination test rig and use a semi permeable forward osmosis membrane.
- To investigate the regeneration and cyclic performance of polymer-nanofluid based novel draw solutions under a simulated solar radiation flux and to check the quality of product water.

1.5 Organization of the dissertation

This research work is focused on the formulation and use of nanofluids as novel draw solutions for forward osmosis desalination with their regeneration using solar energy and act as a ‘proof of concept’. To realize this proof of concept work, the work can be divided into seven chapters.

Chapter 1 gives an overview of the research work describing the need of efficient water desalination techniques, solar energy utilization and the role of nanoparticles in the current water stressed scenario. **Chapter 2** includes a brief snapshot of the direct solar absorption studies using numerous nanoparticles in different base fluids and under varying experimental conditions as well as an overview of the different desalination techniques with a particular focus on FO desalination as appeared in the literature and is concluded with the novel idea of combining temperature and pressure aspects together in the form of direct solar absorptive nanofluid new draw solutions for FO solar desalination.

Chapter 3 is based on formulation of various nanofluids and their characterization using numerous techniques. **Chapter 4** detailed the performance investigation of different nanofluids in terms of their ability to absorb the solar flux directly at bulk volume as well as on micro droplet level and investigate the fluid flow pattern near the three phase contact line and the resulting deposition patterns. **Chapter 5** encompasses the nanofluid based solar steam generation under concentrated solar flux and evaluates the nanoparticle entrainment phenomenon under vigorous boiling.

The FO performance of the novel draw solutions is given in **Chapter 6**. Osmotic pressure, water permeation flux and draw solution leakage rate are investigated using a laboratory scale FO test cell along with solar energy based regeneration of the draw solution. **Chapter 7** summarises the conclusions of the whole research work and presents future recommendations for further exploration in this field in different aspects.

Chapter 2
Direct Solar Absorption, Desalination and Forward Osmosis

This chapter deals with literature background addressing the direct solar collection, different desalination techniques with special focus on forward osmosis desalination and finally the proposed novel concept of nanofluid based direct solar absorptive draw solutions.

2.1 Introduction

Nanofluids have a great potential for absorbing solar energy directly when they are dispersed in an aqueous medium. The increased surface area to volume ratio of nanoparticles enables them to exhibit extra ordinary characteristics. Various heat transfer related applications have increasingly used nanoparticles due to their ability to absorb and carry heat with them. Literature review can be divided into two main categories; one dealing with nanofluid based direct absorption solar collection including the solar absorption in a micro droplet of nanofluid, and the other with water desalination techniques in general and forward osmosis desalination in particular.

2.2 Direct absorption solar collection

With increasing concerns over global warming and environmental issues, developing renewable energy is becoming more and more important to secure our energy needs. Solar energy is the most abundant source of energy and is easily accessible. However making efficient use of solar energy is not an easy task [11]. A conventional plate-type of solar collector absorbs solar energy on an absorbing plate, and transfers the heat via a wall to a working fluid running inside [12-14]. It is a surface-based absorption, which limits the effective utilization of solar energy by creating a large temperature difference between the absorbing plate and the working fluid, especially for concentrated solar energy applications [15].

The limitations of surface absorption can be mitigated by a volume based solar absorption in which the working fluid directly absorbs energy from the sun, named as direct absorption solar collection (DASC). The concept has its origin back in 1970

[16] and is receiving an increasing interest and attention recently by using different nanoparticles [17-19].

Direct absorption solar collection concept is based on the absorption of solar energy directly by the working fluid instead of being absorbed by an absorbing plate and then transferred to the working fluid by convection as in conventional solar thermal collectors as shown in **Fig. 2.1** and **Fig 2.2** [20]. The efficiency of direct absorption solar collectors can be significantly enhanced using nanoparticles of different metallic materials mixed in the working fluid. Nanofluids are engineered colloidal suspensions of nanoparticles in a base fluid and can be used as working fluid for direct collection of solar thermal energy. Numerous studies have been conducted to analyse the performance of direct absorption solar collectors and the effect of introducing a small concentration of different nanomaterials. A comprehensive summary of some of these investigations is presented in Table 2.1.

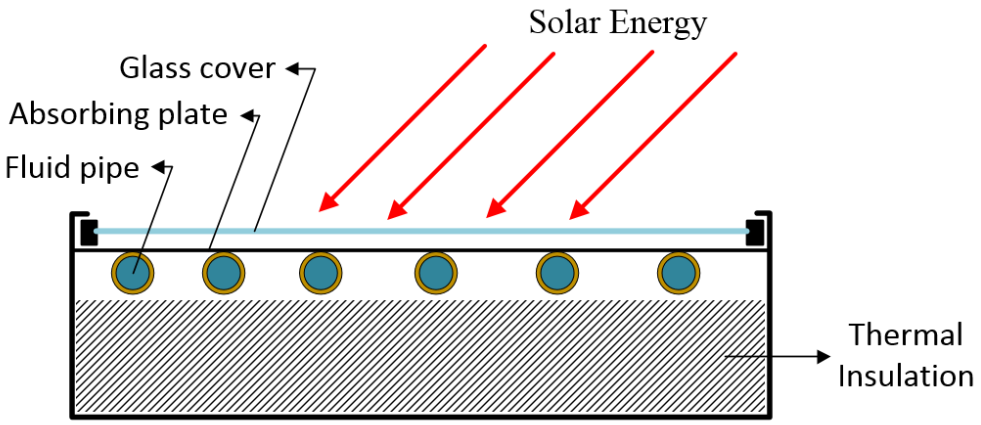

Figure 2. 1 Schematic of a conventional solar collector

Table 2. 1 Nanofluid based direct absorption solar collection

Ref.	**Nanomaterial/ base fluid**	**Observations and remarks**
Zhang *et al.* [21]	Au/DI water	Maximum enhancement is 65% at 6 ppm particle concentration.
Bandarra *et al.* [22]	Silver/DI water	The SAR was decreased from 6.5 kW/g to 0.01 kW/g at a particle concentration of 650 ppm which was believed due to the increase in interaction between particles.
Yousefi *et al.* [23]	Al_2O_3/DI water	The efficiency for 0.2 wt% was greater than that of 0.4 wt% in comparison with water as radiation absorbent.
Said *et al.* [12]	TiO_2/DI water	The flat solar collector efficiency was greater at lower particle concentration at a flow rate of 0.5kg/min.
Verma *et al.* [24]	Al_2O_3/DI water	Efficiency is increased by 3-4% for 0.05 wt % nanofluid as compared to water as working fluid.
Said *et al.* [25]	Al_2O_3/DI water and EG	Low concentrations of nanoparticles have nearly negligible effect on pumping power and pressure drop.
Otanicar *et al.* [26]	graphite /DI water	An improvement in DASC efficiency of 3% for 30nm graphite nanoparticles, 5% for 20nm silver nanoparticles and only 1% for CNT was observed.
Liu *et al.* [15]	Graphene/[HMIM]BF4	70% efficiency achieved at a solar concentration of 20, 5 cm receiver height and 0.0005 wt% of graphene.
Zhang *et al.* [27]	Ni, Cu and carbon coated Ni/ionic liquid	The absorbed energy for Ni/C reached to 100% at 40 ppm, making it a good choice of DASC.

Zhang *et al.* [21] prepared gold nanoparticles by citrate reduction method and cleaned and purified through membrane dialysis. After cleaning, the gold NPs were

analysed on UV-Vis for impurities. Transmission Electron Microscopy (TEM) and Dynamic Light Scattering (DLS) were used to identify the size and shape of engineered GNPs which turned out to be around 15nm to 20nm in size and spherical in shape.

The dispersion of gold nanoparticles was investigated for photothermal conversion features under a sun simulator. It was found that with the increase in particle concentration, the photothermal conversion efficiency increased but in non-linear fashion and the maximum efficiency enhancement was found at 6 ppm particles concentration within the range of experimentation. On comparing with the nanoparticles of other materials, it was found that Au NPs have the highest SAR which is believed to be due to the effect of surface plasmonic resonance in visible spectrum.

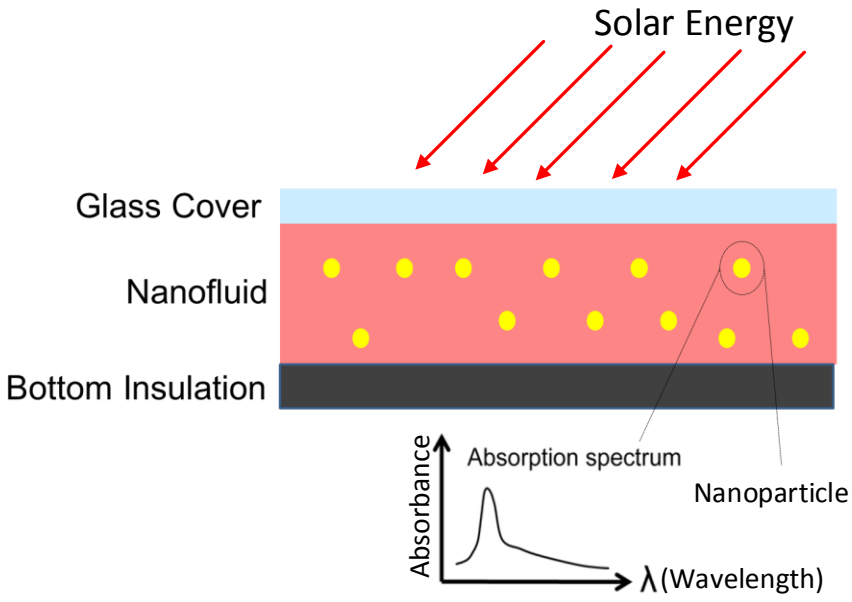

Figure 2. 2 Schematic of a direct absorption solar collector in which the solar thermal energy is absorbed directly by the working fluid containing nanoparticles

Bandarra *et al.* [22] investigated the photothermal conversion performance characteristics of deionized water based silver nanofluid in direct sunlight conditions. DI water based silver nanofluid was prepared by a homogenizer working under high pressure. The experimentation was done for five particle concentration from 0.0001625 vol% to 0.065 vol% and it was concluded that even with very low particle concentrations, the bulk temperature was increased substantially. Furthermore, it was concluded that at peak temperature, the thermal stored energy increased with particle concentration. At the beginning of the radiation process, the photothermal conversion was at its best and the specific absorption rate (SAR) was nearly constant for particle concentrations up to 6.5 ppm. The SAR was decreased from 6.5 kW/g to 0.01 kW/g at a particle concentration of 650ppm which was believed due to the increase in interaction between particles.

Sokhansefat *et al.* [13] studied numerically the dependence of heat transfer rate on the volume concentration of Al_2O_3 synthetic oil based nanofluid in a trough collector tube. This study showed that there is a direct relation heat transfer coefficient and nanoparticles volumetric concentration. It was also concluded in this study that with the increase in the absorber operational temperature, the enhancement of heat transfer in the fluid due to nanoparticles is decreased.

Said *et al.* [28] used commercially available spherical shaped TiO_2 with approximately 21 nm as an average diameter with PEG 400 as surfactant and distilled water as base fluid. 0.1 vol% and 0.3 vol% nanofluid of TiO_2 were prepared with distilled water as base fluid using a highly pressurized homogenizer.

Verma *et al.* [24] studied the effect of Al_2O_3-water based nanofluid on DASC under varying mass flow rates (60, 80, and 100ml/hr) and used two volume fractions 0.005% and 0.05%. Efficiency is increased by 3-4% for 0.05 wt % nanofluid as

compared to water as working fluid. Efficiency also increases with the increase in mass flow rate but the temperature difference decreases with increase in mass flow rate.

Controlled morphological features of nanoparticles and their complete dispersion in base fluid can significantly enhance thermophysical properties like specific heat capacity, thermal conductivity and photothermal conversion performance of working fluids of direct absorption solar collectors. To maximize solar absorption in DANFs, different nanofluids are still to be explored.

Nanomaterials with different optical absorption peaks can be combined to cover maximum spectrum of visible light. Similarly nanoparticles of same material but having different shape and size can be combined for this purpose and a further investigation is required to analyse the combined effect of size and shape on direct absorption behaviour. Furthermore, concentration of nanoparticles in base fluid plays an important role in their photothermal conversion performance. In most of the studies, photothermal conversion efficiency is proportional to the concentration of nanoparticles but not always. The feasibility of DANFs in water forward osmosis based desalination using solar energy has not yet been touched by any research group and is the main novelty and scope of this work.

2.2.1 Droplet evaporation

The cycle of water in nature is due to the phenomenon of evaporation of liquid droplets and the water vapour condensation. A liquid droplet evaporates as long as its unsaturated vapours surround it. In the presence of some insoluble particles in the liquid droplet, the droplet evaporation results in a deposition pattern like a coffee ring, uniform pattern, concentric rings, central congregated bump or some combined

structures. The particle motion within the droplet and the resulting deposition pattern are dependent on evaporation mode and the triple-phase (solid, liquid and vapour) line dynamics. The particle organization, flow dynamics and heat transfer mode during the evaporation of a sessile droplet under a solar or simulated radiation flux are the key factors in understanding the role of presence of nanoparticles in a micro droplet as well as macro evaporation of liquids. The visualization of tracer particles in the presence of plasmonic radiation absorptive nanoparticles can be possible through the principle of total internal reflection and total internal reflection fluorescence microscopy.

Liquid droplet evaporation has a wide range of applications such as inkjet printing, thin film coating, spray drying, fuel injection and optoelectronic device manufacturing [29-32], as well as the diagnosis of diseases from drying the blood droplet and DNA microchips [33-35]. The deposition pattern of a droplet depends on the fluid flow within the droplet [36-41], temperature gradient [37, 42, 43], concentration and type of the nanoparticles [44-46]. The nature of the substrate [47-50] and type of base fluid [51, 52] also have important roles on the formation of droplet deposition patterns. The fluid flow within a nanofluid based droplet during evaporation can either be a capillary flow or Marangoni flow. When the peripheral walls of the droplet are pinned on the substrate surface at solid-liquid-vapour interface, also called three phase line or triple line, liquid flows radially outward to refill the liquid loss due to evaporation, which is known as capillary flow [40]. Marangoni flow, on the contrary, works with a reverse direction and due to non-uniformly distributed surface tension alongside the liquid-vapour line. This uneven distribution of surface tension may either be due to the temperature gradient [42, 43] or concentration gradient [40, 53].

The effect of various types of nanoparticles on the evaporation of a droplet has been investigated in many studies [44-46]. Gan et al. [44] studied the evaporation rate of ethanol based Al_2O_3 and Al nanofluid at various radiation levels, and showed that the evaporation rate of Al nanofluid was better than that of Al_2O_3 due to a higher absorption of Al nanoparticles. The effect of adding laponite, Fe_2O_3 and Ag nanoparticles to deionized water was investigated by Chen et al. [45] in terms of nanofluid droplet evaporation rate. The evaporation rate constants for nanofluids were found to be different from the classical d^2-law. While Ag enhanced the evaporation rate, laponite and Fe_2O_3 particles were found to suppress it, which was ascribed to the apparent heat of vaporization.

Sefiane and Bennacer [46] found a reduction in the evaporation rate of ethanol based aluminium nanofluid droplet on a heated PTFE (Polytetrafluoroethylene) surface as compared to the base fluid. In addition, they observed that the droplet evaporation followed the d^2-law under higher convective temperature but not at lower or natural convection conditions [54]. Wei et al. [55] investigated numerically the dependence of evaporation rate on the Peclet number, particle concentration and contact angle of the droplet containing nanoparticles. Gan and Qiao [56] observed experimentally that adding MWCNT to ethanol enhanced the evaporation rate and droplet temperature due to improved optical absorption.

2.2.1.1 Total internal reflection

When a light beam travelling through a medium having a refractive index n_1 enters another medium having a lower refractive index n_2 at an angle (θ_1) larger than the critical angle (θ_c), the beam cannot pass through the first medium and is totally reflected. This phenomenon is known as total internal reflection (TIR). The critical angle is the incident angle of the light wave at which its angle of refraction (θ_2) is

90° as shown in **Fig. 2.3** and TIR takes place when $\theta_1 > \theta_c$. The critical angle (θ_c) can be calculated from Snell's law [57];

$$n_1 \sin\theta_c = n_2 \sin 90^o \tag{2.1}$$

Therefore,

$$\theta_c = \sin^{-1}\frac{n_2}{n_1} \tag{2.2}$$

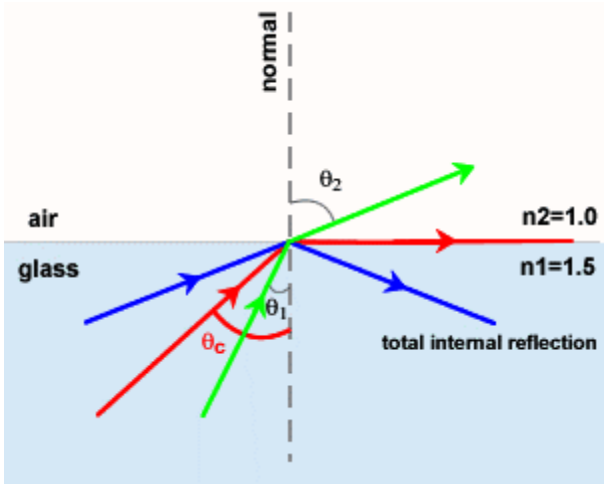

Figure 2. 3 The phenomenon of total internal reflection

2.2.1.2 Total internal reflection fluorescence microscopy

The visualization of the flow of accumulating tracer particles in the vicinity of the three phase line of a micro droplet can be obtained by fluorescent microscopic technique. The tracer particles inside the droplet move passively under the influence of capillary flow and Marangoni flow [58]. The tracer particle motion pattern is also dependent on surface tension, van der Walls and drag forces [59]. The liquid evaporation is very intensive in the thin film region and its direct observation using traditional techniques is intrinsically difficult due to optical limitation. The total internal reflection fluorescence microscopy (TIRFM) is a recently developed technique for the measurement of film thickness and contact angle near the contact line of a partially wetted droplet with a high spatial resolution [60]. The TIRFM uses

evanescent wave illumination developed by the total internal reflection (TIRF) and can be applied for micro flow visualization via nanoparticle image velocimetry (nPIV) and multilayer nanoparticle image velocimetry (MnPIV) [61, 62] in the thin film region (**Fig.2.4**).

An evanescent wave is a wave which is produced as a result of TIR and its intensity decays exponentially along the distance perpendicular to the interface.

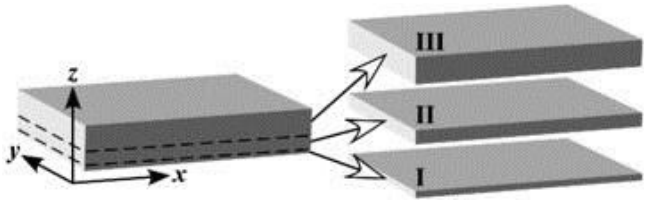

Figure 2. 4 A schematic of the multilayer nanoparticle image velocimetry

The intensity of an evanescent wave can be expressed as below in Eq. 2.3, [62];

$$I(z) = I_m e^{\left(-\frac{z}{z_p}\right)} \tag{2.3}$$

Where I and I_m are the evanescent wave intensity and the maximum intensity at the wall (i.e. $z = 0$) respectively and z and z_p are the distance normal to the wall and the penetration depth respectively. The penetration depth (z_p) can be expressed as in Eq. (2.4);

$$z_p = \frac{\lambda_o}{4\pi n_1} \left[sin^2\theta - (\frac{n_2}{n_1})^2\right]^{-\frac{1}{2}} \tag{2.4}$$

Where λ_o is the wavelength of the incident light, θ is the incident angle.

2.3 Water desalination and forward osmosis

Solar water desalination is a combination of two independent systems namely; solar collection system and water desalination system. Solar thermal energy collection

includes conventional solar collectors and direct absorption solar collectors which have been briefly discussed in the previous section. Water desalination processes include; solar stills, single stage flash (SSF) and multi stage flash (MSF) distillation, humidification dehumidification (HDH), multi effect distillation (MED), reverse osmosis (RO), passive vacuum desalination, membrane distillation, etc. A brief overview of the solar based water desalination techniques is presented in the table 2.2.

Although RO (reverse osmosis) system has the largest installed capacity for water desalination followed by MSF (multi stage flash distillation) [3], yet there are a number of challenges and limitations of these desalination techniques. RO requires extensive and very careful pre-treatment of seawater and high tech membrane for water filtration. The installation and replacement of these membranes are complex in nature and need expertise. Organic, inorganic and bio fouling of RO membrane is the most challenging issue of RO desalination process [63-65]. Also the chemicals and bacteria less in size than water molecules get through the RO membrane thereby causing health problem to the user [66].

RO membrane also demineralize essential minerals from water and is known as “dead water” in Japanese terms [66]. As far as MSF is concerned, it is not a thermal efficient process [67]. Flashing chambers connected in series in MSF require a precise control over pressure in the chamber and its temperature to start a normal operation. The intermittent nature of solar energy and the fixed nature of orifice of flashing chamber is not suited to incorporate required pressure changes in the inter stage flashing chambers [68].

Table 2. 2 Solar water desalination techniques

Desalination techniques	**Features**	**Challenges**
Solar stills	Simplest variety of designs [69-73]	Slow process and very low production rate
Solar based multi effect distillation (MED)	The operating temperature is normally lower than 75 ^{o}C [74]	In comparison with MSF, MED has high efficiency, less water recycling in the loop and better heat transfer coefficient [75, 76]
Solar Powered Reverse Osmosis (RO)	Solar PV powered RO system is more common and popular than solar thermal powered [77, 78].	RO requires extensive and very careful pre-treatment of seawater. Organic, inorganic and bio fouling of RO membrane is the most challenging issue of RO desalination process [63-65].
Solar powered single and multi-stage flash (SSF, MSF) distillation	Can be integrated with solar pond [68, 79] or solar collector [80-82]	MSF is not a thermal efficient process and the thermal loss is too high due its high operating temperatures [67, 83]
Solar humidification dehumidification (HDH) [84-86]	It uses the ability of air to carry water vapours	HDH is still in developing stage and there is a lot of room for improvement to increase portable water production rate and make it energy efficient.
Membrane Distillation (MD)	Water vapours from feed side can pass through a membrane and are condensed on the other side of the membrane.	Energy consumption and cost of MD process is more than MSF and MED due to a resistance offered to mass flow and lowered thermal effectiveness due to heat loss by the membrane [87, 88]

A large amount of seawater circulating in the condenser tubes for its preheating on the cost of condensation heat of vapours in the flashing chamber requires a big amount of energy or indirectly electricity. Similarly MSF powered by solar ponds may contaminate the soil due the leakage of brine [89] and a great care is needed to maintain the salinity level, pH and clarity of the solar ponds. The market is still in need of a water desalination technology that is easy to install and maintain, energy efficient, cost effect and suitable for areas away from the electricity grids.

2.3.1 Forward osmosis desalination process

Forward osmosis (FO) is a process in which the driving force is the difference of solute concentrations across a semipermeable membrane. Water from the feed side of the membrane where solute concentration is low flows through the membrane towards higher concentration side known as draw solution side, under osmotic pressure difference gradient. A general mathematical relation for water flux (J_w) in osmotically driven processes, given by Cath *et al.* [5] is follows:

$$J_w = A(\Delta\pi - \Delta P) \tag{2.5}$$

where A is constant of water permeability of the membrane (L.m^{-2}.h^{-1}.atm), $\Delta\pi$ is the osmotic pressure difference (atm.) between draw solution side and feed side and ΔP is the hydraulic pressure difference (atm.) applied across the membrane. In the above relation, $(\Delta\pi - \Delta P)$ is the net driving force under which water permeates through the membrane. As no or very low external hydraulic pressure is applied in case of FO, ΔP is zero and the relation for water flux is reduced to;

$$J_w = A\Delta\pi = A(\pi_{Draw} - \pi_{Feed}) \tag{2.6}$$

where π_{Draw} is the osmotic pressure of the draw solution and $\boldsymbol{\pi_{Feed}}$ is the osmotic pressure of the feed solution.

Water flux dilutes the draw agent and water from this diluted draw agent is separated in the recovery system. A schematic of the process is shown in **Fig. 2.5**, adapted from [90]. FO is a low grade energy operated process which has been used for desalination of brackish or seawater, food industry for concentrating the juices etc., reclaiming wastewater, generating electricity and for a controlled drug release purpose in biomedical [91]

If other water desalination technologies like RO, MED, MSF, etc. are compared with FO; FO has not been very popular in early years. The major reason why FO could not be developed as much as other desalination techniques is the lack of suitable FO membranes and draw solutions and the complexity of draw solution regeneration [5].

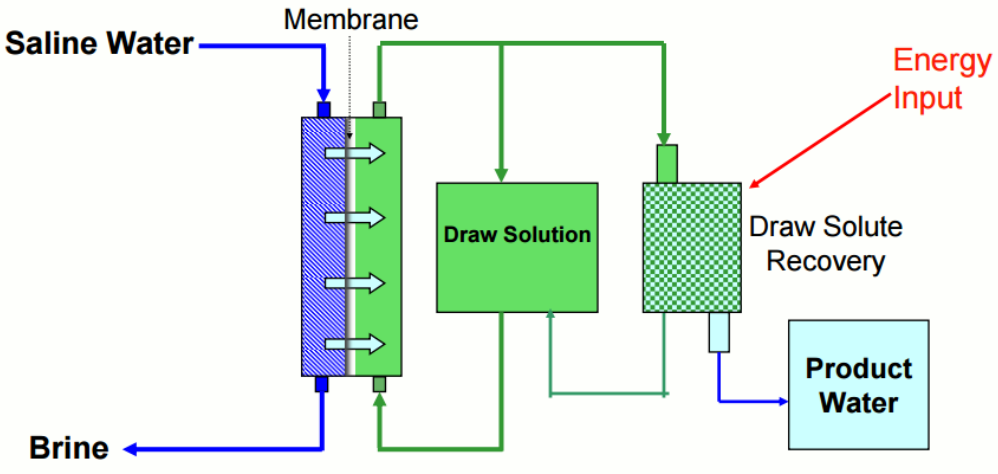

Figure 2. 5 Schematic of FO desalination process

FO has captured the attention of researchers with the development in membrane technology and a number of investigations have been conducted in the last three to four years as can be seen from **Fig. 2.6**. This is because FO has certain advantages over the other energy hungry desalination processes like RO, MED and MSF. The following section gives a brief description of these benefits. These benefits include low energy operation due to zero or less hydraulic pressure[92], negligible or less chance of membrane fouling as compared to RO [93, 94], an easy solution to brine issue generated from other water desalting processes and high rates of rejecting salts.

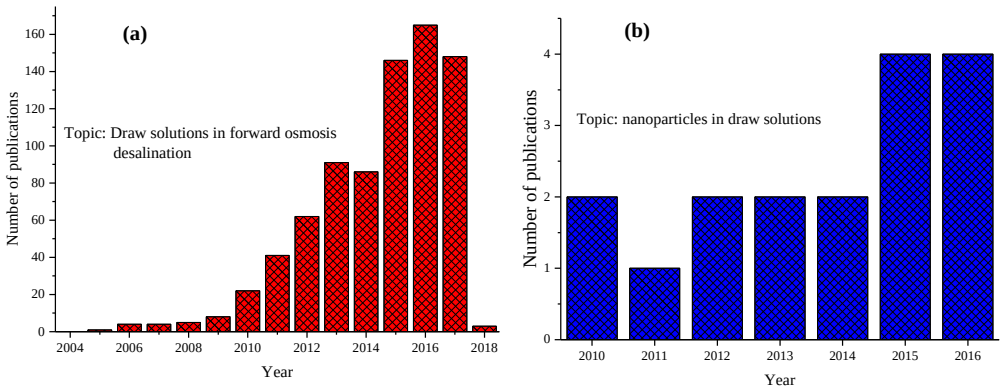

Figure 2. 6 Number of publications (including journal articles, conference proceedings papers and book chapters), (a) publications related to the topic "draw solution in forward osmosis desalination" and (b) publications related to the topic "nanoparticles in draw solutions" (the data is based on Web of Science statistics as on November 26, 2017)

2.3.2 Benefits of FO

2.3.2.1 Low energy consumption

As water permeates through the semipermeable membrane from the feed solution due to the concentration difference, no or very low hydraulic pressure is required for this operation [5, 95]. The energy consumption in FO desalination process is very low as compared to other widespread water desalting technologies like MSF, MED and RO for the permeation of water across the membrane. However a lot of energy is required for regeneration of draw solution and separation of potable water in FO.

If the energy required in different rampant water desalination technologies is converted to equivalent work which is defined as the amount of electricity generated by the same amount of energy e.g. steam when expanded in a turbine, FO is the least energy consuming desalting water process as can be seen in **Fig. 2.7**, as evaluated by McGinnis [96] against FO with ammonia-carbon dioxide gas mixture solution as draw agent.

The following relation (2.7) can be used for calculating the work equivalent (kWh/m^3) for different desalination technologies [97];

$$W_{eq} = \frac{(H_{steam\ used} - H_{steam\ at\ condensor}) \times \eta_{\ turbine} \times 1000}{GOR}\left(\frac{kJ}{m^3}\right) \times 0.000277\left(\frac{kWh}{kJ}\right) + W_{elect}\left(\frac{kWh}{m^3}\right) \quad (2.7)$$

where H, η, W_{elect} and GOR denote the enthalpy, turbine efficiency, equivalent work related to electrical energy and gained output ratio respectively.

Another investigation by Ali Shoeb [98] gives another comparison of energy consumed by various desalination technologies as shown in Table 2.3 on the basis of electrical equivalent work.

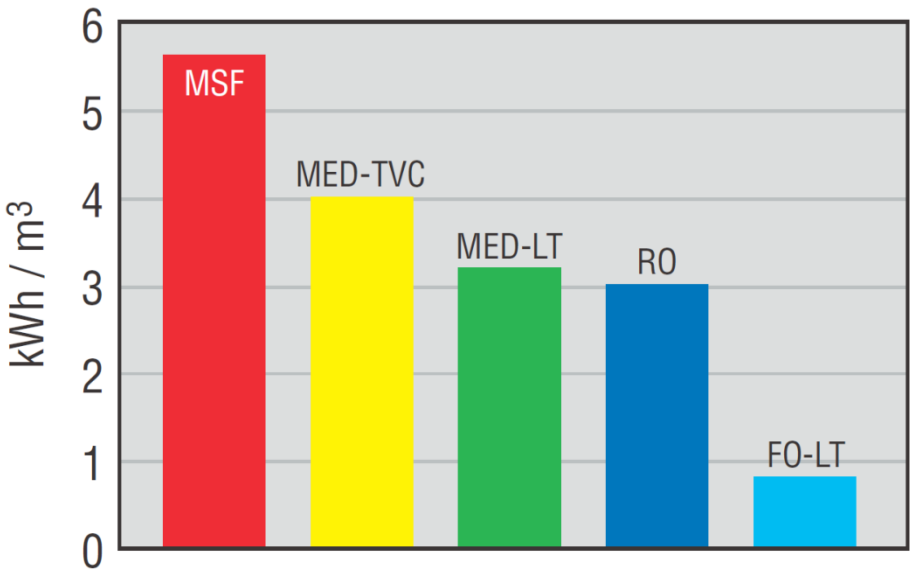

Figure 2. 7 Energy consumption comparison of different water desalination technologies (on x-axis) on the basis of 'Equivalent Work' (on y-axis) with NH_3-CO_2 and 1M ammonium salt as draw solution.

FO desalination is a two stage process in which water permeates across the membrane under the effect of osmotic pressure difference from the feed and dilutes the draw solution in the first stage. Almost no energy is consumed in this stage as compared to RO. In the second stage, the draw solution is to be regenerated and potable water is to be separated from the draw solution. Most of the energy required in FO operation is consumed in this stage.

Although the upper limit of electrical equivalent work in Table 2.3 for FO is higher than that of RO but it can be justified by stating that RO needs electricity only and

FO can utilize solar energy for its operation even in those areas where no electricity is available.

Table 2. 3 Energy consumption comparison of different desalination technologies

Desalination Technique	Electrical Equivalent Energy Requirement (kWh/m^3)
Forward osmosis	3-8
Reverse Osmosis	4-6
Multi Effect Distillation (MED)	15-58
Multi Stage Flash Distillation (MSF)	21-58

Such draw solutions need to be devolved which use low or minimum amount of energy for their regeneration and product water separation. Solar thermal energy is the best renewable energy source for the second stage draw solution regeneration in areas which are away from the grid lines. Also unnecessary energy recovery as is required in RO to make it energy efficient, makes FO more energy efficient than RO and an applicable solution to drinking water needs in areas where electricity is limited.

2.3.2.2 Minimum membrane fouling propensity

Membrane fouling is one of the major problems of membrane based processes like RO, FO and PRO in which different types of salts, organic, inorganic contamination and microorganisms are deposited on the active layer of membrane thereby reducing the water permeation. Membrane fouling not only reduces water flux across the

membrane but it also affects the lifetime of the membrane thereby increasing the maintenance and operating cost of the process. As water is transported under the effect of very high hydraulic pressure, membrane fouling in RO is of irreversible nature and needs to be properly addressed or the membrane to be replaced frequently. The driving force for water transport in FO is the osmotic pressure difference across the membrane and very low or zero hydraulic pressure is required, the membrane fouling propensity is very low as compared to RO and is reversible which can be mitigated easily.

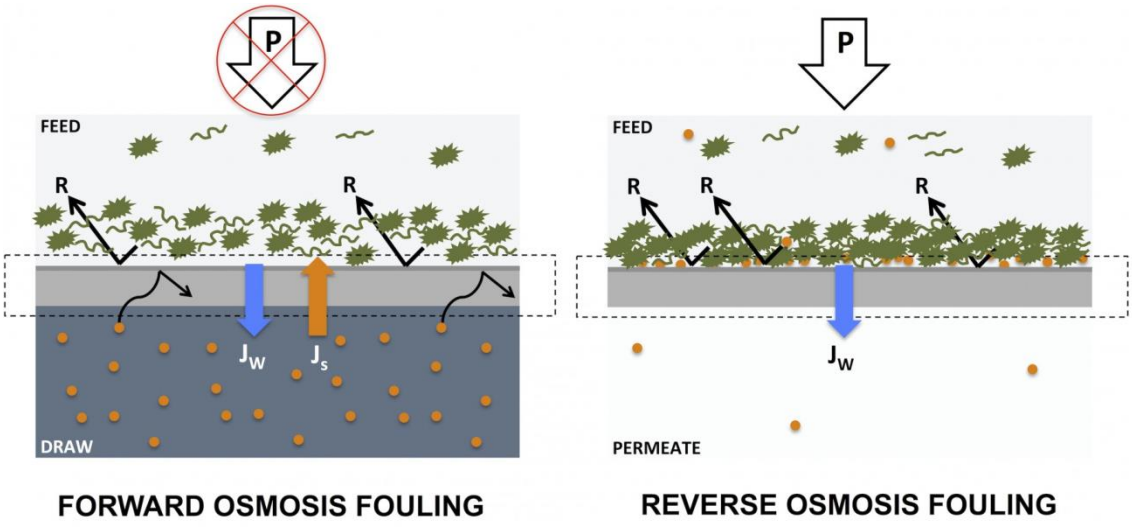

Figure 2. 8 Membrane fouling propensity in case of RO and FO

As cake layer of foulants is loosely packed due to no external hydraulic pressure in case of FO process, reduced water flux can be easily recovered by intermittent cleaning through cross flow or by creating turbulence near the membrane [99-101] as shown in **Fig. 2.8**. The reversible nature of membrane fouling in FO desalination process is also confirmed by Zhang *et al.* [102] and Chun *et al.*[101] in which they

used the actual non-chlorinated brackish lake water for studying the membrane fouling tendency.

Membrane fouling mitigation due to its loose binding and reversible nature is relatively very easy and economical as compared to RO. In addition to intermittent rinsing, hydrodynamic forces can be induced in the flow to mitigate reversible membrane fouling in FO. These hydrodynamic forces include; increasing the cross velocities of feed and draw solutions [103, 104], developing pulsated flow near the membrane surface, creating turbulence using spacer rings [104] and introduction of air bubbles [99] for the removal of membrane foulants. Use of these hydrodynamic forces will add to energy consumption of the process.

Loosely packed foulant layer and its reversible nature is one of the main attractions of FO desalination process and it diverts the attention of researchers to investigate it further. Also very low membrane fouling propensity makes FO a competitor of other desalination technologies. Further study is still required to understand the fouling mechanism and its mitigation in FO membranes.

2.3.2.3 Other miscellaneous benefits

FO offers high rates of salt rejection due to its membrane pore size [105], less foulant accumulation and no external pressure . The removal of TDS (total dissolved solids) from complex solution is done very effectively and efficiently by FO desalination process [106]. High salt rejection rate in FO enables it for treating highly salted streams (greater than 83 bar) which is not possible through RO [107]

Due to the absence of very high hydraulic pressure, no high strength materials are required to withstand this pressure [108]. No pre-treatment of feed or complex feed

solution is required in FO which is an essential and extensive activity in RO and some other desalination technologies. It also makes FO a cost effective desalination process.

FO is a clean and easy solution to municipal wastewater effluent [109] and other complex industrial streams like textile industries , oil and gas [110] and even nuclear wastewater streams [95].

Severity and intensity of brine generated through FO is very low as compared to other water desalting techniques. FO can effectively reduce the volume of rejected brine generated by other desalination processes like RO, MSF and MED which makes its disposal easy and cost effective.

2.3.3 FO challenges

With development in membrane technology, FO is aiming to compete with other prevalent desalination technologies. But there are certain technical limitations of the process and need to be further investigated and resolved. Despite of the attractive benefits mentioned above, there are various challenges to FO process which hinder its commercialization. Draw solute flux reversal, DS recovery and lack of proper and suitable draw solutions are some of the main challenges which FO desalination is facing. If these limitations are resolved and proper draw solutions are developed which adhere to most of the necessitated characteristics, FO could be one of the best technologies that can contribute to deal with drinking water issues particularly in remote areas. FO limitations are discussed in the following sections.

2.3.3.1 Reverse flux of draw solute

In addition to water permeation from the feed side to the draw solution side through the membrane under the effect of osmotic pressure difference, the draw solute may also permeate through the membrane towards the feed side under the effect of concentration gradient. This phenomenon is known as reverse solute diffusion or solute flux reversal which is again one of the major challenges faced by FO commercialization. As a result of reverse solute diffusion, the cost of the FO process is increased if an expensive draw solute is used because of its loss with time. The cost may also be increased due to further treatment of the concentrate before its disposal due to draw solute contamination if it is harmful for the environment as stated by Phillip [111].

The solute reversal also supports and worsens membrane fouling thereby decreasing the water flux through it. A general relation for estimating the reverse solute flux is as follows;

$$J_s = B\Delta c \tag{2.8}$$

where J_s, B and Δc are reverse solute flux, constant for solute permeability of the membrane and concentration gradient across the FO membrane.

For higher water fluxes, normally concentration of draw solutes is increased but this is not always favourable [112]. For example for sodium chloride salt, the solute flux reversal is intensified with increase in the concentration. Kim *et al.* [113] investigated that as the concentration of NaCl is increased which strengthens the osmotic driving force, both water flux and reverse solute flux are increased. The increased reverse solute permeation causes ICP in the support layer of membrane.

Reverse solute flux can be avoided or minimized either by developing such a membrane having a support layer which absolutely does not permit the solute permeation or increasingly diffuses it back to draw solution, or by suitable selection or development of solutes for the draw solution. The deciding features of the draw solutes include size of the draw solute ions/particles and their diffusion coefficients. Novel draw solutions need to be developed which exhibit minimum draw solute reverse diffusion and considerably increase water permeation by increasing the effective osmotic pressure difference.

2.3.3.2 Draw solute recovery

Under the effect of osmotic driving force, water permeates through the membrane and dilutes draw solution. This diluted draw solution is brought to the recovery system where clean water is separated and draw solution is concentrated, regenerated or recovered. Draw solution recovery and clean water separation is sometimes very complex and is another challenge for FO popularity and realization. Draw solution recovery basically depends on the type and nature of the draw solute being used.

A number of methods have been applied for this recovery including the use of volatile solutes like sulphur dioxide gas [114] and mixture of carbon dioxide, ammonia gases [96, 104, 115] and methyl ether [116] where thermal energy is used to evaporate the gases leaving clean water, magnetic separator [117-119] where magnetic nanoparticles were used as draw solutes and magnetic field was used for their separation, precipitation method [120, 121] where draw solution was precipitated to separate water and in some cases no regeneration is required [122]

where draw solution when diluted is directly used as drinking water in emergency situations.

Despite the increased water flux, each recovery method and draw solution has its own drawbacks including pungent smell in product water or its spoiled taste, toxic and harmful reaction products and decreasing osmotic pressure of the draw solution. Easily recoverable and long lasting draw solutions with high osmotic pressure are still needed to be developed and validated for bringing the advantages of FO in desalination field.

2.3.3.3 Lack of suitable FO draw solutions

The osmotic pressure gradient across the membrane is the driving force of a FO process. After a significant development in membrane technology, FO got the potential of being applied in various applications including water desalination, wastewater treatment, food industry and managing the brine produced by other desalination processes. Draw solution is the source of osmotic force to move water molecules through membrane from feed side. Various desirable properties of FO draw solutions include;

a. high osmotic pressure to have high water flux through the membrane,
b. minimum or zero reverse solute flux through membrane towards feed side,
c. minimum internal concentration polarization of the membrane,
d. easy recovery and
e. efficient product water separation.

Keeping these characteristics in consideration, numerous investigations have been carried out in the development of efficient draw solutions for FO. A brief summary of some of these investigations is presented in Table 2.4.

MNPs with three types of surface functional groups including; 2-pyrrolidone, triethylene glycol, and polyacrylic acid (2-Pyrol-MNPs, TREGMNPs, and PAA-MNPs respectively) were synthesized by thermal decomposition and investigated against HTI FO membrane with DI water as feed solution by Ling *et al.* [118]. Various concentrations were examined and the water flux increases with concentration in a non-linear manner. Out of these three surface capped MNPs, PAA-MNPs showed the highest water flux of 7.7 LMH which was thought of due to well dispersed nature of polyacrylic acid. However there was agglomeration and unsatisfactory recovery of small sized MNPs due to increased thick layer of polyacrylic acid.

In another study, Ling *et al.* [123] developed polyacrylic acid (PAA) and poly N-ispropyleacrylamide (PNIPAM) coated MNPs with COOH functional group either from NaOH or $Ca(OH)_2$. Water flux of PAA-MNPs was higher than that of PAA-PNIPAM-MNPs in either case when feed water is DI water or synthetic brackish water. The water permeation in case of brackish water as feed solution was much lower than that of DI water.

So far above mentioned few studies which have shown a number of problems arising from the use of MNPs as draw solutes in FO desalination. Though these investigations are preliminary results, they are facing the problem of agglomeration, reduced water flux after even 8 to 10 runs and recovery problem of the nanoparticles even after using high magnetic field and nano filtration. Hence there is a strong

prospective to develop and explore nanofluid based draw solutions using other nanoparticles which overcome these issues and make the draw solution regeneration and water separation easy and energy efficient.

Table 2.4 FO draw solutions with advantages and limitations.

Draw solution/Solute	**Advantages**	**Limitations**	**Ref.**
Ammonia-carbon dioxide	High water flux Moderate heat for recovery (60^oC)	Pungent smell of ammonia in output water	[115]
Polyacrylic acid (magnetic nanoparticles)	Easy separation of DS by applied electric field	Water flux is low MNP efficiency is decreased with time UF for recovery	[118, 123]
Stimuli responsive hydrogels	Thermal or pressure stimulus for recovery	High bacterial infection and hence cannot be practically used	[124]
Thermo responsive microgels	water flux as high as 23LMH high product water separation	centrifuging at high rpm is involved for product water recovery	[125]
Dimethyl ether	Energy effective	Draw solution is lost in product water separation Low water flux	[116]
Citrate-coated magnetic nanoparticles	Water flux as high as 17LMH	Reduced water flux with time Degradation of membrane due its reaction wit cit-MNPs	[117]

This table summarizes numerous FO draw solutes and their limitations due to they could not be practically implemented in the FO desalination process.

2.4 The novel concept of DANF based FO draw solutions

Despite of numerous plus points of FO over other desalination processes, there are a number of challenges including internal concentration polarization across the membrane, reduced water flux with the passage of time, developing draw solution with high osmotic pressure, recovery of product water from diluted draw solution and regeneration of draw agent as discussed in detail in above sections.

This work proposes an innovative concept: using DANFs as a novel draw solution that can efficiently absorb solar energy for their regeneration and provide sufficient osmosis pressure for increased water flux through the membrane and reduce reverse flux from draw agent side to feed side. Nanoparticle and their hybrids will be developed followed by coating with different polymers and disassociating their surface with different functional groups for enhanced dispensability and osmotic pressure for FO desalination. **Fig. 2.9** represents a schematic of the novel concept of draw solution based on different nanoparticles

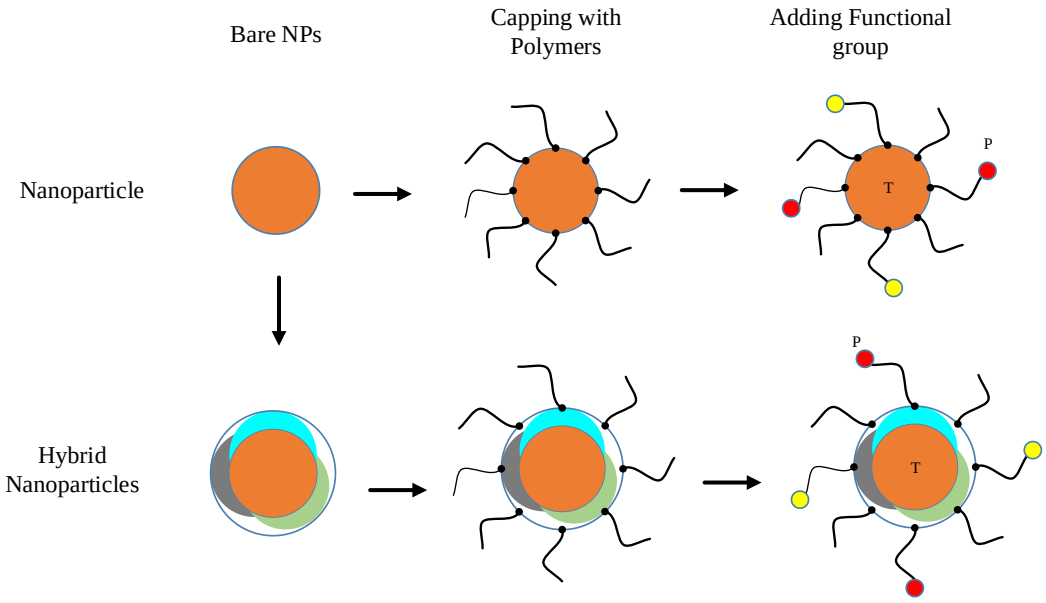

Figure 2. 9 Schematic of novel draw solution development process

Chapter 3
Synthesis and Characterization of Nanofluids

This chapter deals with the formulation and characterization of numerous nanofluids for enhanced direct solar absorption and osmotic pressure to work as novel draw solution for FO desalination. Objectively formulated nanofluids are characterized in terms of morphology, structure characteristics and elemental composition using various high performance techniques.

3.1 Introduction

Nanofluids are engineered colloidal suspensions of nanoparticles in a base fluid and can be prepared either by dispersing the respective nanopowders in a suitable solvent in the presence of a dispersant or they can be synthesized by the reaction of their precursors based on bottom up approach. The preparation of nanofluids by dispersing the nano powders usually using a bath or probe ultra-sonication is known as 'two step method' while formulation of nanofluids by the chemical reaction of their precursors is called one step method.

Direct solar absorptive nanofluids in this work have been formulated by one-step method using different modified methodologies including citrate reduction approach [126, 127] for the formulation of gold nanofluids, solution impregnation route [128] for core and shell nanoparticles. On the other hand, two-step method is followed where a suitable stabilizing agent or dispersant is used under ultra-sonication. The synthesized nanofluids are characterized in terms of their morphological appearance, structural characteristics and elemental composition using various techniques.

3.2 Formulation and characterization of nanofluids

3.2.1 Reagents and materials

All the reagents and materials were used as received without further purification. Commercial nanopowders of Ag, Cu and Zn (Sigma Aldrich Co.) and Fe, Si and Al_2O_3-γ (Nanostructured & amorphous material Inc.) were used as received to prepare nanofluids in deionized water. Tri-sodium citrate ($Na_3C_6H_5O_7$, 99.8%,

Fisher Scientific) and Sodium dodecyl sulphate ($NaC_{12}H_{25}SO_4$, 98%, Sigma-Aldrich) were used as the dispersant and stabilizing agents. Hydrogen tetra chloroauric acid ($HAuCl_4$. with Au ≥ 49%, Fisher Scientific) aqueous solution was used as precursor to synthesize gold nanoparticles by citrate reduction method. Silver nitrate ($AgNO_3$, Sigma Aldrich Co.) was used as precursor for the synthesis of core/shell silicon/silver nano composite with Si nanopowder.

Sulphuric acid (H_2SO_4, 95%) and nitric acid (HNO_3, 69%) were purchased from VWR Chemicals and were used as oxidizing agent for the surface functionalization of carbon nanofiber. Carbon nanofiber (CNF) [graphitized (iron-free) compressed in the form of conical platelets (D=100 nm, L=20-200 μm) Aldrich Chemistry, USA] and potassium hydroxide (KOH, Fisher Scientific) were used to synthesize potassium functionalized carbon nanofiber (K/CNF). Triethylene glycol ($C_6H_{14}O_4$, 99%, Sigma Aldrich Co.) was used as solvent for K/CNF to have as novel draw solution. Deionized (DI) water was used as the base fluid throughout the experimental procedure.

3.2.2 Characterization techniques

The nanofluids were characterized morphologically and their structural and compositional analysis was done by a combination of the following characterization techniques.

3.2.2.1 Scanning electron microscopy (SEM)

The SEM measurements were performed using a high performance cold field emission-scanning electron microscope (CFE-SEM, SU8230 Hitachi) equipped with an energy dispersive X-ray spectroscopy (EDS, Oxford INCA) to analyse the surface

morphologies, location of the elements and elemental compositions of the nanofluid samples.

3.2.2.2 Transmission electron microscopy (TEM)

The TEM measurements were carried out to produce micrographs of the nanoparticles by illuminating with an electron beam in a vacuum environment using FEI Tecnai TF20 FEG operated at 200 kV to analyse the surface morphologies. The TEM analysis can give a detailed information on morphological properties, structural and compositional behaviour of nanoparticles down to a particle size of 5 nm. One drop of the nanosuspension was put on a micro-copper grid covered with a thin layer of carbon and was dried at room temperature for TEM analysis.

3.2.2.3 UV/Visible spectrophotometry

Absorption spectroscopy technique is based on the radiation absorption as a function of wavelength due to its interaction with the sample particles. The variation in the absorption intensity as a function of radiation wavelength is called the absorption spectrum. The optical absorption of the nanofluid was examined by a UV/Vis spectrophotometers (UV-1800-Shimadzu and HITACHI, U-3900) using a high precision cell (light path of 10 mm).

3.2.2.4 Dynamic light scattering (DLS) device

Dynamic light scattering (DLS) technique is a well-recognized method of measuring the hydrodynamic size and zeta potential of colloids and nanofluids. DLS is based on the Stokes-Einstein mathematical relation ($d_h = {K_B T}/{6\pi\eta D}$, where d_h, K_B, T, η, and D are hydrodynamic diameter, Boltzmann constant, absolute temperature,

solvent viscosity and diffusion coefficient, respectively) which associates the size of a nanoparticle in a dispersant to its diffusion under the effect of Brownian motion of the particle. The hydrodynamic size was measured using Malvern zeetasizer. Disposable cuvettes were used for the measurement of hydrodynamic size of the nanoparticles in the dispersant.

3.2.2.5 Fourier Transform infrared (FTIR) spectroscopy

The identification of the functional groups on the prepared nanofluid samples were examined at room temperature on a Nicolet iS10 FTIR spectrometer with a resolution of 4 cm^{-1}, in the ranges of 500 to 4000 cm^{-1} and the final output was in %Transmittance.

3.2.2.6 Thermo-gravimetric analysis (TGA)

The thermal stability of nanofluid samples was performed on the TGA/DSC-2 instrument (Mettler Toledo, England) where (20±5) mg of sample was weighted in a 70 μL alumina crucible and placed in the TGA/DSC-2 sample holder. Experiment was conducted under a constant flow rate (50 ml/min) of nitrogen purge gas and the sample was heated in the temperature range of 30 to 900 °C at a ramping temperature of 10 °C/min.

3.2.2.7 X-ray diffraction (XRD)

The XRD analysis was carried out on a powder Bruker's advanced D8 diffractometer using CuKα radiation (λ=1.5418 Å) to determine the crystal structures of nanofluid samples. The operation voltage and applied current for the XRD instrument were maintained at 40 kV and 40 mA, respectively. The samples

were loaded onto the sample holder and scanned at 2θ angle range from 5^{o} to 80^{o} with step size 0.035 at 30 sec per step.

3.2.3 Nanofluids from nanopowders

A number of nanoparticles dispersed in different media have been used for direct solar energy absorption under varying experimental conditions, as described in Section 2.2. The most commonly used nanoparticles having good solar absorptivity are selected to investigate their photothermal performance under the same experimental conditions. Table 3.1 enlists these nanoparticles which include silver, copper, zinc, iron, silicon and aluminium-γ. The photothermal behaviour of these six nanoparticles are experimented with 0.01 wt% concentration and their performance is compared in Chapter 4.

Table 3. 1 Particle size range of various nanofluids

Nanomaterial	**size range**	**Supplier**
Cu	35-45 nm	Sigma Aldrich
Ag	50-60 nm	Sigma Aldrich
Zn	40-60 nm	Sigma Aldrich
Si	30-50 nm	Nanostructured & amorphous material Inc.
Fe	50-80 nm	Nanostructured & amorphous material Inc.
Al_2O_3-γ	40-80 nm	Nanostructured & amorphous material Inc.

Commercial nanopowders of six materials including Ag, Cu and Zn (Sigma Aldrich Co.) and Fe, Si and Al_2O_3-γ (Nanostructured & amorphous material Inc.) were used as received to prepare the respective nanofluids by two step method. Tri-sodium citrate (99.8%, Fisher Scientific) was used as the dispersant and stabilizing agent and DI water was used as the base fluid throughout the experimental procedure. The

primary particle size range of the nanopowders as supplied by the suppliers is given in Table 3.1.

Nanofluid of the selected nano powdered materials were prepared by two-step method. In this method, selected nanopowders were directly mixed with a 0.5 wt% of tri-sodium citrate (TSC) solution in DI water. For instance, to prepare a nanofluid of 0.01% weight concentration, 0.01 g nanopowder was mixed with 99.99 g of 0.5 wt% aqueous solution of tri-sodium citrate as a dispersant under vigorous stirring. The acquired mixture was sonicated by a high energy probe (1200 W) for 5 minutes where the temperature was controlled at 40 ^{o}C. The suspensions were then cooled down naturally to room temperature and were sonicated for 10 min before the photothermal conversion experiment.

Morphological characterization of the nanopowders is given in **Fig. 3.1** where **Fig 3.1 (I)** (a through f) shows SEM (scanning electron microscopy) images of the nanopowders and **Fig. 3.1 (II)** gives TEM (transmission electron microscopy) micrograph of silver nanopowder dispersed in 0.5% aqueous solution of TSC. The nanopowders were mostly clustered before the dispersion but became completely dispersed in DI water in the presence of stabilizing agent after sonication. The experimental results of photothermal behaviour of these nanofluids are presented and explained in sections from 4.3.1 to 4.3.4 in Chapter 4.

3.2.4 Si/Ag hybrid nanofluid

The synthesis of Si/Ag core/shell hybrid nanoparticles was completed in two phases. The first phase included the dispersion of Si nanopowder with a particle size between

40 nm and 100 nm. The second step in the core-shell fabrication process was to coat the Si nanoparticles with Ag through solution impregnation technique.

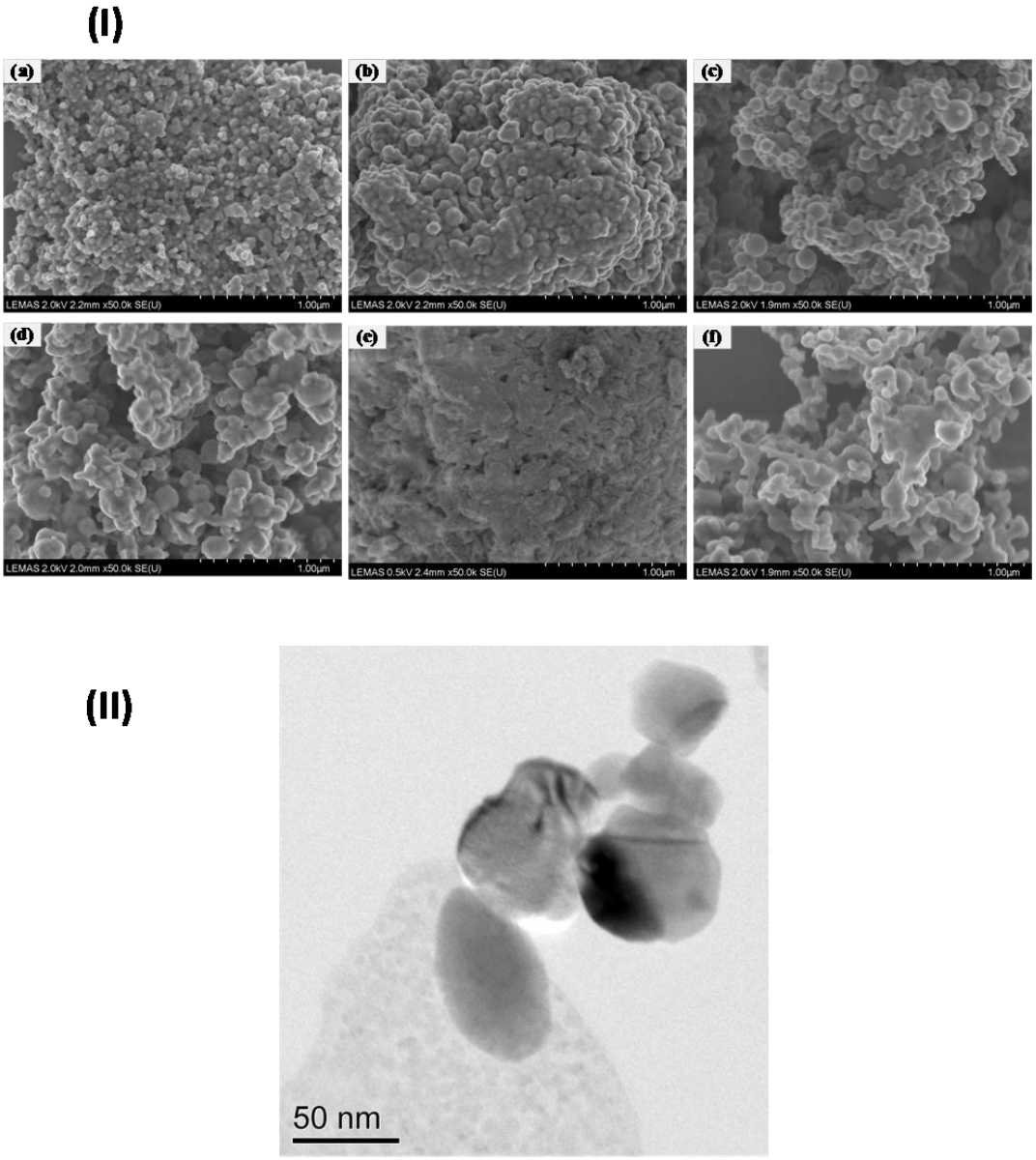

Figure 3. 1 Morphological appearance of nanopowders (I) SEM images of nanopowders of (a) Copper, (b) Silver, (c) Iron, (d) Zinc, (e) Aluminium oxide-γ and (f) Silicon and (II) TEM micrograph of silver nanoparticles dispersed in deionized water.

This is a modified methodology developed by Kumar et al. [128] where 1 g of Si powder was dispersed with 100 ml of 0.25 M $AgNO_3$ (as a source of Ag NPs) under vigorous stirring. To complete the solution impregnation process, the mixture was allowed for at least 36 hours stirring at room temperature. The solution was then calcined in a muffle furnace at 700 ^oC for 2 hours. A light grey powder was obtained which was re-dispersed in de-ionized water to get a desired concentration.

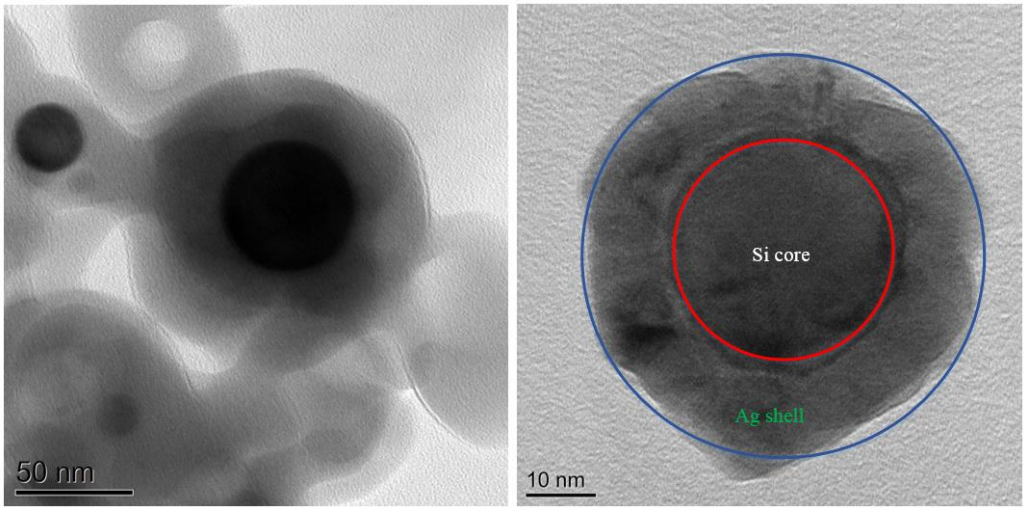

Figure 3. 2 TEM micrographs of the core/shell Si/Ag nanoparticles at different magnifications

For morphological analysis on TEM, holey Au grids were used where a drop of the core/shell Si/Ag hybrid nanofluid was dried on shiny side of grid before further analysis. TEM micrograph **Fig. 3.2** clearly shows that Si nanoparticles are coated with Ag. The inner dark round area in red circle in Fig. 3.2 (right side) is the Si core while the light cloud in blue circle around the dark core is coating of silver. The presence of Si and Ag is also confirmed by EDX spectrum as shown in **Fig. 3.3**. The droplet evaporation rate of the sessile droplet on a glass substrate and their resulting deposition patterns are given in section 4.3.5 of Chapter 4.

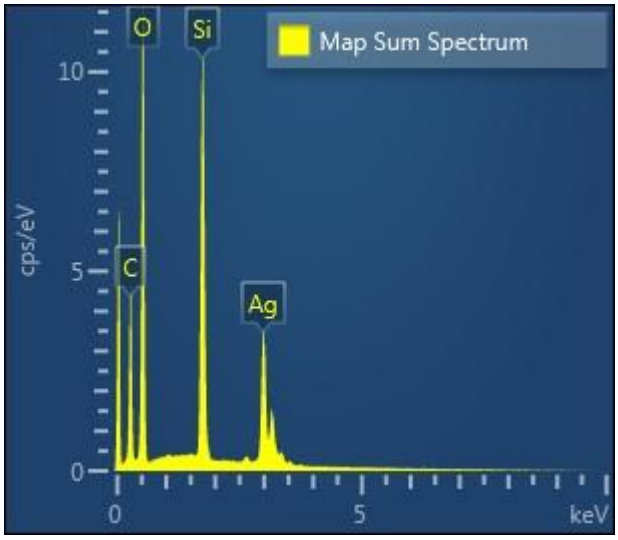

Figure 3. 3 Elemental analysis using Energy Dispersive X-ray (EDX) spectroscopy

3.2.5 Gold nanofluid by citrate reduction method

Gold nanoparticles (GNPs) were synthesized by one-step based on a modified thermal citrate reduction method as reported by Zhang at el. [21] and Chen et al. [129]. In the synthesis process as shown in **Fig. 3.4**, 100 ml of 5mM $HAuCl_4$ solution was mixed with 100 ml of 10 mM tri-sodium citrate solution. The resultant mixture was heated to the boiling point until the mixture turned to wine red colour. The resultant solution was continuously heated at 80 ^oC in a sonication bath for further 3 hours. Synthesized GNPs were aged at room temperature for 24 hours for stability and cleaned by dialysis from 8 kDa membrane. The membrane allows the excessive ions to diffuse smoothly from the suspension and blocks the GNPs. DI water was changed twice a day for a period of 10 days, leading to pure GNPs dispersions. The concentration of the resulting nanofluid was measured by Atomic Absorption Spectrometry (AAS, VARIAN, AA240FS).

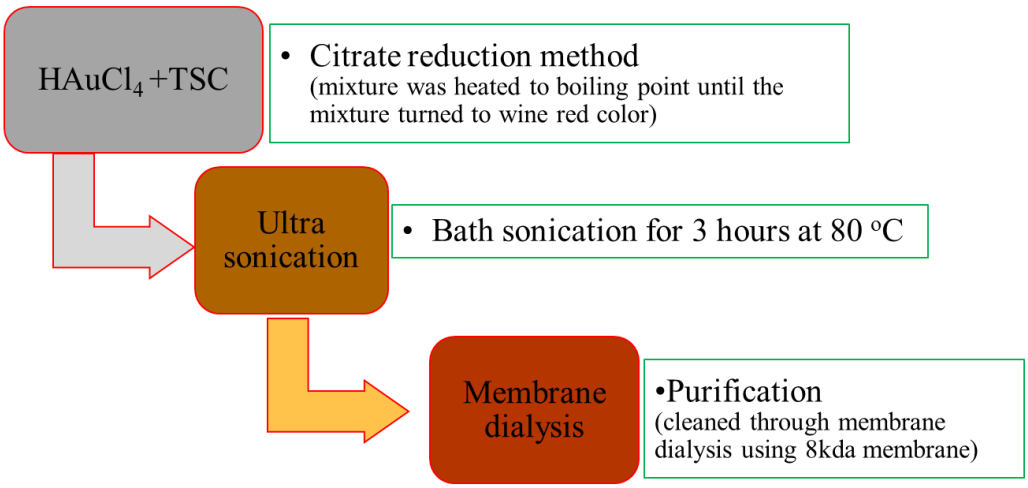

Figure 3.4 Synthesis methodology of Au nanofluid

The morphology of the synthesized nanoparticles was analysed by a transmission electron microscopy (TEM) (TECNAI, TF20) equipped with EDX (Energy Dispersive X-ray spectroscope) and the hydrodynamic size was measured by the DLS device. **Fig 3.5 (a)** shows the TEM image of the nanoparticles and the inset shows a closer view. It can be seen that the gold nanoparticles are mostly spherical with particle size in the range of 20~ 30 nm. The hydrodynamic size distribution of the gold particles (**Fig. 3.5 (b)**) is slightly larger size than that from TEM size, which is due to the hydrodynamic nature of size measurement by DLS.

The experimental results on gold nanofluid based direct solar steam generation are discussed in chapter 5 and an improved technique to calculate the photothermal efficiency is proposed in addition to the effect of the number and position of thermocouples.

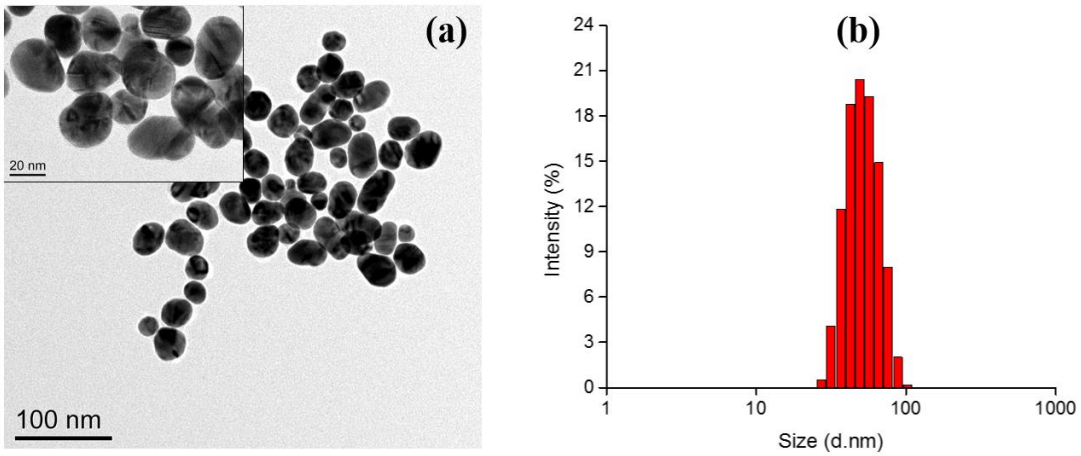

Figure 3.5 Characterization of the synthesized gold nanoparticles, (a) TEM image of the gold nanoparticles showing a good suspension and size variation and (b) hydrodynamic size distribution of the gold nanoparticles measured by DLS.

3.2.6 K-functionalized carbon nanofibers (K/CNF)

Surface functionalization of carbon nanofiber (CNF) is an effective route to introducing some crucial functional groups on the internal or external surface to increase the hydrophilicity. 5 g of CNF [graphitized (iron-free) compressed of conical platelets with diameter and length of 100 nm and 20-200 µm respectively] was immersed in a 80 ml of nitric acid:sulfuric acid (1:3, v/v) at 70 ºC for 6 hour under stirring at 250 revolution per minute. The obtained solution was then filtrated and washed several times with DI water followed by drying in a vacuum-oven at 80 ºC overnight. The resulting of treated-CNF powder was suspended in a 50 ml of 0.05 M aqueous sodium dodecyl sulphate (SDS) solution and sonicated for 30 min. Subsequently, 250 ml of 0.5 M KOH aqueous solution was added drop wise to the dispersed treated-CNF solution and the reaction mixture was then refluxed for 16 h. The synthesis route is also presented schematically in **Fig. 3.6**.

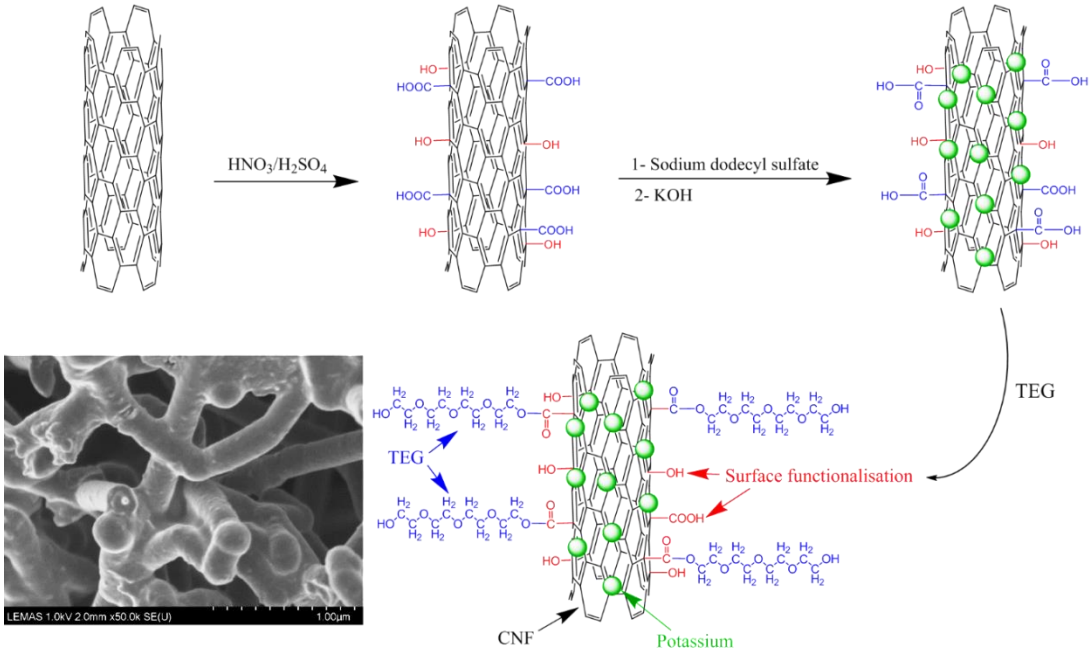

Figure 3. 6 Schematic synthesis route of TEG-K/CNF novel draw solution

After normalizing to room temperature, a black solution was obtained. The as-obtained particles were separated from the solution using Megafuge at 11000 RPM and extensively washed with 1:1 methanol to DI water until the pH of the filtrate reached a value of 7. The separated grey-black gel then oven-dried at 80 ºC for 24 hr and upon normalizing to room temperature it was crushed to have K/CNF powder.

The measured weight of K/CNF powder was dispersed in different volume concentrations of TEG ranging from 0.05 to 0.2 wt% concentrations. The resultant mixture was probe sonicated for 5 min to completely disperse the K/CNF in TEG aqueous solution. The TEG-K/CNF mixture was very stable even over a period of three months.

Fig. 3.7 shows the FTIR spectra of CNF, K/CNF and TEG-K/CNF samples. CNF sample had almost not much bands because the CNF acted as a very effective black

body absorber [130]. In case of K/CNF and TEG-K/CNF, there were several extra characteristic peaks related to generate functional groups on the surface as well as K-species doping into the structure of CNF as shown in **Fig. 3.7**. The strong broad bands at ~3150 cm^{-1} were associated to the –OH and –COOH groups on the surface of CNF structure as well as the free –OH end group of TEG structure attached to the surface of acid treated CNF [130-132]. The bands at ~2950 and ~2850 cm^{-1} could attribute to the asymmetric and symmetric stretching of –C-H groups, respectively, in TEG molecules functionalised CNF [133]. There were few weak peaks at ~2090 to 2390 cm^{-1} that could be assigned to the asymmetric stretching of CO_2 molecules. An additional new peak appears at ~1735 to 1750 cm^{-1} and could be related to the C=O stretching in carboxylic and carbonyl groups [130] The band at ~1650 cm^{-1} was ascribed to the C=C stretching in the main CNF structures. The band at ~1600 cm^{-1} was related to the H-O-H symmetric vibration of water molecules absorbed on the surface of K/CNF and TEG-K/CNF structures. The band at ~1440 cm^{-1} was assigned to the C-H bending of TEG groups in TEG-K/CNF. The new peak at 1350 cm^{-1} was related to the C-O stretching but the band at around 1200 cm^{-1} was assigned to the C-C stretching [133]. The sharp peak at 1060 to 1010 cm^{-1} was corresponded to the C-O bending in ether whilst the one at 840 cm^{-1} could be attributed to the –OH in carboxylic groups [130]. The intensity of this peak (at 840 cm^{-1}) in TEG-K/CNF reduced after surface functionalization with TEG [133]. This confirmed the formation of ester bond between –COOH on the surface of CNF and –OH groups of TEG molecules.

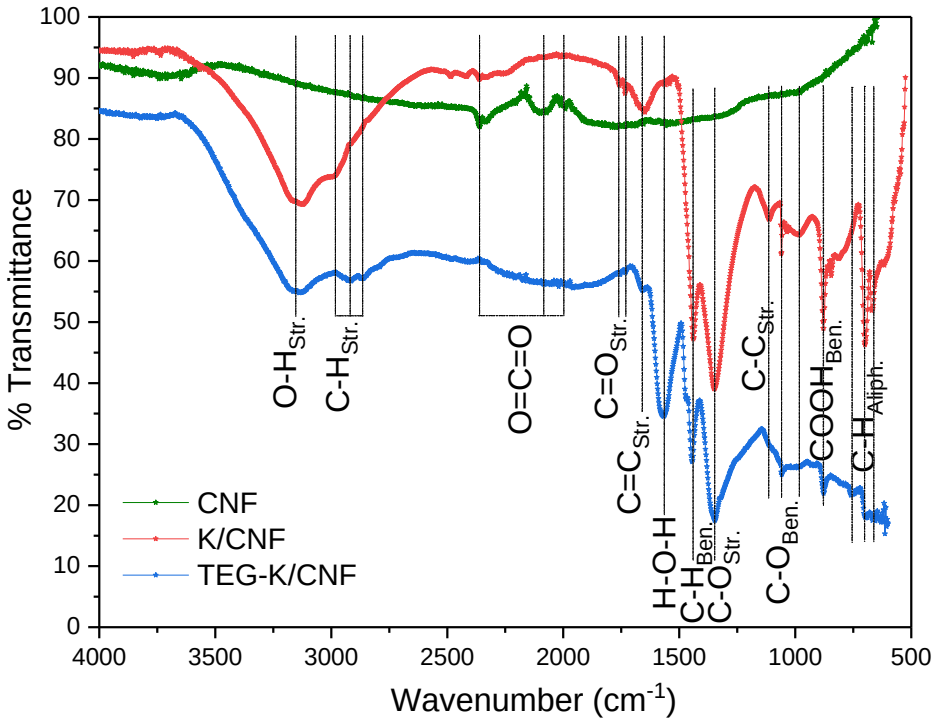

Figure 3. 7 FTIR spectra for CNF, K/CNF and TEG-K/CNF samples

The several bands at about 765, 685, 650 and 600 cm^{-1} were attributed to the aliphatic C-H bending [134]. This result clearly indicates that the surface of K/CNF was successfully functionalised with TEG molecules. The attachment of –COOH, -OH and K groups onto the surface of CNF has a strong effect on the stability of synthesised sample in aqueous medium and are the major reason for the enhancement of osmotic pressure.

The morphologies of CNF, K/CNF and TEG-K/CNF samples at different magnifications are shown in **Fig. 3.8**. The SEM images of unmodified CNF as shown in **Fig. 3.8 (a)** at different magnifications demonstrated that the surface of CNFs was smooth and confirming the used CNF sample had short and long filled cylindrical chains of fibre covalently bonded carbon atoms which possess hydrophobic properties. The formation of the short and long filled cylindrical chains

with observed channels can be attributed to the nature of the synthesis of nanofibers from different polymers.

Whereas, the morphology of potassium functionalized carbon nanofiber (K/CNF) was different (roughness of the side cylindrical chains) and the carbon fibres were thicker than unmodified CNF sample. This phenomenon may be related to the surface treatment of CNF with strong acidic mixture (H_2SO_4 and HNO_3) to form carboxylic/hydroxyl groups on the surface as well as K-species embedded in the CNF as shown in F**ig. 3.8 (b)**. Having K-species doped, -COOH and –OH on the structure of CNF lead to increase the hydrophilicity of synthesised material which caused an increase in the osmotic pressure. In case of TEG-K/CNF, it can be clearly seen that there was a complete surface coverage of K/CNF with TEG to form spongy morphology as shown in **Fig. 3.8 (c)**. This is further confirmation that the surface of K/CNF were successfully functionalised with TEG molecules. Addition of TEG molecules to the surface of K/CNF leads to increase –O– and –OH groups which would further increase hydrophilicity of TEG-K/CNF surface.

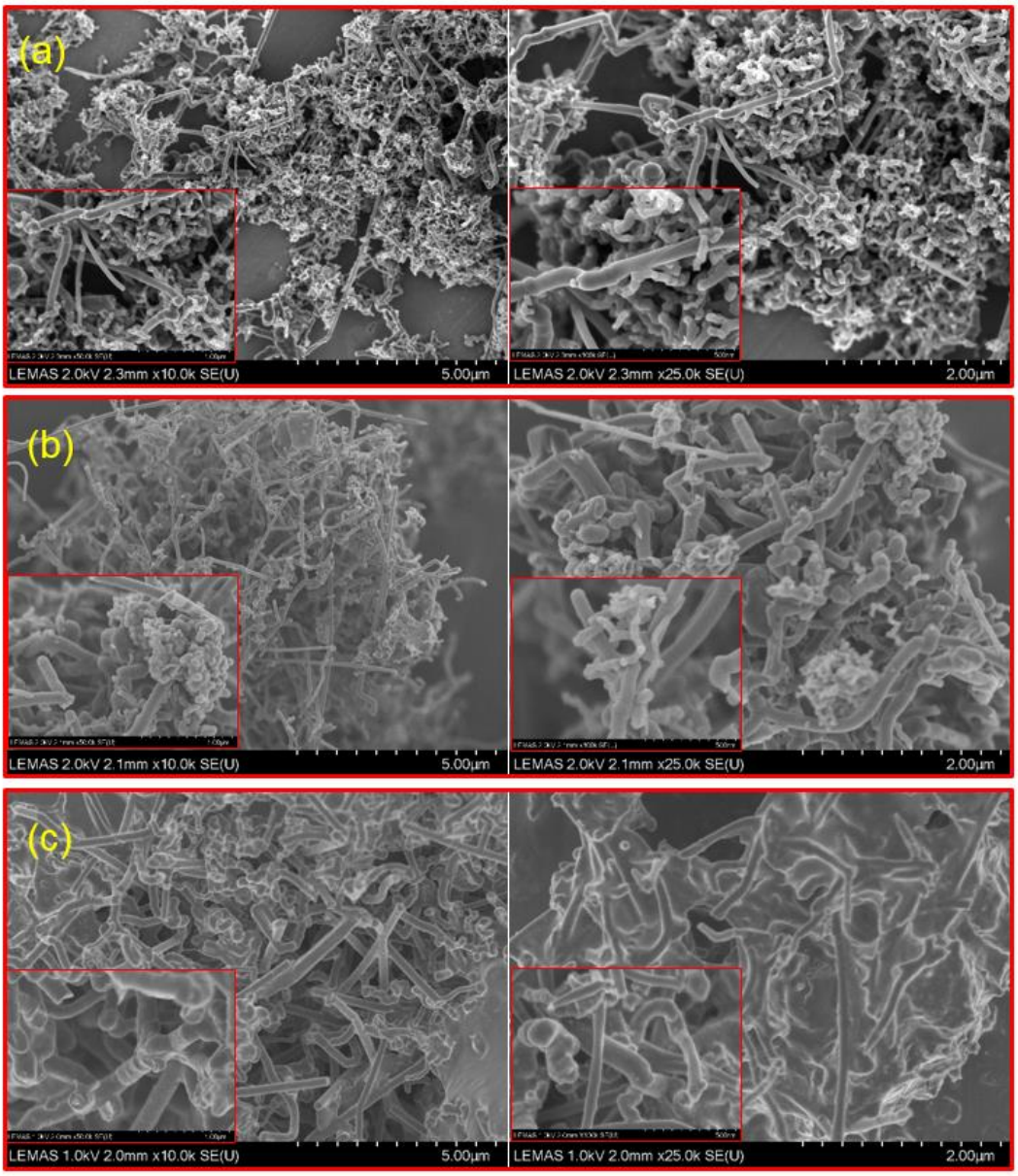

Figure 3. 8 SEM micrograms for (a) CNF, (b) K/CNF and (c) TEG.K/CNF at different magnifications

The elemental analysis of K/CNF using SEM-energy dispersive X-ray spectroscopy (EDX) revealed that the synthesised K/CNF consisted of carbon, oxygen and potassium elements as shown in EDX spectrum in **Fig. 3.9**. The K-species were

evenly distributed throughout the elemental mapping (**Fig. 3.10**). This confirms the successful decoration of CNF with potassium in the synthesised K/CNF.

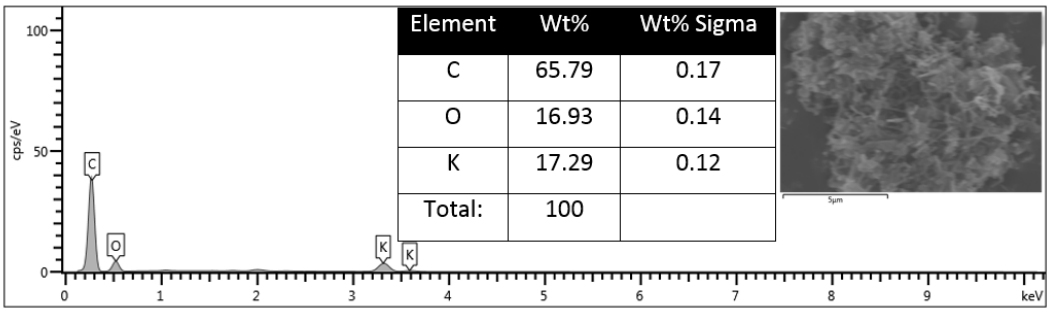

Figure 3. 9 SEM-EDX for K/CNF sample

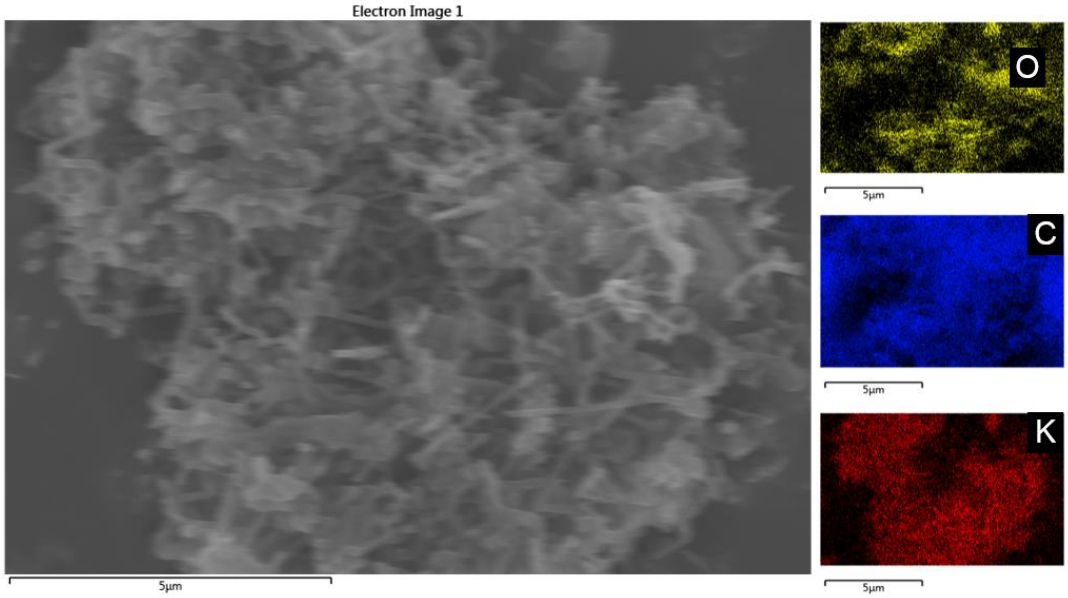

Figure 3. 10 EDX-mapping for K/CNF sample

Fig. 3.11 presents the XRD pattern of CNF, K/CNF and TEG-K/CNF samples. It can be seen that the two broad diffraction peaks at 2θ of 25° and 44° corresponding to [002] and [101] in the structure of CNF, respectively [135]. It can be clearly seen that were massive changes in the crystal structure of synthesised K/CNF and TEG-

K/CNF materials in comparison with unmodified CNF. In addition, there was no difference between the XRD pattern of K/CNF and TEG-K/CNF samples. However, the peak intensities reduced after modification with TEG as a results of surface coverage of K/CNF with TEG.

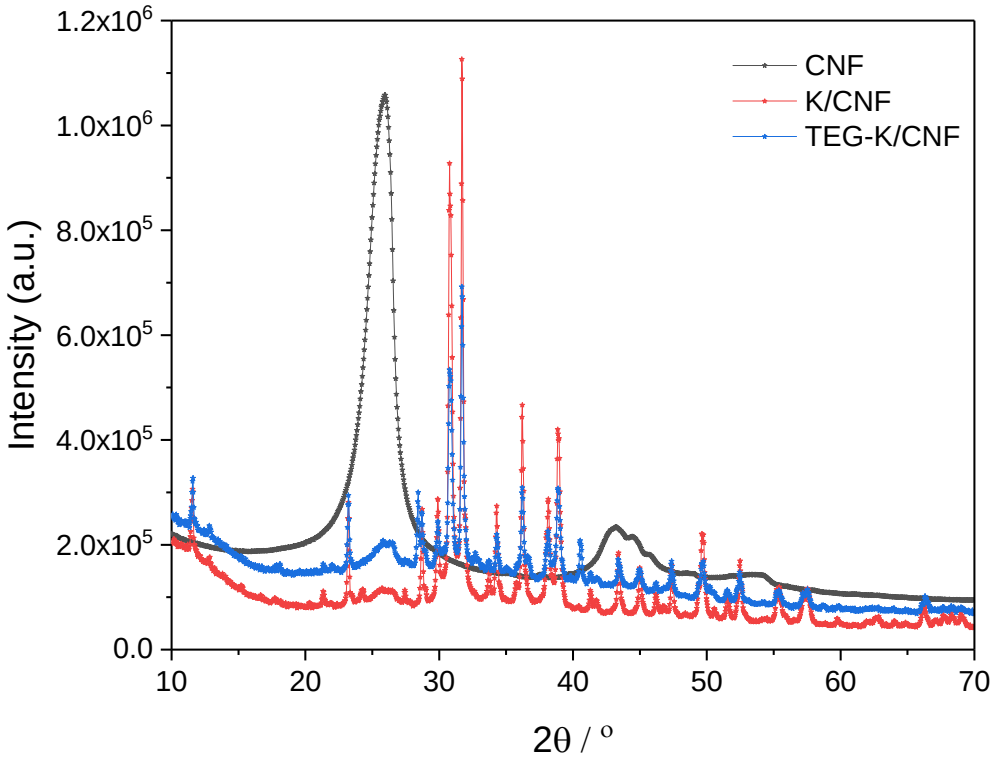

Figure 3. 11 XRD patterns for CNF, K/CNF and TEG-K/CNF at room temperature

The thermal behaviours of the synthesised TEG-K/CNF sample and that of their precursors were investigated and the corresponding TGA curves are given in **Fig 3.12**. It can be seen that the unmodified CNF sample was very stable and did not show any dramatic decomposition in the range of 30 to 800 °C and then a slight weight loss could be observed. In case of K/CNF, three step of weight loss were observed. The first step began at 90-140 °C due to possibly desorption of water molecules and the second one at 140-175 °C associated with the decomposition of

carboxylic and hydroxyl groups on the surface of K/CNF as well as the remained sodium dodecyl sulphate.

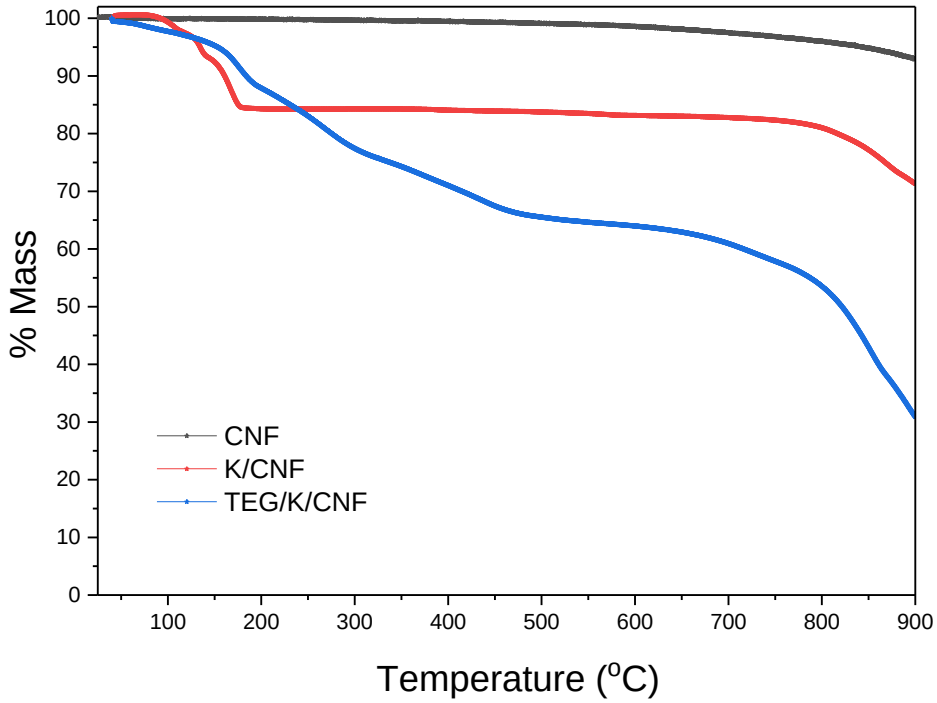

Figure 3. 12 TGA curves for CNF, K/CNF and TEG-K/CNF

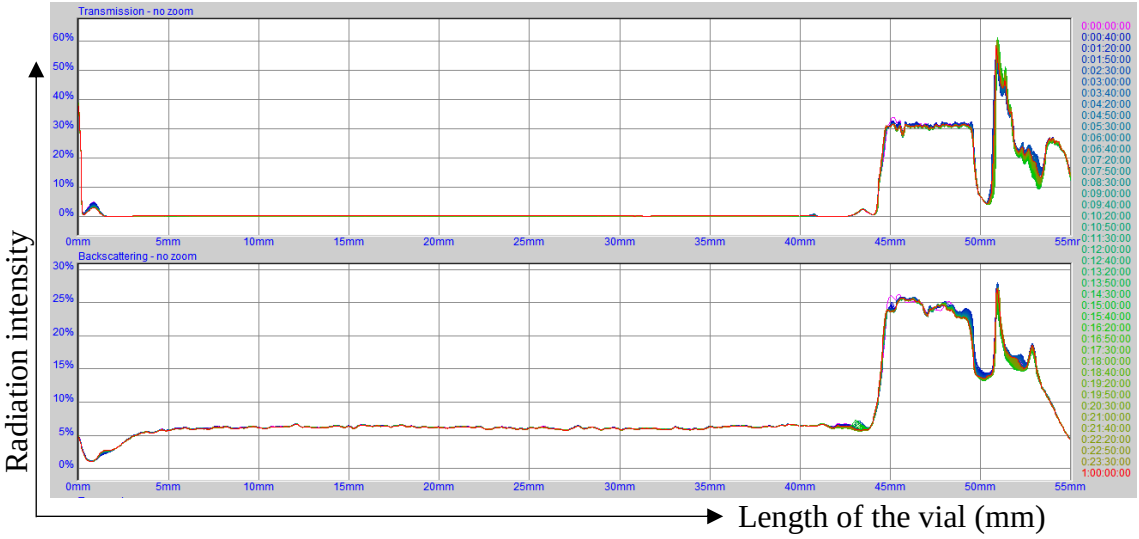

Figure 3. 13 Transmission and backscattering spectra from Turbiscan over a period of 24 hours showing a very good stability of the K/CNF sample

The final step started at 800 °C due to the partial decomposition of CNF structure. It is evident that the degree of acidic functionalization of CNF from the mass loss suggests that the CNF has been functionalised around 14 wt% with –COOH and –OH groups. In contrast, the characteristic TGA curve of TEG-K/CNF exhibits a four step weight loss. The TGA curve of TEG-K/CNF were exactly similar to that of K/CNF apart of rapid weight loss (~28 wt%) at 175 to 450 °C assigned to the decomposition or detachment of TEG functional groups [133] on the surface of K/CNF.

The stability of the K/CNF sample was checked using Turbiscan (Formulaction, France) which measures the sedimentation rate by using turbidity measurements of backscatter and transmission to assess the stability of the sample. The transmission and backscattering spectra as given in **Fig. 3.13** shows no sedimentation over a period of 24 hours with scanning after every 40 minute interval. All the scans are overlapped both in transmission and backscattering spectrum showing a high stability of the sample.

The FO performance including osmolality and osmotic pressure, water permeation flux, reverse solute flux and the photothermal behaviour of these novel draw solutions are presented in chapter 6.

3.3 Chapter summary

Various nanofluids to be used for the evaluation of photothermal characteristics, steam generation and FO performance were synthesized and characterized by various techniques. Nanofluids prepared from nano powders include silver, iron,

zinc, silicon, copper and alumina while gold nanofluid was synthesized by one step method using citrate reduction approach. Si/Ag hybrid nanofluids were formulated by solution impregnation process and graphene nano platelets were synthesized by modified Hummer's synthesis route. All of the formulated nanofluids were completely synthesized in terms of morphology, structure, stability and elemental composition using SEM, TEM, EDX, XRD, FTIR, TGA and DLS before using them in further experiments.

Chapter 4
Nanofluid based Direct Solar Absorption and Droplet Evaporation

This chapter deals with the experimental performance of direct solar absorptive nanofluids at bulk volume as well as on micro droplet scale. Various plasmonic and non plasmonic nanofluids and their hybrids are investigated in terms of direct solar absorption under various solar flux conditions.

4.1 Introduction

The phenomenon of direct solar absorption is based on the absorption of solar energy directly by the working fluid instead of being absorbed by an absorbing plate and then transferred to the working fluid by convection as in conventional solar thermal collectors. As the commonly used heat transfer working fluids are poor absorbers of solar energy in the visible and near infrared range of solar spectrum, their efficiency can be significantly enhanced by suspending various nanoparticles and tuning their absorption properties.

Properly tuned nanofluid in terms of their photothermal properties can significantly enhance the solar energy absorption and a number of studies have been conducted in this context under different experimental conditions and various concentrations as outlines in Table 4.1 and briefly explained in Chapter 2. Moreover, Vakili et al. [136] used deionized water based graphene nanofluid with concentration up to 0.005 wt% for solar energy harness and concluded that the percentage absorption and conductivity are directly dependent on the volume concentration of graphene nano platelets. Similarly Chen et al. [137] deployed water based reduced graphene oxide nanofluid with a 0.02% mass fraction for the analysis of their photothermal performance for low temperature direct absorption solar collector. It was concluded that the reduced graphene oxide nanofluid was better in photothermal performance than that of graphene oxide nanofluids. Chen et al. [138] prepared bimetallic nanoparticles composed of plasmonic Au and Ag for enhanced photothermal conversion and could only achieve 31.41% photothermal efficiency over the basefluid.

Table 4. 1 Various nanofluids used with different concentrations in photothermal experiments under varying experimental conditions

Authors [Ref]	Nanoparticle	Concentration		
		From	To	units
Zhang et al. [21]	Au	0.00028	0.0112	wt%
Bandarra et al. [22]	Ag	0.0001625	0.065	vol%
Gupta et al. [11]	Al_2O_3	0.001	0.05	vol%
Menbari et al. [139]	CuO	0.002	0.008	vol%
Yousefi et al. [23]	Al_2O_3	0.2	0.4	wt%
Qenbo et al. [140]	Cu	0.001	0.02	vol%
Said et al. [25]	Al_2O_3	0.05	0.1	vol%
Saidur et al. [141]	Al	1.0		vol%
Yousefi et al. [142]	MWCNT	0.2		wt%

Each of the above mentioned studies was based on only one particular type of particle. A comparative assessment of the performance of commonly used nanomaterials for solar energy harness is much needed. The effect of these nanomaterials must be investigated at the same concentration and under similar operating conditions to reveal their photothermal conversion performance.

On the other hand, how the presence of nanoparticles in a liquid droplet having fluorescent particles, affect the flow and evaporation dynamics under a week radiation flux was also investigated. The hybrid nanoparticles in the form of core and shell have been used to investigate the evaporation rate, flow dynamics and resulting deposition patterns in a sessile micro droplet under a weak radiation flux. The micro droplet evaporation is experimentally investigated to understand the effect of nanoparticle presence on the flow dynamics, contact line movement and

resulting disposition patterns and to relate this micro droplet evaporation to the surface or pool evaporation case as in chapter 5.

Experiments were performed to investigate the photothermal performance of a number of deionized water based nanofluids as well as core/shell Si/Ag hybrid nanoparticles in the presence of fluorescent tracers in a micro droplet under a simulated solar flux. The photothermal performance of nanofluids was studied in terms of their sensible heating, evaporating capability, specific absorption rate and enhancement in photothermal efficiency over the base fluid while the effect of adding nanoparticles in a micro droplet was investigated to reveal their influence on the photo absorption, fluid flow, and resulting deposition patterns using a novel experimental study. The deposition patterns of the nanofluid droplet after the evaporation are obtained with the help of tracer particles using a unique total internal reflection fluorescence microscopy (TIRFM) setup.

4.2 Experimental setup

The photothermal conversion characteristics of the prepared nanofluids were investigated using a solar simulator (Newport Co.). It has a class AAA certification to JIS C 8912, and ASTM E 927-05 standards, which has a 450W xenon lamp as the light source and spectral correction filters (known as Air Mass filters) to correct the light output to closely match the solar spectrum. An air mass filter AM1.5G was used to simulate the direct solar spectrum with the Sun at a zenith angle of 48.20 (ASTM E891). The sun simulator has a spectral match 0.75-1.25% fraction of ideal percentage, 2% non-uniformity of irradiance and ± 2% spectral instability according

to ASTM Class AAA standard. A schematic view of the experimental setup is presented in **Fig.4.1**.

A petri dish of 5.8 cm diameter was used to contain the sample. The bulk temperature change was measured by three K-type (Omega 5TC-TT-K-36-36) thermocouples (TC), which were positioned at three representative depths: just under the top surface of the fluid (TC1), at the middle (TC2) and close to the bottom of the petri dish (TC3). A fourth thermocouple was used to measure the variation of room temperature. The data were registered by a data acquisition device (NI SCXI-1303) under the LabVIEW environment at a sampling rate of 1 Hz. The uncertainty in temperature measurement was calibrated as ±0.5 ^{o}C. The sample container was rinsed with DI water before each experiment to avoid inter-sample contamination.

A Fresnel lens of 5.5 x 5.5 inch^2 with a focal length of 10 inch was used to focus the output light onto the nanofluid sample. The focused intensity of light was measured as 12 suns (one sun being ~970 W/m^2) with the help of a solar intensity meter.

The fluorescent particles in hybrid with Si/Ag nanoparticles were illuminated by an evanescent wave having exponentially decaying intensity along the distance normal to the wall using an inverted microscope (Olympus, IX71), total internal reflection fluorescence microscopy (TIRFM) and MnPIV technique. The concept of evanescent wave, TIRFM and MnPIV is already discussed in chapter 2.

The tracers in this work are used as florescent particles i.e. to make the flow visualization possible and to capture the deposition patterns because they glow when irradiated with laser light. The radiation absorptive nanoparticle (Si/Ag) size is too small to be visualized in the TIRFM setup.

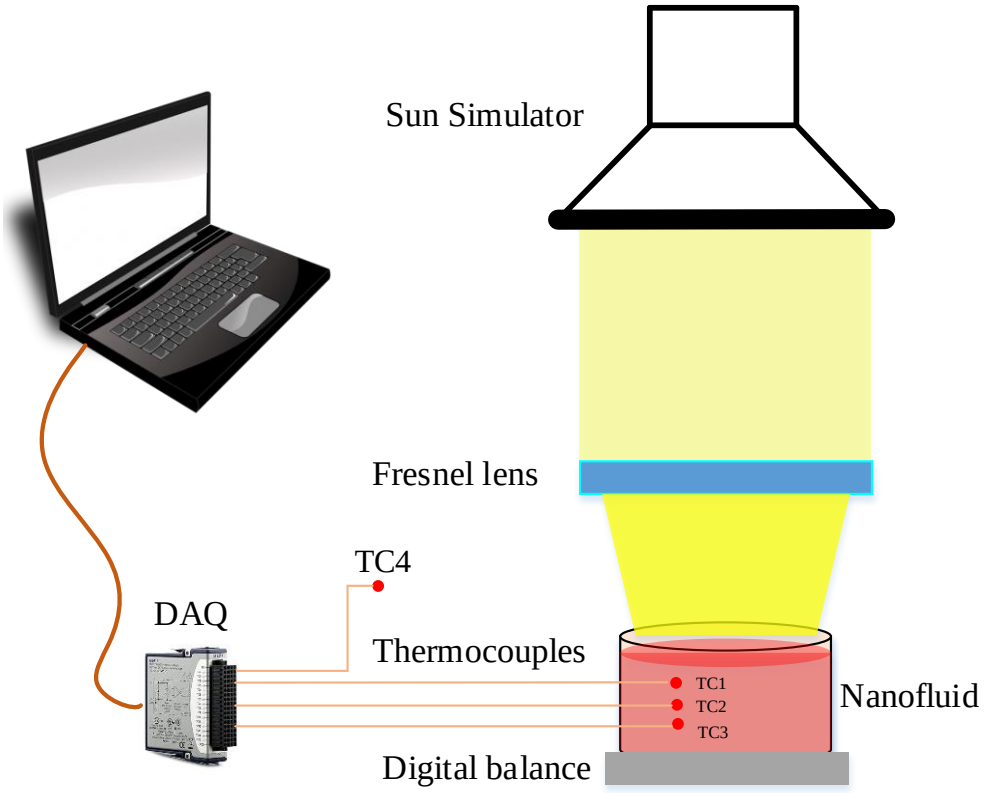

Figure 4. 1 Schematic view of the experimental setup showing the position of thermocouples and arrangement of Fresnel lens under a solar simulator

The glass coverslips used as substrate were cleaned with deionized water followed by a 30 min sonication in ethanol solution. To make it highly hydrophilic, the glass substrate was treated with piranha solution (3:1 volume ratio of 98% H_2SO_4 and 30% H_2O_2) in a sonication bath for 30 min at 80 ^oC. For the case of near wall motion analysis of the tracer particles in the nanoparticle hybrid droplet and their subsequent dry patterns, the ambient temperature and relative humidity were maintained at 22 ± 1 ^oC and 40 ± 1% respectively.

The evanescent illumination was obtained from a continuous wave solid laser (Coherent, FV5-LA-AR) coupled with an optical fibre at a wavelength of 488 nm.

A penetration depth (as detailed in chapter 2) of 86 nm was achieved by a total internal reflection fluorescence (TIRF) objective lens having magnification of 60x. The optical fibre had a coupling efficiency of about 65% and the laser output power was >5 mW. An epifluorescent bandpass filter cube (Chroma Tech, HQ550/40 m) isolates the polystyrene emissions. The bandpass filter transmits light at 512 nm wavelength and reflects the 488 nm radiance which is imaged by the TIRF objective at 15 mS exposure time on to EMCCD (Electron multiplying charge coupled device, Andor, IXON 3 Ultra). The EMCCD recorded 16 bit 256 × 256 pixels images at an electronic gain of 8 and framing rate of about 62 Hz. The imaging system with 60x magnification has field view of 68.26 × 68.26 μm^2. The excitation light with a very small intensity (5mW) has a negligible influence on the droplet evaporation which was also confirmed by recording the total drying time with and without excitation light under the same ambient conditions. A schematic of the TIFRM setup is given in **Fig. 4.2** and a photo of the inverted microscope is shown in **Fig. 4.3**.

The experimental procedure includes the following steps:

i. lubricating the TIRFM objective lens with appropriate volume of immersion oil,
ii. placing the prepared glass coverslip (substrate) on the TIRFM objective,
iii. dripping a drop 0.5 µL of nanofluid with a precise micropipette (Fisher Scientific) on the substrate,
iv. adjusting the objective lens to bring the bottom most part of the droplet in focus,

v. adjusting the incident angle of the excitation light for the generation of an evanescent wave at the lowermost part of the substrate for total internal reflection and bringing the objective lens in perfect focus,

vi. recording the particle motion information through EMCCD with an interval of 10 second till the complete evaporation of the droplet,

vii. image processing using standard algorithm of particle velocimetry, and

viii. changing the nanofluid concentration by following the steps (ii) through (vii).

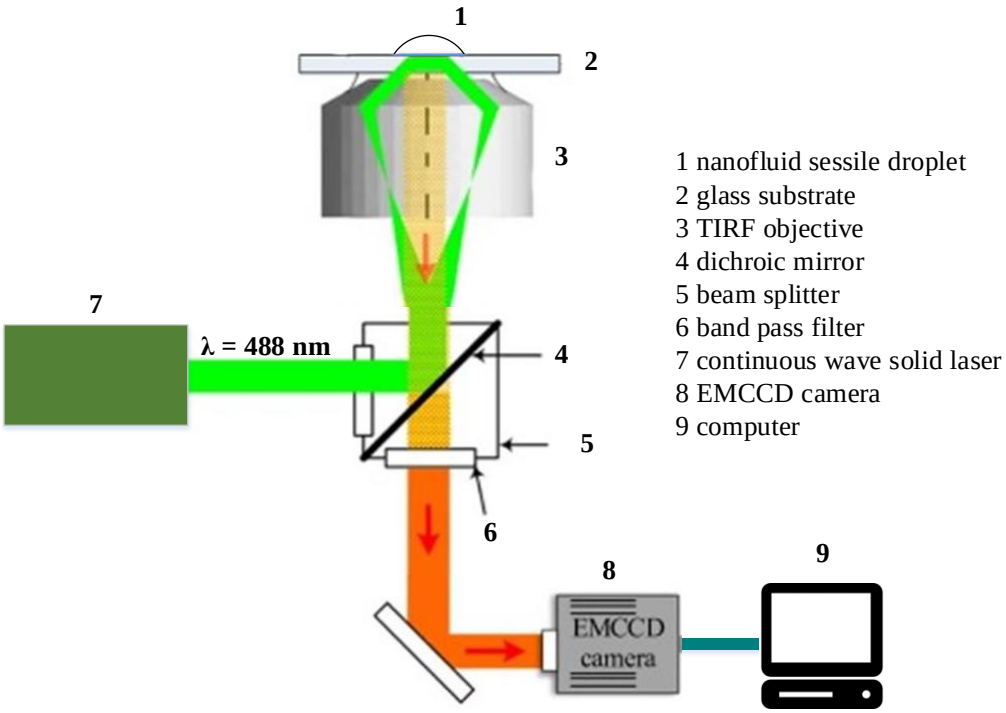

Figure 4. 2 Schematic of the TIRFM (total internal reflection fluorescence microscopy) setup

Figure 4. 3 A photograph of the inverted microscope

A schematic of the experimental procedure for flow analysis is also shown in **Fig. 4.4**. In one measurement, the EMCCD recorded a series 100 images with 50 sets of in-plane intensity data which were averaged to minimize the chance of random error.

The tracer particle position with respect to the wall and thus the movement of the tracer particles in the liquid film close to the three phase line can be quantified by processing the images using standard algorithm of particle velocimetry. The technique and its accuracy had already been validated by various researchers [49, 62, 143, 144] using different methods including micro scale Poiseuille flow, near wall flow, nanoscale near wall contact line visualization and electro osmotic flow.

The evaporation of the nanofluid droplet containing Si/Ag nanoparticles and fluorescent tracer particles was carried out on a pendant drop setup under different irradiance levels as schematically shown in **Fig. 4.5**. The droplet drying process was imaged with a high speed CCD camera at the rate of 25 frames per second. The

spatial resolution of the imaging system was about 3 μm per pixel. The distance between the imaging system and the droplet was kept constant to have comparable results. A micro syringe pump was used to drip the droplet on the glass substrate. The droplet was evaporated three times under each radiation condition to confirm the consistency in the drying time recording. Images were taken from the time of dripping the droplet onto the glass substrate till it vanished completely.

A self-developed MATLAB code was used to process all the images which counts the number of pixels in the droplet zone. The pixels could be converted to droplet nominal diameter, droplet height and volume at different time intervals during the evaporation by scaling the pixels to an object of known size. The deposition patterns of the dried droplet in each case were recorded on TIRFM setup using laser light and 10x magnification objective with EMCCD.

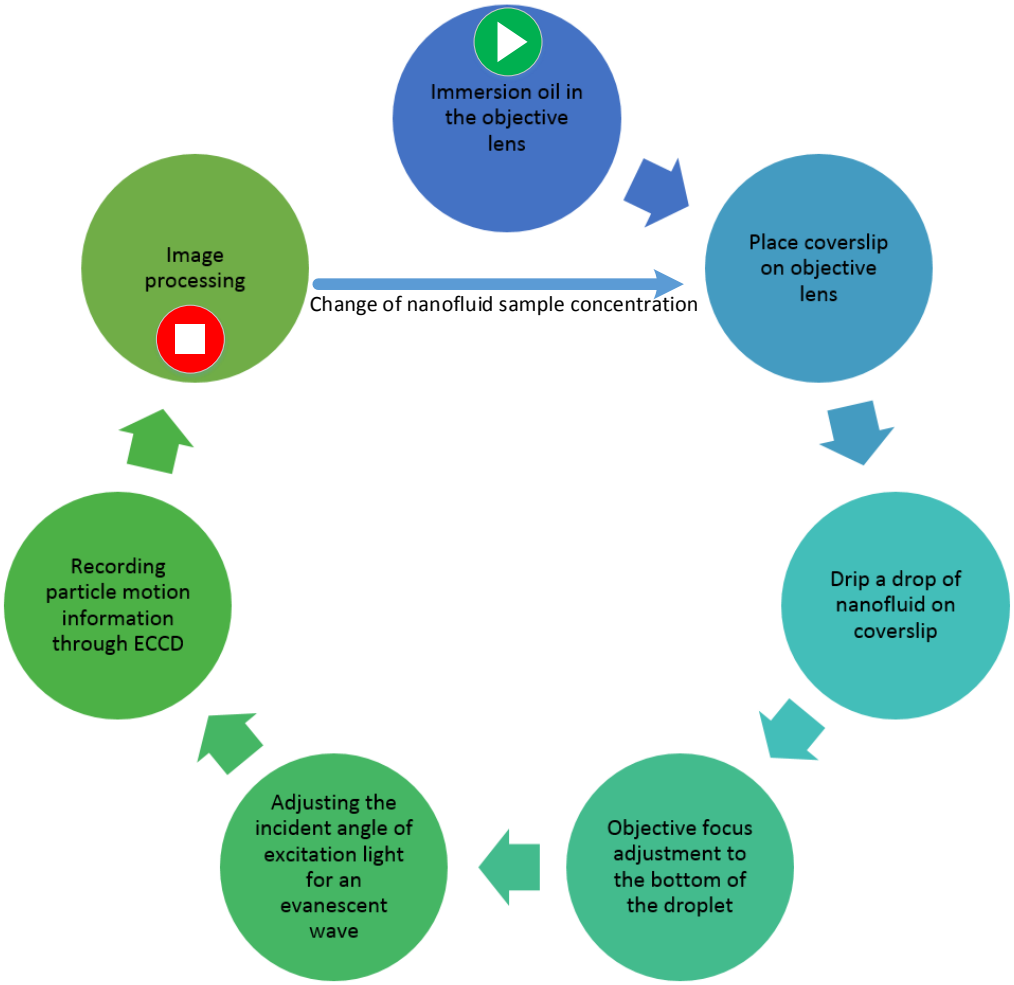

Figure 4. 4 Steps involved in nanofluid droplet drying process

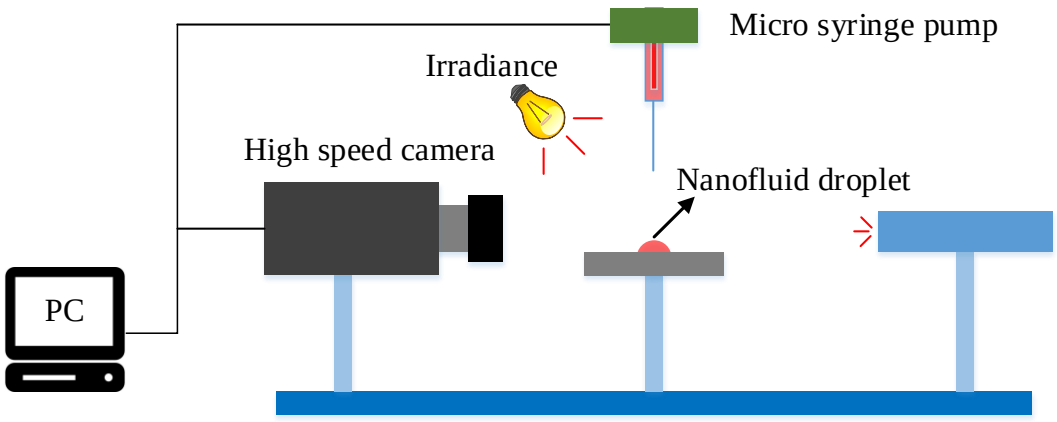

Figure 4. 5 A schematic of the nanofluid droplet drying setup

4.3 Results and analysis

4.3.1 Optical absorbance

Water is a poor absorber of the solar energy in the visible light spectrum where most of the solar energy is contained as can be seen from **Fig. 4.6.** Solar absorption of water can be significantly enhanced by adding nanoparticles that have good absorptivity in the visible region. In this study, the optical absorptivity of the prepared nanofluids was checked by a UV-Vis spectrometer using a high precision quartz cell with light path of 10 mm. The optical absorbance spectra and spectral solar irradiance are shown in **Fig. 4.6**.

The absorbance is defined as the logarithm (10 as base) of reciprocal of transmittance whereas the transmittance is the ratio of the transmitted light by the nanofluid sample to the incident light. According to the Beer-Lambert's Law [145], absorbance is $log(I_o/I) = \epsilon lc$, where I_o is the incident light on the sample, I is the light transmitted, ϵ is the extinction coefficient, l is the length of the sample through which light passed, and c is the concentration of the nanofluid.

Different metallic nanofluids have different optical absorption peaks over the visible spectrum. The absorption peak of silver nanoparticles is the strongest amongst all the nanofluids compared at the same particle concentration of 0.01 wt. % (Fig. 4.6).

This is due to the strong localized surface plasmonic effect in silver nanoparticle that makes it different from the others. The plasmonic resonance frequency of silver nanofluid can be seen around 430 nm from Fig. 4.6, which is almost the beginning of the visible band of the solar spectrum.

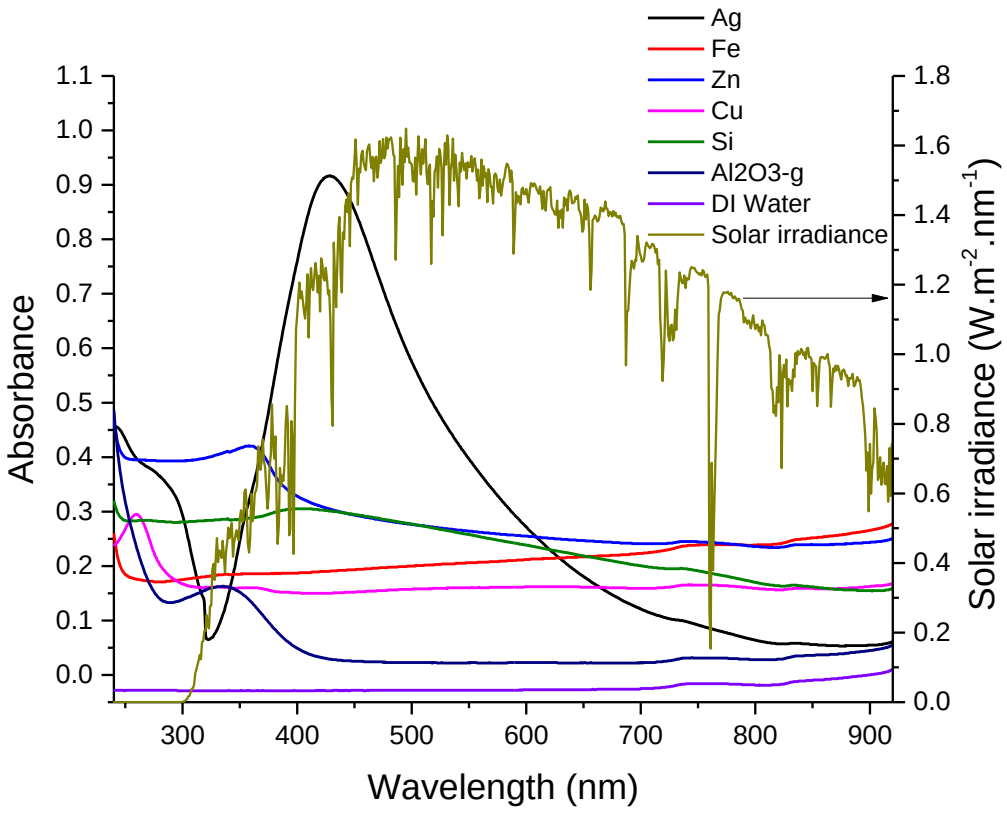

Figure 4. 6 Optical absorbance spectra of DI water based nanofluids (0.01 wt%)

Compared with silver, the optical absorbance of other nanofluids in this study has mostly their absorption peaks in the UV to visible region. Though the absorption peaks of Fe, Si, Cu nanofluids are not very strong in the UV region, the flat absorption curve in the visible region shows that their absorption is far much better than water at such a low weight concentration.

4.3.2 Volumetric heating of nanofluid samples

The temperature of the nanoparticles in the nanofluid can be assumed as the temperature of the bulk fluid due to very small nanoparticle concentration i.e. only 0.01% by weight. Deionized water and sample of each fluid was heated for a minimum period of 30 min under the solar flux of 12 suns. **Fig.4.7 (a)** represents the

temperature variation of three thermocouples for a silver nanofluid sample, and **Fig.4.7 (b)** shows the average temperature profiles of various nanofluid samples under consideration.

As it can be clearly seen from **Fig.4.7 (a)** that all three thermocouples show almost linear increase in bulk fluid temperature at the start of the experiment, and this linearity is lost as the experiment is continued. Such a linearity at the start of the experiment is because almost all of the energy is absorbed by the nanofluid and there is negligible heat leak to the surroundings. But as the temperature of the nanofluid increases, the temperature difference between the sample and the surrounding increases, which results in increased heat loss that deviation from the linearity. As the temperature difference goes to the maximum value within the experimental settings, further increase in temperature is small, as can be seen at the later stage of the experiment in **Fig.4.7**.

The rate of temperature rise for TC1 is higher than that of other two thermocouples i.e. TC2 and TC3 because most of the solar energy is absorbed by the top surface of the nanofluid and lower rate of temperature rise under the top surface is due to the decay in the solar intensity along the optical length. The maximum temperature difference between TC1 and TC3 reached about 5 ^{o}C, indicating a large temperature non-uniformity inside the fluid. The room temperature remained almost the same during the experimental run as can be seen in **Fig.4.7 (a)**.

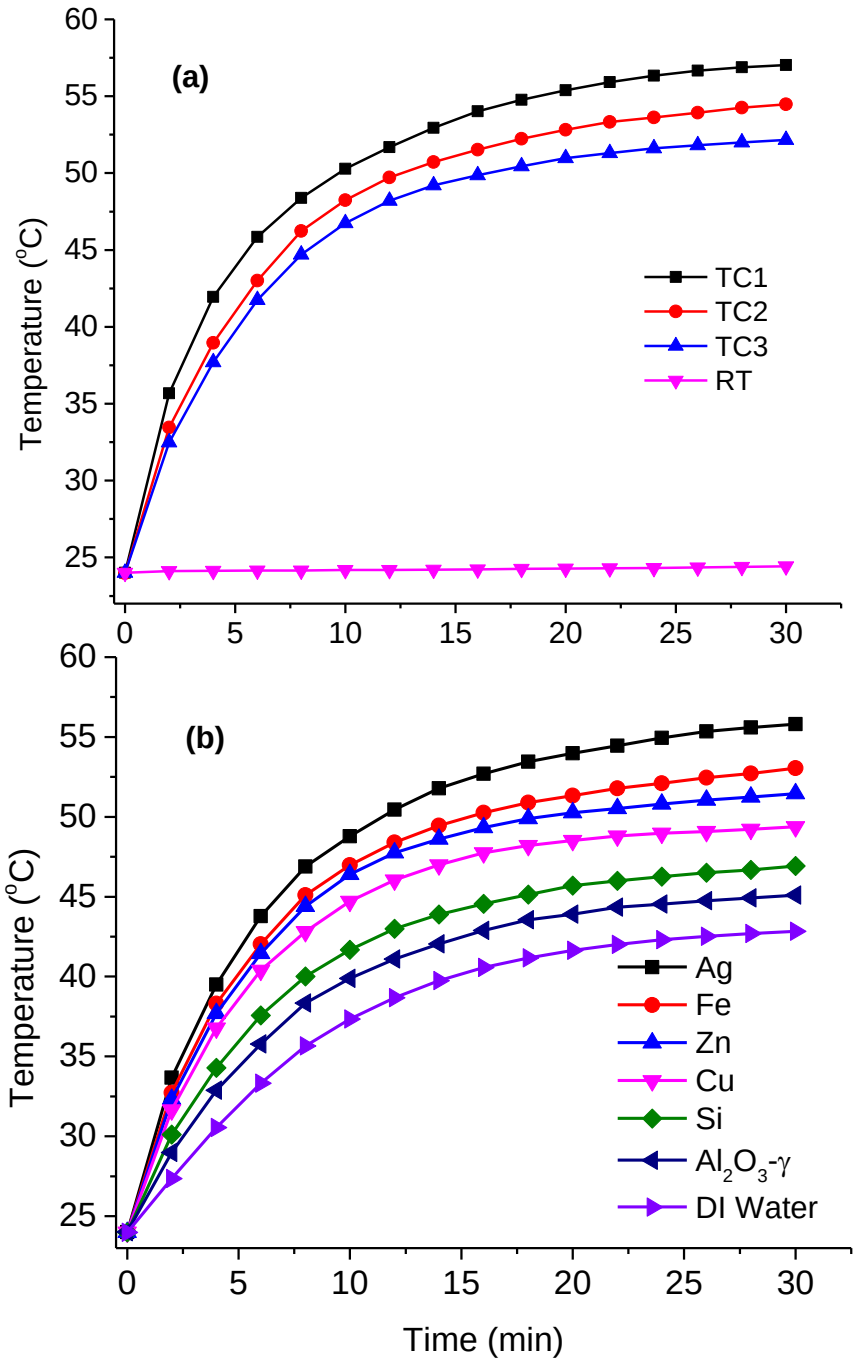

Figure 4. 7 (a) Temperature distribution in silver nanofluid where RT is room temperature, (b) Average transient temperature profiles of various nanofluid samples with 0.01% weight concentration under a solar intensity of 12 Suns and comparison to that of deionized water.

The average temperature of the three thermocouple values ($\Delta T = (T_1 + T_2 + T_3)/3$, where T_1, T_2 and T_3 are temperatures measured by thermocouples TC1, TC2 and TC3 respectively) is plotted against time for all the nanofluids under consideration in **Fig. 4.7 (b)** at the same concentration of 0.01% by weight. In comparison with deionized water, all of the nanofluids have higher temperature gradients except Al_2O_3-γ, which is only slightly higher. In the order of the nanofluids with respect to their peak temperature, silver nanofluid is at the highest position, followed by Fe, Zn, Cu and Si.

The mass loss of the sample due to vaporization was measured by an electronic scale over a 30 min time period, and is given in **Fig. 4.8**. The mass loss of the sample of DI water and nanofluid is proportional to the fluid bulk temperature rise shown in **Fig. 4.7**. Under the effect of a low solar flux from the solar simulator, most of the energy was consumed in heating the bulk fluid at the initial stage of the experiment, as can be seen by the contribution of sensible heat and latent heat in **Fig. 4.9** for the case of silver nanofluid. But as the experiment proceeds, more absorbed energy is used to evaporate the fluid, instead of heating the bulk fluid. The heat loss to the ambient increases with the increase in overall temperature of the sample volume.

4.3.3 Photothermal efficiency

As the overall temperature of the nanofluid sample is small, it can be assumed that temperature of the nanoparticles and the surrounding fluid is same. For smaller fluid depths and overall homogeneous temperature distribution in a fluid volume, the light to heat conversion transient efficiency η_{PTE} can be calculated by the relation in Eq. (4.1);

$$\eta_{PTE} = \frac{\int_0^t (c_w m_w + c_n m_n).\Delta T.dt + \int_0^t L_v.m_{loss}.dt}{\int_0^t I.A_i.dt} \quad (4.1)$$

where c and m represent the specific heat capacity (J/kgK) and mass (kg) and the subscripts w and n represent water and nanofluid respectively, ΔT is the average ($(\Delta T = (T_1 + T_2 + T_3)/3)$) change in temperature of three thermocouples in time t, I is the solar irradiance, which is equal to 11.6 kW/m^2 in this work and A_i is the illumination area of the nanofluid sample, L_v is the latent heat of vaporization of water at 1atm and m_{loss} is mass loss of the sample in time t.

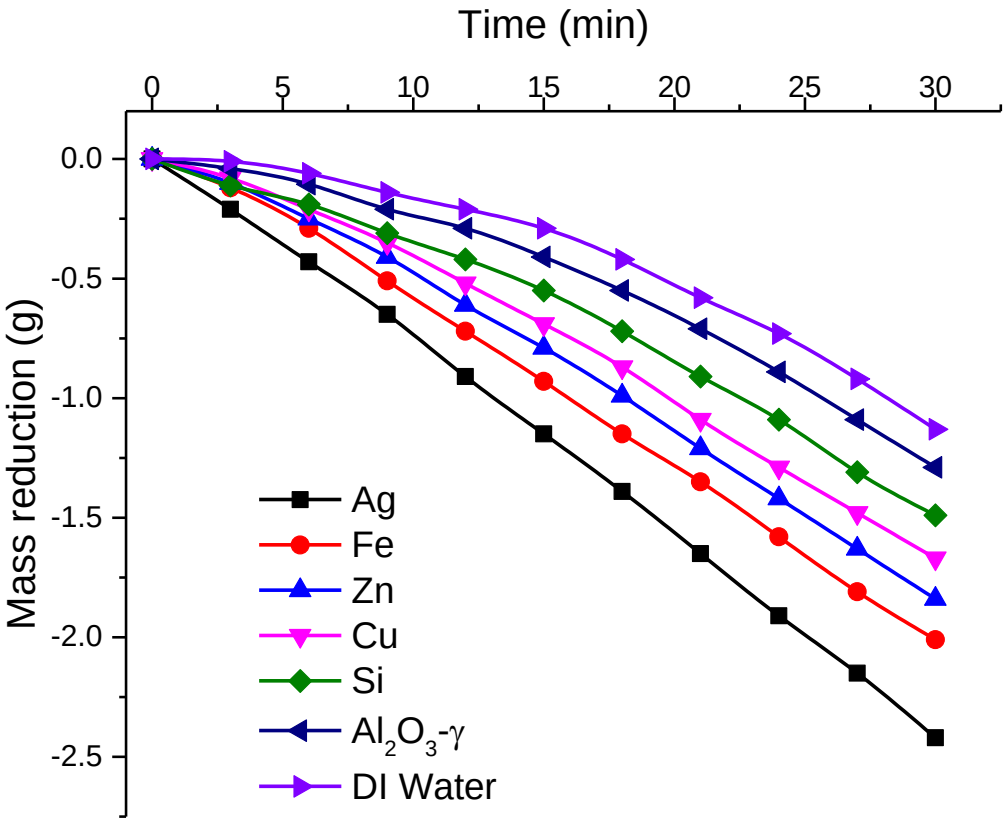

Figure 4. 8 Mass loss over a period of 30 min for various nanofluids under a solar intensity of 12 Suns.

As the overall particle concentration is very small so the $c_n m_n / c_w m_w \approx 0$, and the Eq. (4.1) can be modified to Eq. (4.2);

$$\eta_{PTE} = \frac{\int_0^t c_w m_w . \Delta T . dt + \int_0^t L_v . m_{loss} . dt}{\int_0^t I . A_i . dt} \quad (4.2)$$

Light to heat conversion efficiency including sensible heating and vapour generation efficiencies of various nano suspensions with 0.01 wt.% concentration for initial stage of heating for 6 min is shown in **Fig. 4.10 (a)** and for total experiment duration in **Fig. 4.10 (b)**. Comparing with the base fluid, the photothermal conversion efficiencies of nanofluids are significantly higher. The average fluid temperature from three thermocouples was used. Amongst all the nanofluids used in this study, Ag has the highest efficiency as compared to the base fluid. The enhancement in efficiency over the experimental domain is shown in **Fig. 4.11**, while the inset shows the efficiency enhancement in the first 6 min duration over the base fluid.

The heat utilization and its distribution to sensible heat, latent heat and ambient loss for the case of silver nanofluid is shown in **Fig. 4.9**. The sensible heat and latent heat of vaporization of the silver nanosuspension as shown in **Fig. 4.9 (a)** are almost equal at the very beginning of the experiment while the latent heat of vaporization part of the utilized energy keeps on increasing over the sensible heat part with time. This increasing trend of latent heat continues until the end of the experiment while the increase rate of sensible heat of the sample is very low especially at the last phase of the experiment. The corresponding efficiency of the sensible heating and vapour generation are shown **Fig 4.9 (b)**, which shows a gradual decrease in overall photothermal performance of the silver suspension over the time.

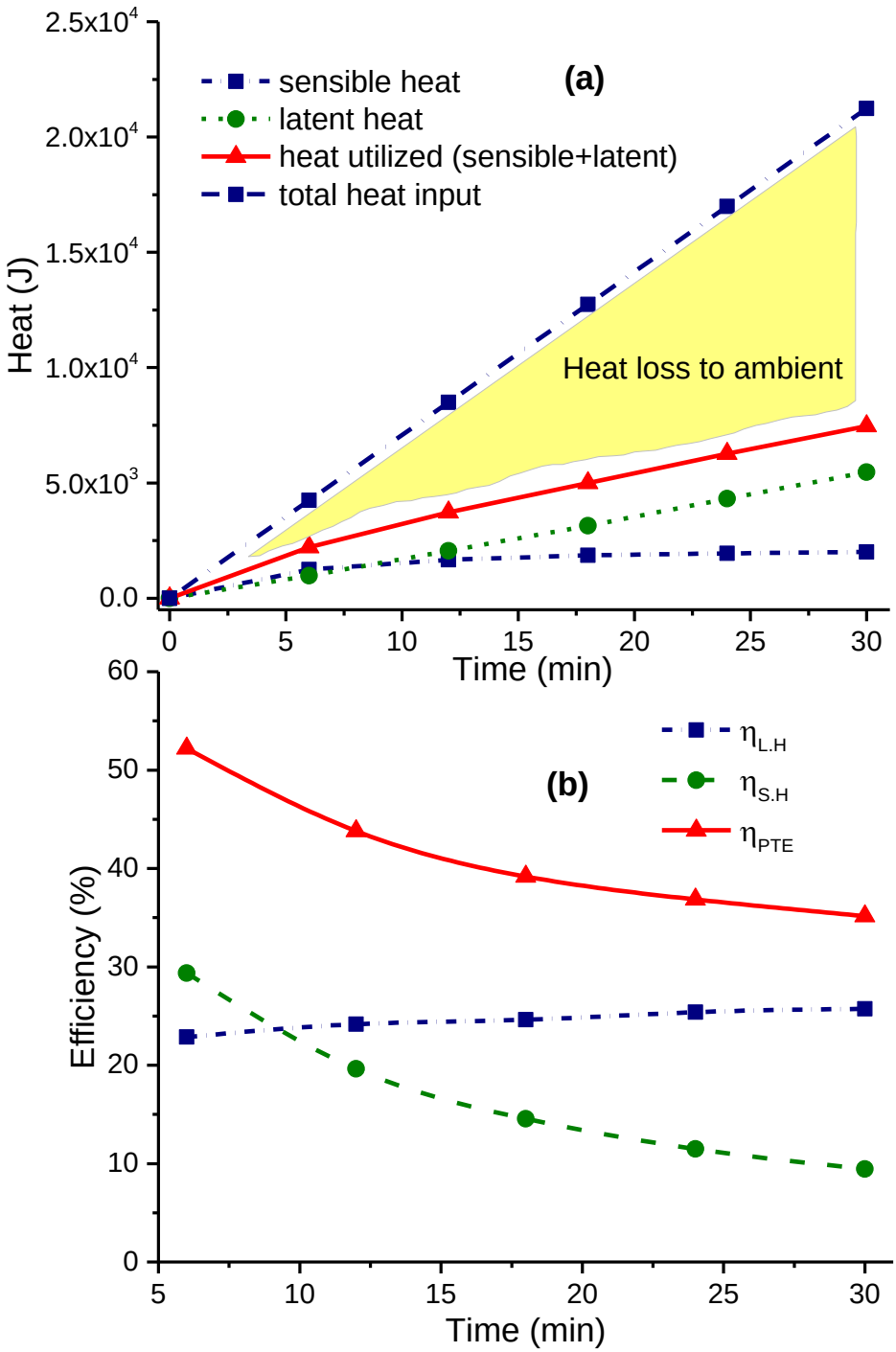

Figure 4. 9 Photothermal performance of silver nanofluid over a period of 30 minutes , (a) contribution of sensible heating and latent heating, and (b) variation of sensible heating and latent heating efficiencies ($\eta_{S.H}$ and $\eta_{L.H}$ respectively) and overall photothermal efficiency (η_{PTE}).

A comparison of heating efficiency and vapour generation efficiency of various nanofluids investigated based on initial phase (6 min) and over the domain of the experiment (30 min) is presented in **Fig 4.10**. The ascending order of different nanofluids in terms of their overall experimental photothermal performance is Al_2O_3-γ, Si, Cu, Zn, Fe and Ag based on 6 min and 30 min data shown in **Fig. 4.10 (a)** and **Fig. 4.10 (b)** respectively. It can be concluded from **Fig. 4.10 (b)** that the efficiency of sensible heating for all the nanofluids is almost the same with little variation over 30 min duration of exposure to solar flux and the major difference in between lies on the evaporation effect. As revealed from Jin et al. [146, 147], there was large temperature difference inside nanofluids under solar radiation, and the major effect for nanofluids lies on the trapping of solar energy, especially at the surface layer. Under strong solar radiation (i.e. a few hundred of Suns), the surface layer could become superheated and vigorous boiling could occur, albeit the bulk fluid is still under subcooled condition. The current study revealed a similar trend. Although the temperature was not high enough to cause vigorous boiling, the major difference among different nanofluids lies on the surface trapping and evaporation effect. The difference in heating the bulk fluids, as shown by the sensible heating efficiency, is small among different nanofluids. Most of the extra heat converted by nanoparticles is used to evaporate the fluid, which mainly occurs at the surface. The higher the surface temperature, the higher the evaporation rate.

After 6 min of the experiment, the efficiency of the sensible heating and that of vapour generation are 29.4% and 22.8% respectively, which are 9.4% and 25.7% after 30 min.

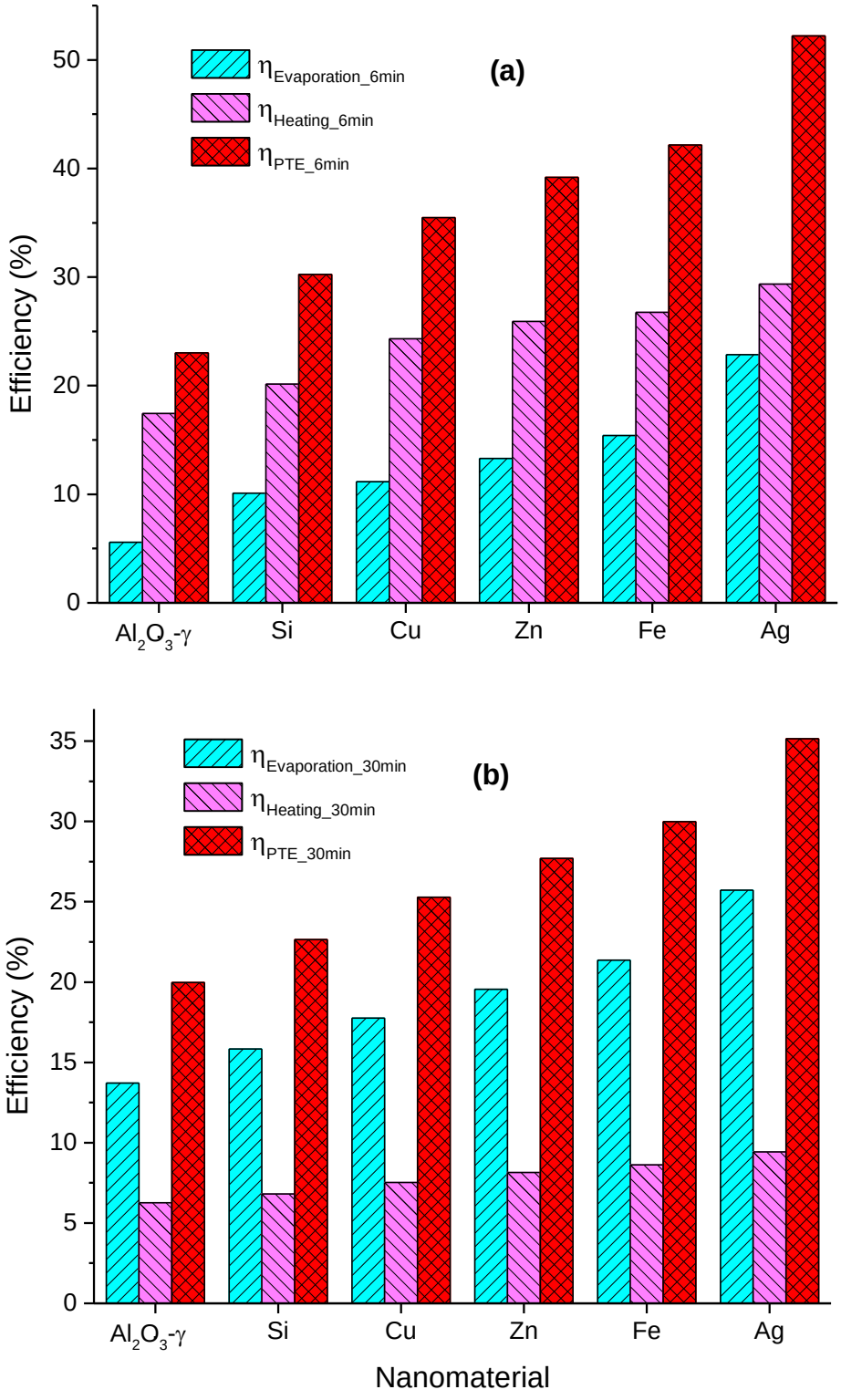

Figure 4. 10 Distribution of Photothermal conversion efficiency of various nanofluids into sensible heat efficiency and evaporation efficiency based on the data of (a) first 6 min and (b) 30 min

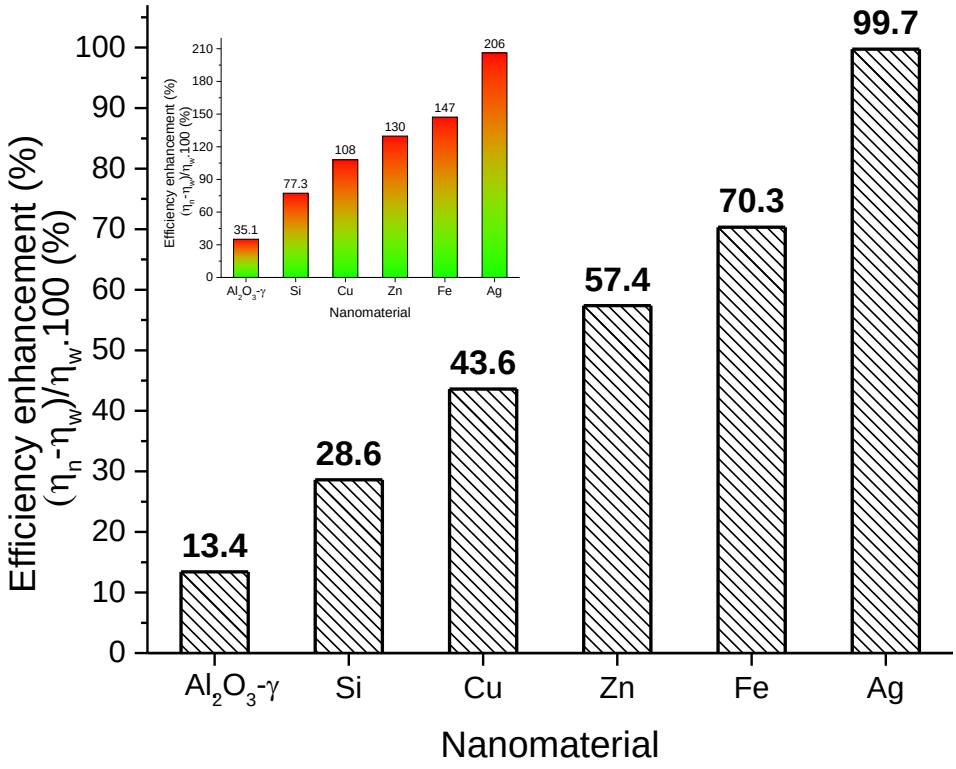

Figure 4. 11 Overall enhancement in photothermal conversion efficiency over the base fluid for full experimental duration (i.e. 30 min). The enhancement for first 6 min of the experiment is even higher, which is also shown as the inset.

A dramatic change in the heating efficiency over time shows a rapid loss of heat to the ambient while a slight variation in the vapour generation efficiency signifies that the strong localized heat by silver nanoparticles sustained vapour generation irrespective of the bulk fluid temperature within the experimental domain.

4.3.4 Specific absorption rate

Other than photothermal efficiency, specific absorption rate (SAR) is an important quantitative tool to evaluate the ability of the nanoparticles to absorb energy. The energy absorbed per unit mass of the nanoparticles is known as SAR, used to describe the photothermal performance of nanofluids. The ability of plasmonic

nanoparticles to absorb solar energy is much better than that of many magnetic nanoparticles under such a low light heat flux as described by [148]

SAR (kW/g) of nanofluids can be calculated using Eq. (4.3)

$$SAR = \frac{[(c_w m_w + c_n m_n)\Delta T_n - c_w m_w \Delta T_w] + L_v . m_{loss}}{1000\, m_n \Delta t} \quad (4.3)$$

where c_w and m_w represent the specific heat capacity (J/kgK) and mass (kg) of base fluid and c_n and m_n represent specific heat capacity and mass of nanoparticles. ΔT_n and ΔT_w show the change in temperature of nanofluid and water in time Δt respectively. Within the scope of this work $((c_n \Delta T_n / (1000. \Delta t)) \sim 0$ and hence the SAR can be approximated as in Eq. (4.4)

$$SAR \approx \frac{c_w m_w (\Delta T_n - \Delta T_w) + L_v m_{loss}}{1000. m_n \Delta t} \quad (4.4)$$

Fig. 4.12 shows the SAR of the nanofluids compared with the base fluid for a 0.01% concentration by weight. Clearly from **Fig. 4.12**, the SAR of silver nanoparticles is higher than any other nanoparticles due its plasmonic nature and the results are consistent with that of Bandarra et al. [22]. However, the silver nanofluid was not stable at high temperature and also due its sticky nature, it could not be used in a closed loop process. Hence nanofluids of gold and carbon nanofibers are experimented for solar steam generation and are presented in chapter 5 and 6 respectively.

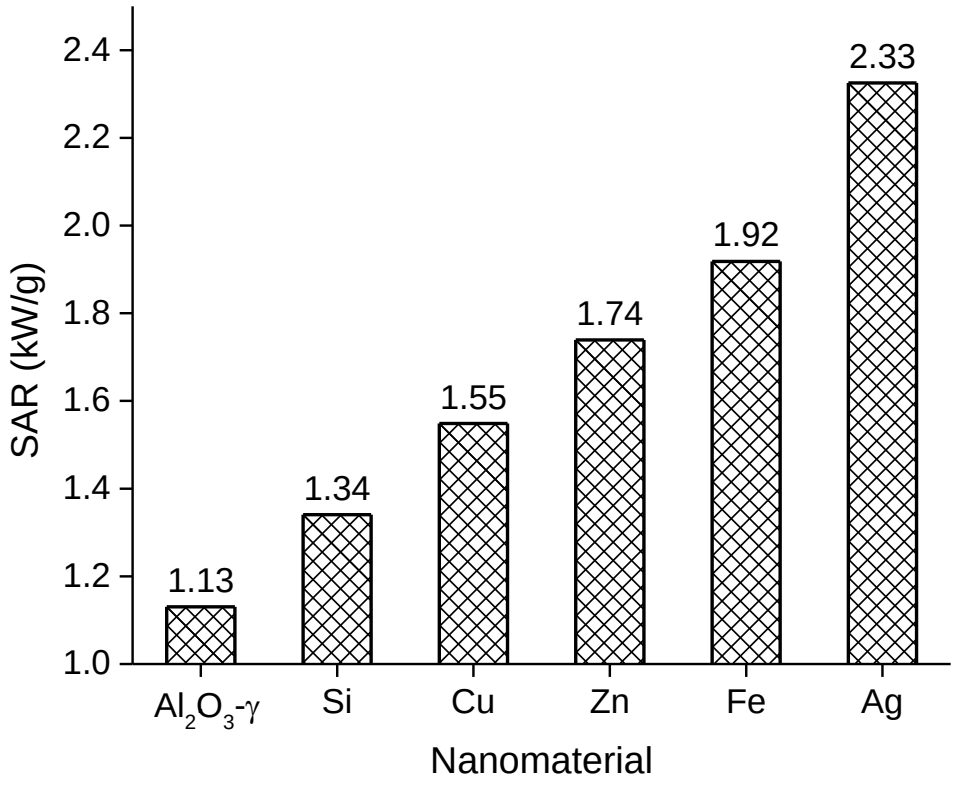

Figure 4. 12 Specific absorption rate of nanofluids over the period of 30min.

4.3.5 Droplet evaporation and deposition patterns

The hybrids of the tracer particle solution as base fluid and Si/Ag nanofluid were made by mixing the known concentration of each and presented in **Table 4.1** in which B and H stand for base fluid and hybrid fluid respectively. The evaporation profiles of the droplets for various concentrations of the fluorescent particles and core/shell Si/Ag nanoparticles under varying irradiance levels are given in **Fig. 4.14** and **Fig. 4.15**.

There was a slight variation in the initial droplet volume in each experiment, normalized volume (V_n) during the droplet evaporation time are compared which can be calculated from Eq. (4.5% as given below;

$$V_n = \frac{V_t}{V_0} \tag{4.5}$$

Here V_t is the droplet volume at any time t during the evaporation and V_0 is the initial droplet volume. As the normalized volume is a ratio of the volumes, it does not have any unit. **Figure 4.13** shows the evaporation of the droplet containing tracer particles only (B1 and B2) and act as a baseline for the hybrid droplet evaporation. **Figure 4.13 (a)** shows that the tracer particles have negligible influence on the evaporation of the droplet. As the tracer particles are the fluorescent particles only (i.e. with very weak light absorptivity), the change in the intensity of light as a heat source has almost no influence on the droplet evaporation behaviour. **Figure 4.13 (b)** shows that evaporation curves for the three irradiance levels almost overlap each other at the initial stage of the evaporation. The final stage of the droplet evaporation experiences a very negligible effect of incoming light intensity. It can be assumed that any significant change in the evaporation behaviour of the droplet is due to the core/shell Si/Ag nanoparticles.

Table 4. 2 Concentration of tracer particles and Si/Ag nanoparticles in the hybrids and their initial average contact angle measurements

Hybrid no.	Tracer particle concentration (% w/v)	Nanoparticle concentration (%wt)	Initial contact angle (degree)
B1	0.00025	----	30.4
B2	0.00050	----	31.7
H1	0.00025	0.003	28.8
H2	0.00050	0.003	27.6
H3	0.00025	0.006	29.5
H4	0.00050	0.006	29.8

$$V_n = \frac{V_t}{V_0}$$

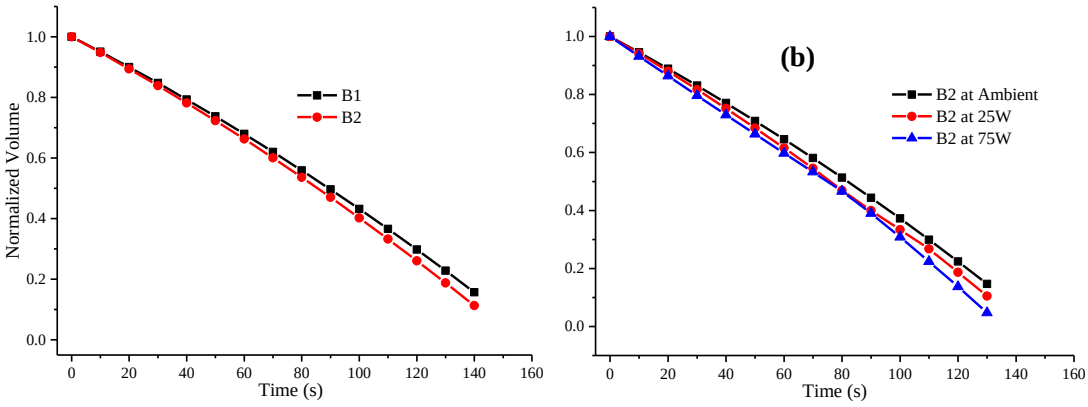

Figure 4. 13 Normalized evaporated volume as a function of time; (a) effect of concentration of the tracer particles on the evaporated volume and (b) the effect of irradiance on the evaporation of droplet from base fluid B2

The normalized evaporated volume over the evaporation time for the droplet from hybrid H1 under the varied incoming heat fluxes is given in **Fig. 4.14**. The presence of Si/Ag core/shell nanoparticles in the droplet changed the evaporation time of the droplet dramatically under different irradiance levels. The light absorbing Si/Ag nanoparticles decreased the evaporation time of the droplet as the intensity of the incoming light is increased thereby increasing the evaporation rate as shown in the inset of **Fig. 4.14**. The evaporation rate is increased from 5.8 µL/s to 10.6 µL/s as the irradiance is increased from ambient to 75 W for the same amount of tracer

particles and nanoparticles. This increase in the droplet evaporation rate can be associated with the localized heating around the highly absorbing nanoparticles.

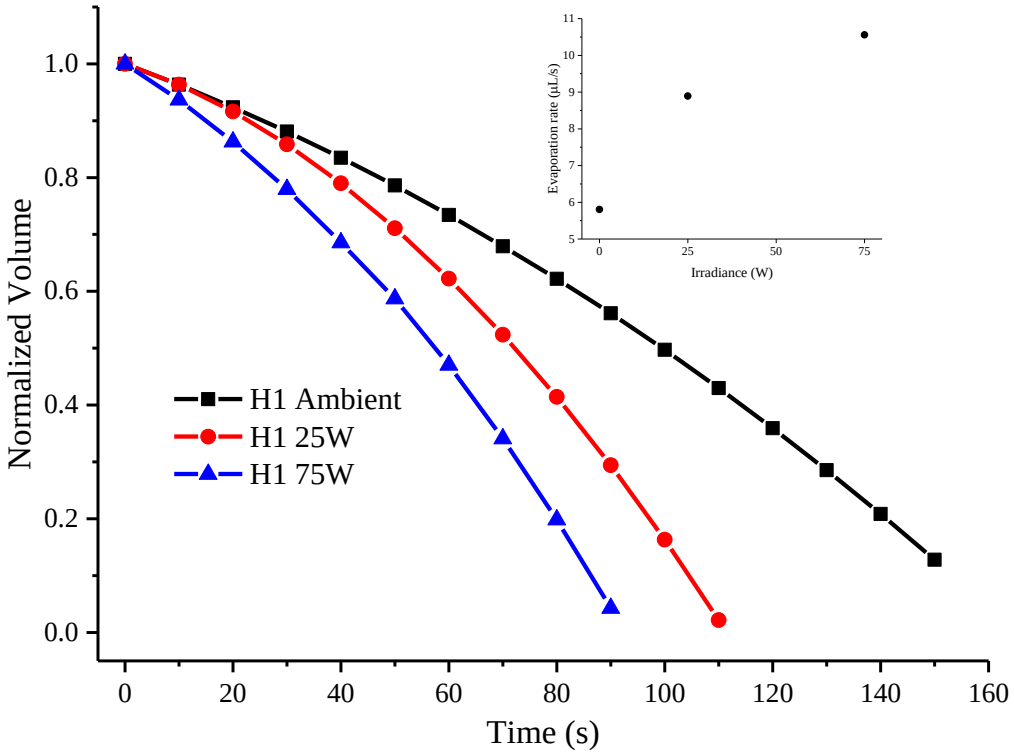

Figure 4. 14 Evaporation of the droplet containing hybrid H1 under different irradiance levels. The inset shows a relation between the droplet evaporation rate and irradiance

Figure 4.15 (a) shows the influence of Si/Ag nanoparticle concentration in hybrids H1 and H3 compared with B1 at 75 W irradiance while the effect of core/shell nanoparticles in hybrids H2 and H4 compared with their respective base fluid B2 under 25 W is presented in **Fig. 4.15 (b)**. The droplet evaporation rate is increased from 9 µL/s to 14 µL/s with the addition of only 0.006 w% Si/Ag nanoparticles, i.e., an enhancement of 55.5% over the base fluid.

The evaporation of the sessile droplet may follow the constant contact radius (CCR) mode or the constant contact angle (CCA) mode or combination of them. In CCR

mode, the contact line of the droplet is pinned to the substrate and the contact angle keeps on decreasing while the contact angle remains fixed and the droplet contact area keeps decreasing during the evaporation in CCA mode [149]. The evaporation of the droplets in the current study followed the CCR mode during the initial evaporation phase while the CCA mode was followed at the dry out phase of the droplet, which is consisted with the observation from a few other researchers [55, 150-152]. The transition of the contact line of the droplet from 'pinning' to 'depinning' is an important dimension for the analysis of the droplet evaporation and disposition pattern. The duration of the pinning which is the time before the contact of the droplet starts receding can be affected by many factors including the size of the droplet, the size and concentration of the nanoparticles in the droplet, the nature of the nanoparticle materials, the substrate and the intensity of thermal influx or irradiance.

The fluid flow dynamics and the effect of nanoparticle addition on the three phase contact line pinning during the droplet evaporation can also be observed from the deposition patterns. The particles in the droplets having different particle concentrations and evaporated under varied irradiance levels exhibited different deposition patterns as can be seen in **Fig. 4.16** and **Fig. 4.17**.

Similar to the non-irradiation case, a non-uniform evaporation caused by the capillary flow takes most of the particles in the droplet to the contact line and deposited there. Consequently a bright ring is developed as shown in Fig. 4.16. It can be stated that the very first pinning-depinning-pinning cycle of the droplet contact line during almost half of the droplet evaporation time is wider for the lower particle concentrations than that of higher concentrations of the tracers as well as

Si/Ag nanoparticles. Then the recurring process of pinning and depinning of the droplet contact line which is also known as ‘stick-slip behaviour’ starts till the complete evaporation of the droplet thereby giving a multi-ring like pattern of the dried droplet.

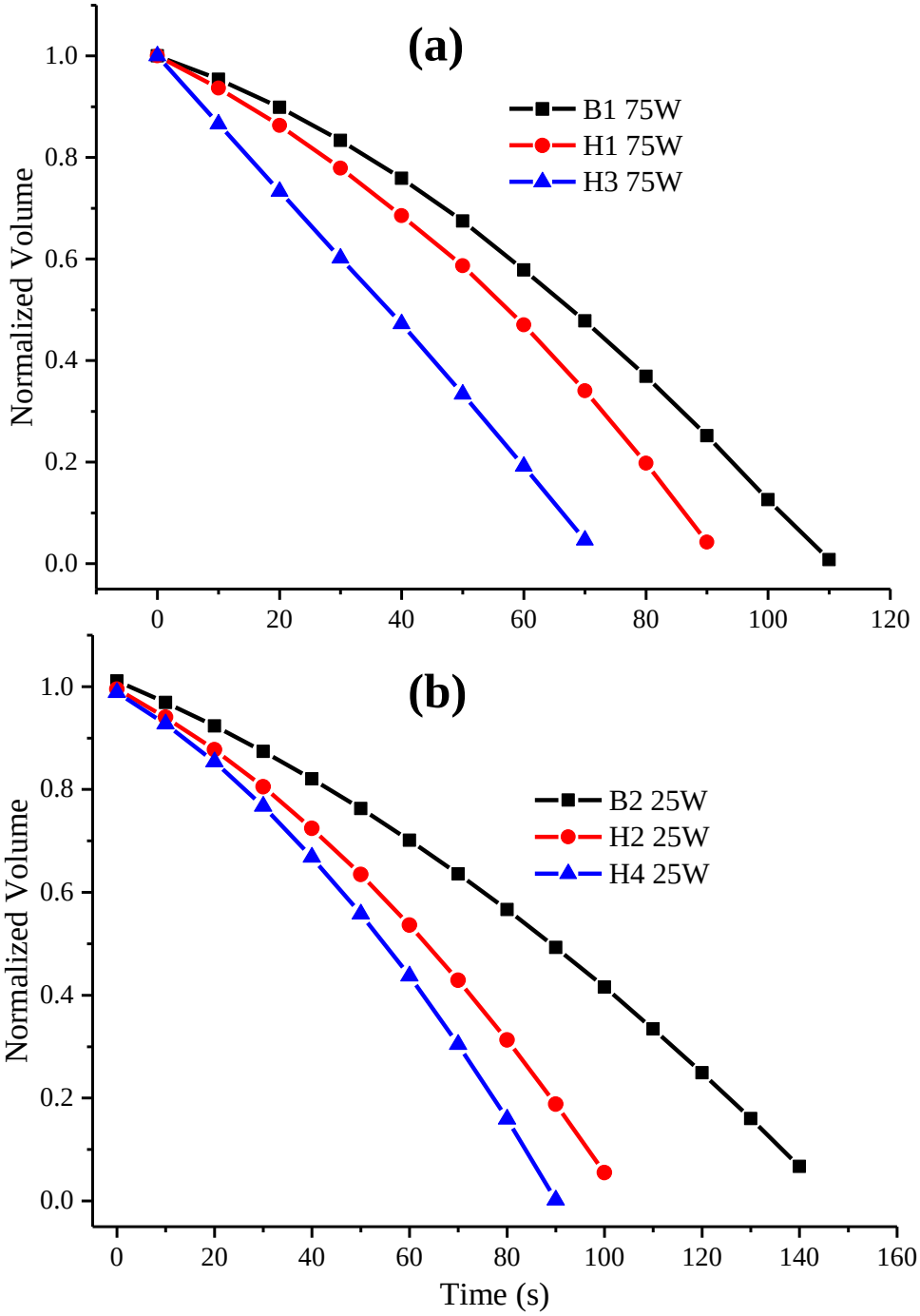

Figure 4. 15 Droplet evaporation having different concentrations of Si/Ag nanoparticles in hybrid with tracer particles concentration of (a) 0.00025 w/v% (B1) at 75 W irradiance and (b) 0.00050 w/v% (B2) at 25 W irradiance

In some cases, the contact line is pinned and the residual fluid at the centre of the droplet is moved to the pinned edge under thermocapillary flow at the final

evaporation stage of the droplet, leaving a relatively empty space at the centre of the droplet as shown in **Fig 4.16 (c)** and **Fig. 4.17 (b and c)**. The recurring rate of stick-slip of the contact line of droplet having higher particle loading and under the higher thermal intensity is so fast that the overlapping or in some cases very tightly packed asymmetric rings pattern is developed during the droplet evaporation as can be seen in **Fig. 17**.

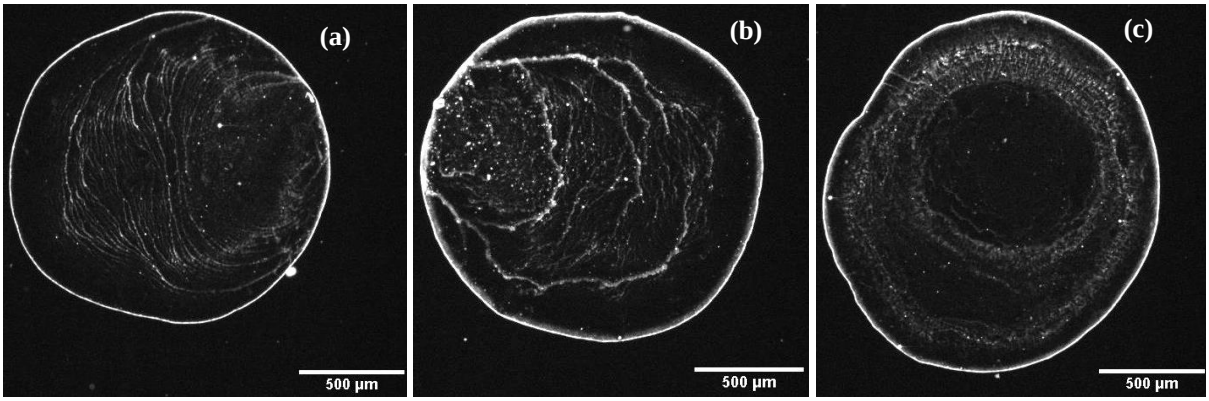

Figure 4. 16 Deposition patterns of the droplet of (a) B1, (b) H1 and (c) H3 evaporated at 25 W irradiance

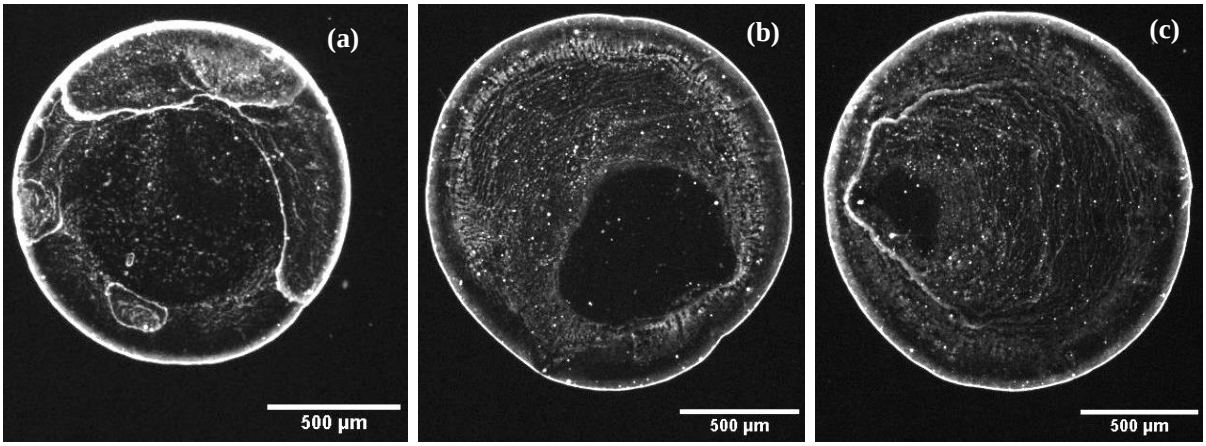

Figure 4. 17 Deposition patterns of the droplet of (a) B2, (b) H2 and (c) H4 evaporated at 75 W irradiance

The evaporation rate and deposition patterns of the droplet are significantly influenced by the concentration of the Si/Ag core/shell nanoparticles and radiation intensity. The concentration of the nanoparticles greatly enhanced the droplet evaporation rate due to the higher absorptivity of Si/Ag nanoparticle, which also influence the deposition patterns. However the mechanism of asymmetrically deposited particles duration the evaporation of the droplets containing tracer particle and Si/Ag nanoparticle hybrids is a complex phenomenon.

4.4 Chapter summary

Direct solar absorption based performance of different nanofluids was checked under a simulated solar flux up to 12 suns in bulk nanofluid volume as well as under a very week radiation flux on a micro droplet level. Six most commonly used nanomaterials were identified and investigated for their direct volumetric solar absorption performance in bulk fluid volume. It was found quantitatively that the addition of small fraction of nanoparticle in the base fluid can significantly enhance its photothermal conversion performance, not only at micro droplet level but also on bulk fluid scale. Comparing with the base fluid, the silver nanofluid enhanced the photothermal efficiency by 99.7% followed by iron nanofluid which gave an enhancement of 70.3% over the base fluid at bulk fluid scale. On the other hand, silicon/silver hybrid nanofluid was investigated for direct radiation absorption in a micro droplet having fluorescent tracer particles. The tracers were used to visualize the flow dynamics and the consequent deposition patterns using a unique experimental setup based on total internal reflection (TIR) principle. A detailed experimental insight into the effect of Si/Ag nanoparticles in an evaporating

nanofluid micro droplet and their influence on the consequential deposition pattern was conducted. Only 0.006 wt% concentration of Si/Ag nanoparticles resulted in an enhancement of about 55.5% in the droplet evaporation rate. The results of the direct solar absorption by nanofluids on a bulk fluid volume as well as at micro droplet level proved that the addition of even a very small concentration of nanoparticles in the base fluid can significantly enhance its photothermal performance.

Chapter 5

Solar Steam Generation and its Characterization

This chapter deals with the solar steam generation capability of nanofluid under a concentrated simulated solar flux. An integrating method of calculating the sensible heat along the optical depth of nanofluid sample is proposed. It also gives the analysis of product water in relation to the presence of nanoparticles and characterization of nanofluid after the steam generation experiments.

5.1 Introduction

In addition to the volumetric heating and micro droplet evaporation based on nanofluids, direct vapour generation due to localized heating of nanoparticles [147, 153-155] is a recent development in this area. For example, Neumann et al. [156] showed that by using very dilute gold nanoparticles under a focused solar light via a typical Fresnel lens, steam was produced instantly while the measured bulk temperature was still 6 ^{o}C approximately. The calculated steam generation efficiency reached 80%, meaning only 20% of the solar radiation was used to increase the bulk fluid temperature.

Later simulation work [156-158] showed the possibility of nanobubble formation based on a non-equilibrium phase change assumption. However these results are quite different compared to the recent results from Jin et al. [159]. Still using a Fresnel lens (i.e. solar flux ~220 Suns), it revealed that steam generation was mainly caused by localized boiling and evaporation in superheated regimes due to a highly non-uniform temperature distribution, albeit the bulk fluid was still subcooled. They hypothesized that nanobubble, i.e., steam produced around heated particles, was unlikely to occur under normal solar radiations.

It shall be noted that all these experiments [146, 156, 159] were performed outdoor, where the solar flux varied from time to time, and the focus by Fresnel lens limited the heating to a small area, leading to a non-uniform solar energy input. This arrangement would lead to a very high solar flux in localized areas, producing spot heating and high evaporation rate locally.

As far as the steam generation mechanism is concerned, it has been shown analytically that a minimum radiation flux of 3×10^8 W/m^2 is required to produce nanobubbles on heated nanoparticles [158, 160, 161], which can only be reached by powerful laser beams. In a separated study, Julien et al. [162] showed that 1×10^{10} W/m^2 was required to generate a nanobubble on a plasmonic gold nanoparticle. However quite differently, Hogan et al. [163] reported that ~1 MW/m^2 solar flux was sufficient for efficient steam production due to a collective effect of nanoparticles that both scattered and absorbed light, hence localizing light energy into mesoscale volumes.

It can be noted that most of the experiments performed so far [146, 156, 159, 164] were not under well-controlled conditions. Besides the problem of varying solar flux and spot heating mentioned above, most of the experiments were performed by a single-point temperature measurement, ignoring the temperature distribution in the bulk fluid [21, 145, 156]. Though Jin et al. [147] and Ni et al. [155] used multipoint temperature measurement, only the average temperature was used for the evaluation of the photothermal efficiency. In Jin's work [147], the spot heating and small fluid volume minimized the temperature stratification phenomenon, and the fluid reached saturated boiling rapidly , where the most interesting phenomenon under subcooled condition was insufficiently captured.

Furthermore, the possible escaping phenomenon of nanoparticles with the steam under saturated boiling has not been investigated, which is critical for any potential desalination or clean water production applications. Clearly a better understanding of the solar steam generation by nanoparticles is much needed.

A novel one-dimension test section was designed, and multiple thermocouples were used to reveal the temperature distribution along the heating path under a highly concentrated solar flux of around 280 Suns. A novel integration method was proposed to calculate the sensible heating contribution and to aid the analysis of steam production mechanism.

The novel one-dimensional test section was used to investigate that whether the phenomenon of direct steam generation was the same or different under uniform heating rather spot heating and well controlled conditions. Furthermore, the underneath mechanism for direct steam generation was explained and the phenomenon of escaping nanoparticles with the produced steam was investigated by performing the steam generation experiments under concentrated solar flux.

5.2 Experimental setup

Steam generation capability of the characterized gold nanofluids were investigated using a solar simulator having seven xenon short-arc lamps aligned on the reflector ellipsoidal axis. The solar simulator is capable of producing a concentrated solar flux of about 4 MW/m^2 when all of seven lamps are in operation. The seven lamps are fixed in the form a hexagonal shape shown in **Fig. 5.1 (a)**.

The value of maximum flux at 25%, 50% and 75% of power capacity are 1.92, 3.16 and 3.91 MW/m^2 [165]. Only one lamp was put in operation for the current experiments to deliver a solar flux equivalent to 280 Suns (280 kW/ m^2). The flux was characterized by a manufacturer calibrated high radiative flux meter (Gardon type, Medthermo). There was a fluctuation in the radiation flux when the lamp was

started but the flux stabilized after 10 to 12 minute time as shown in **Fig. 5.1 (b)**. A door was used to block the radiation flux during the sample change over time instead of switching the lamp off.

The solar radiation had a focal area of 28.27 cm^2, which was passed through a custom-made aperture (30 mm diameter) of aerogel sheet wrapped in aluminium foil. The test section was made of high temperature quartz glass with the inner and outer diameter of 30 mm and 34 mm respectively. The test section was put accurately under the solar radiator to enable a uniform heating. A sample fluid of 25 ml (~35.4 mm depth) was filled into and covered with a transparent quartz cover. Holes of 1 mm diameter were fabricated in the vessel to insert the thermocouples equidistant to each other at 10 mm. The vessel was covered with a tightly packed aerogel blanket with thermal conductivity of 0.015 W/m^2K to minimize the heat loss to the surroundings. A square glass box was used to contain the aerogel with the vessel fitted in a hole in the aerogel sheets.

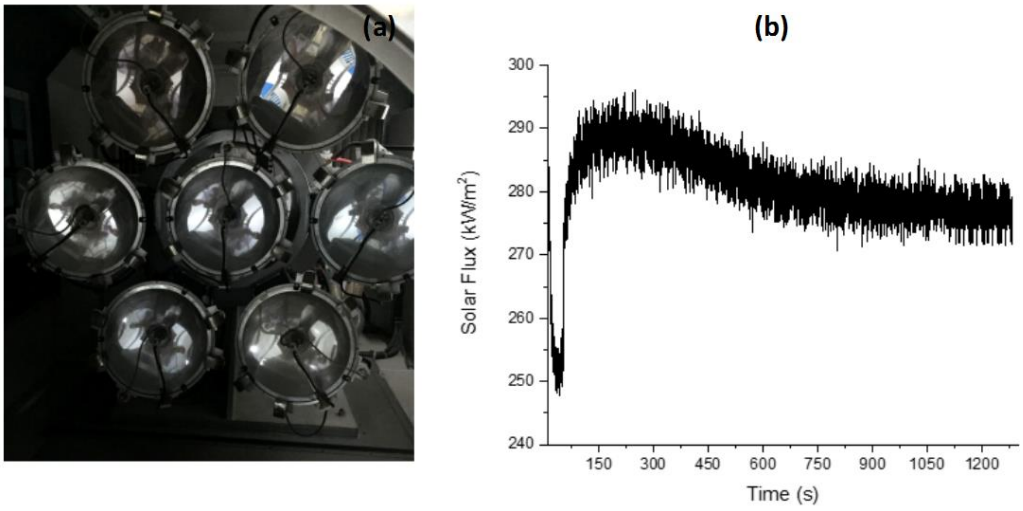

Figure 5. 1 Seven xenon lamps arranged to form a hexagonal shape, (b) Stability of the radiation flux after 12 min.

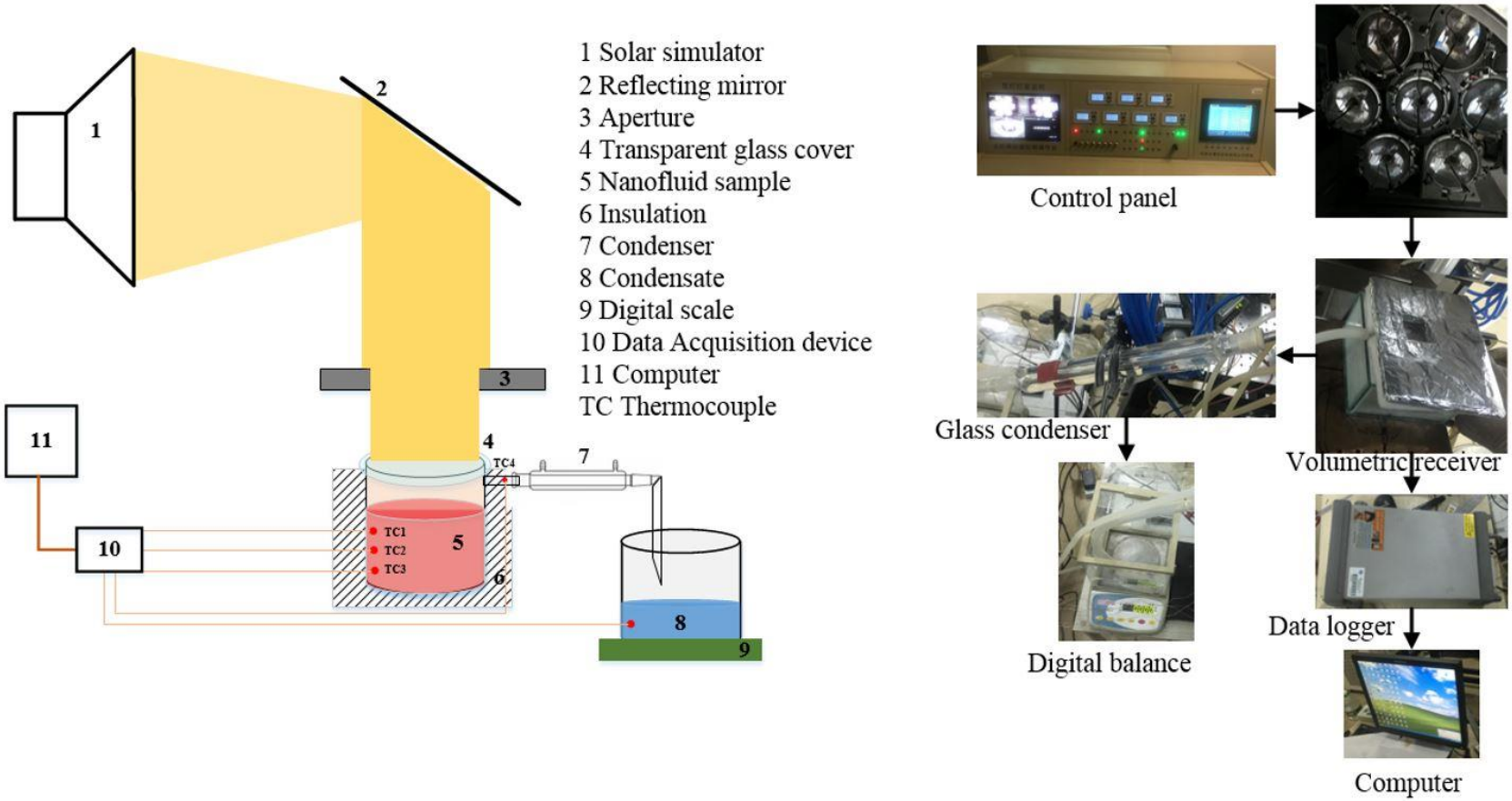

Figure 5. 2 Schematic of the experimental setup highlighting the major components.

Three K-type (Omega 5TC-TT-K-36-36) thermocouples (TC) were used to measure the bulk fluid temperature, positioned evenly along the optical depth in top, middle and bottom sections of the sample fluid at a distance of 10 mm from each other. This was to ensure that neither the top TC was exposed to the air during the experiment nor the bottom TC touched the bottom of the vessel. The temperature of the vapour generated was measured through an additional K-type thermocouple. The steam temperature was measured at the middle of a 20 mm long exit channel, as shown in **Fig. 5.2**. The temperature was registered by a data logger (Agilent 34970A) linked to a computer. The uncertainty in temperature measurement was validated as ±0.25 K. The generated steam was condensed in a glass condenser with cooling water circulating around the condensing tube. A sensitive digital balance (Setra, BL-500S) with uncertainty of ±0.001g was used to measure the mass of the condensed vapour.

5.3 Results and discussion

5.3.1 Optical absorption of the nanofluid samples

The optical absorbance of Au nanofluids was checked by UV/Vis spectrophotometer (U-3900, HITACHI) using a high precision cell with light path of 10 mm. The absorbance of Au nanofluid is shown in **Fig.5.3**, whereas the inset shows a linear relationship of the absorbance peak with the concentration. The absorbance peak of the Au nanofluid appears at a wavelength of 525 nm and is identical for various concentrations. The absorbance peak can be engineered and shifted towards longer wavelength by controlling the size and shape of the nanoparticles during the synthesis process.

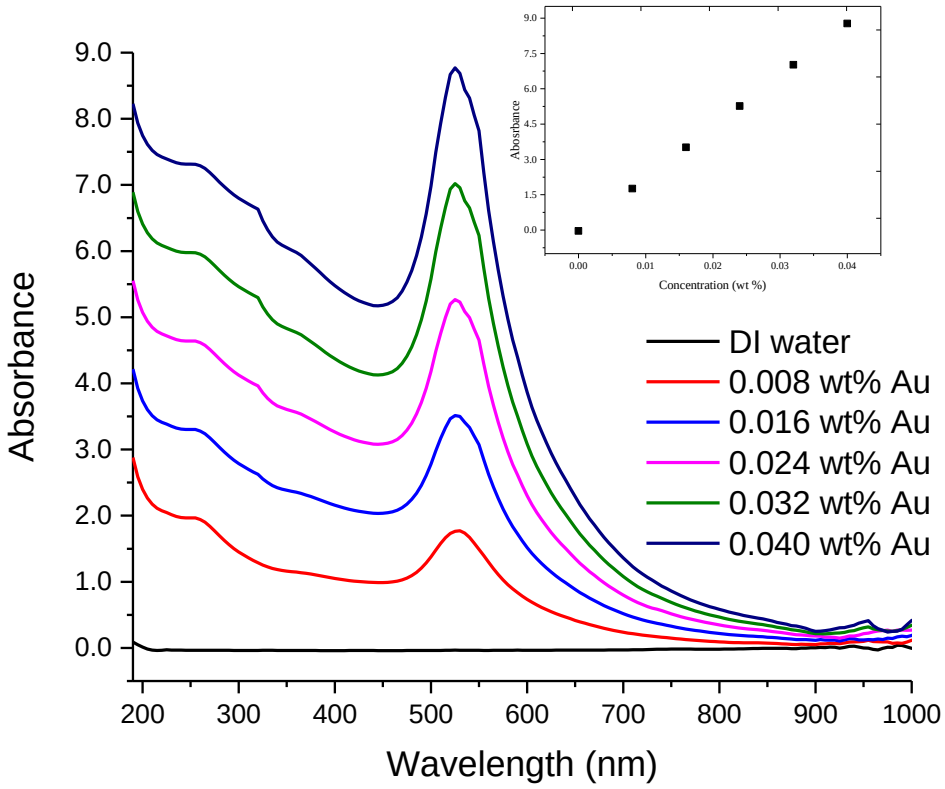

Figure 5. 3 Optical absorbance spectra of the gold nanofluids at various weight concentrations with absorbance peak at plasmonic resonance wavelength of 525nm. The inset shows a linear relationship of the absorbance peak with the concentration.

5.3.2 Fluid heating and steam characterization

The bulk fluid temperature was measured by three thermocouples TC1, TC2 and TC3 as the nanofluid sample was heated under a solar flux of 280 Suns. The top TC1 showed a rapid change in fluid temperature as the sample is illuminated. Depending upon the variation of bulk fluid temperature as given in **Fig. 5.4**, the fluid heating can be divided into three phases. The first phase is the heating of surface fluid with the underneath fluid in subcooled condition. The surface fluid reaches boiling temperature

rapidly and the temperature of the underneath layers of the fluid volume is slightly changed (**Fig. 5.4 and Fig. 5.6 (a)**). The second phase is the heating of bulk fluid volume in which the heat flux penetrates and brings the temperature of the whole fluid volume to the boiling.

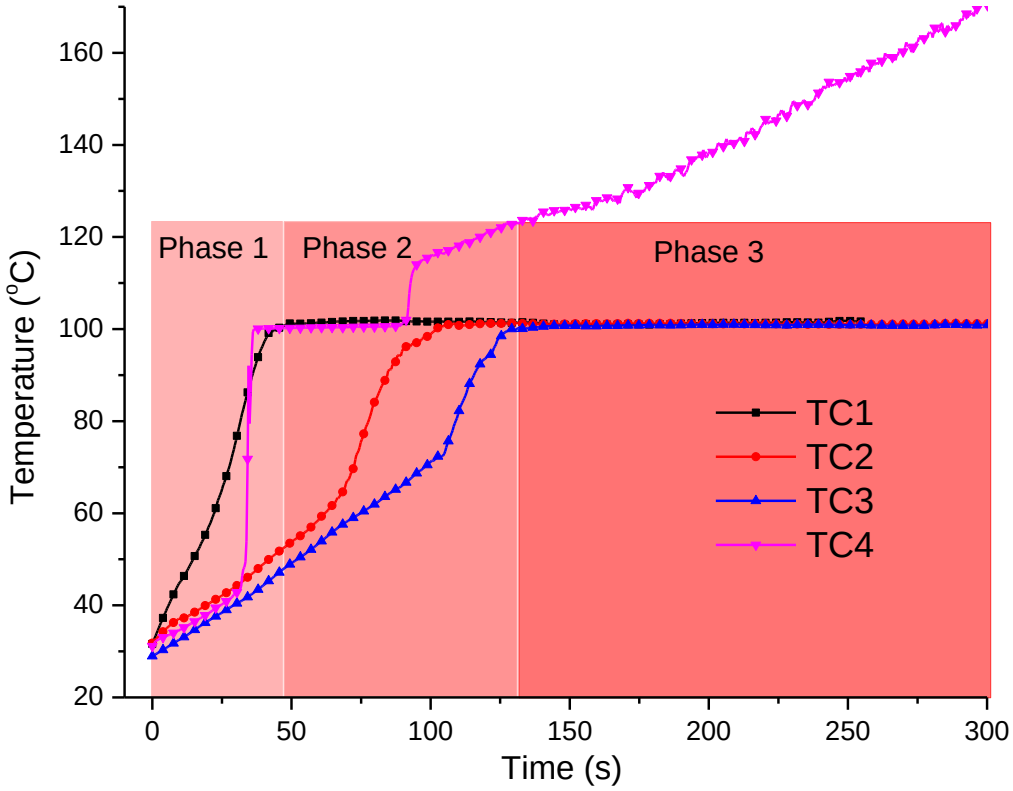

Figure 5. 4 Temperature distribution during the 5 min illumination of 0.016 wt% Au nanofluid sample where phase 1 shows the surface heating, phase 2 is the bulk fluid heating and phase 3 shows the saturated boiling of the sample. Here TC1, TC2 and TC3 are the temperatures of the thermocouples 1, 2 and 3 and TC4 is the temperature of the steam.

The third phase is the saturated boiling phase in which the sample volume temperature reaches the boiling point. Due to superheating, the steam temperature continues to increase above the boiling temperature until the radiation flux is switched off. The

temperature distribution in the first two heating phases can be clearly seen in **Fig. 5.6 (a)**, in which the concentration of gold nanoparticles is 0.04 wt%. The non-uniformity of temperature along the heating path is increased with the increase of nanoparticle concentration. This is associated with the increased radiation absorption at the surface due to more solar energy trapping at the surface at a higher concentration.

The temperature distribution for deionized water sample is shown in **Fig. 5.5 (a)** and the temperatures of the surface fluids in case of deionized water and 0.008 wt% Au nanofluid is given in **Fig. 5.5 (b)** as a comparison. It is evident from **Fig. 5.5** that for DI water, there is not much temperature variation along the heating path during the initial volumetric heating phase and the rate of rise in surface temperature is also much slower than that of 0.008 wt% gold nanofluid.

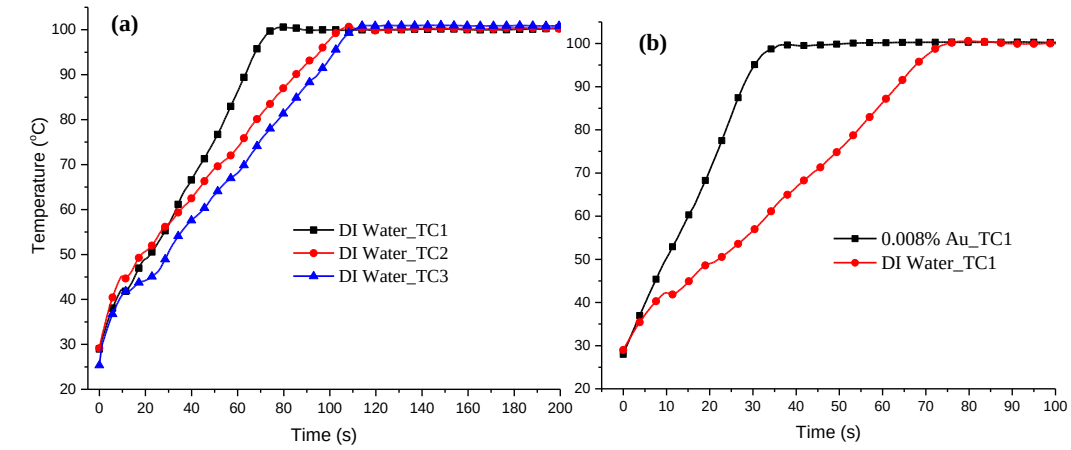

Figure 5. 5 (a) Temperature distribution in deionized water sample and (b) comparison of the surface temperatures (TC1) of 0.008 wt% gold nanofluid and deionized water

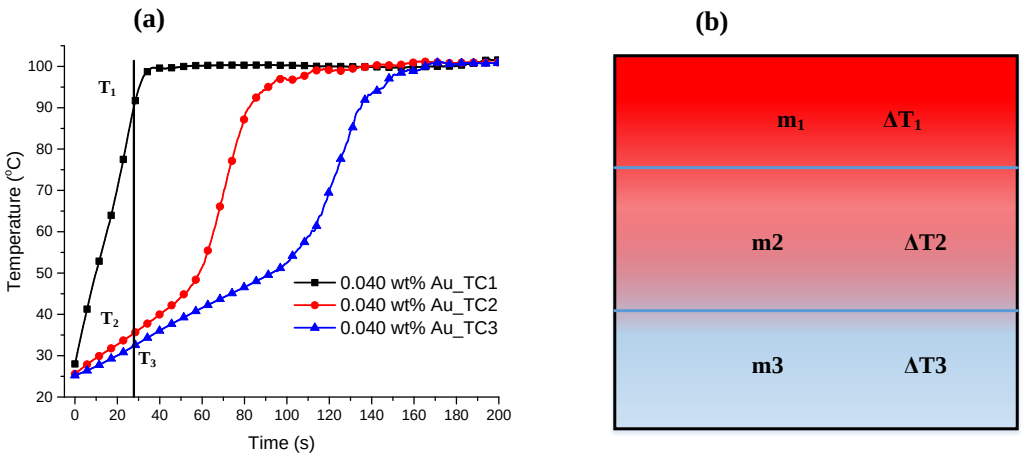

Figure 5. 6 (a) Variation of temperature along the depth of the 0.040 wt% Au nanofluid sample where T_1, T_2 and T_3 show the reading of thermocouples TC1, TC2 and TC3 respectively and (b) division of fluid volume into different levels as per the temperature distribution during fluid heating.

Although the thermophysical properties of water like thermal conductivity and specific heat capacity would be changed with the addition of nanoparticles. However with such a small nanoparticle concentration (0.040 wt%), the change in these properties was found to be negligible. The mass of the condensed vapor generated over a 5-min duration is given in **Fig. 5.7**, which shows a significanlty higher value for nanofluid samples . Comparing with DI water, an enhancement of 80% and 157% in the vapor generation efficiency are observed for gold nanofluids at 0.008 wt% and 0.040 wt% concentrations respectively. The amount of condensed vapor is increased nearly linearly with the increase of nanoparticle concentration, as presented in **Fig. 5.7 (inset)**. The variation in the mass of condensate at the initital volumetric heating of the samples with varying concentration is small, which might be due to the recondensation of the vapors. The vapors generated under subcooled conditions have greater tendency of recondensation due to the presence of cold vessel walls. A

constant evaporation rate after the phase two of the volumetric heating confirms the saturated boiling in the nanofluid sample. The uncertainty in the mass measurement for the sample with 0.008 wt% nanoparticle concentration was estimated to be ±0.592% for the first 60 seconds of illumination. The relative uncertainty in the calculated photothermal efficiency was estimated to be ±2%.

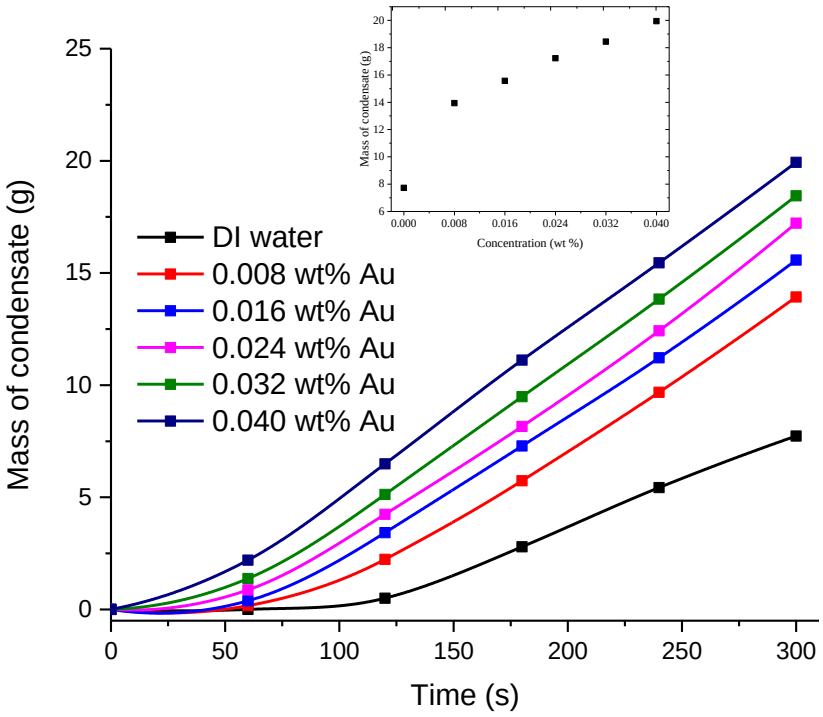

Figure 5. 7 Mass variation of the condensed vapours at different nanoparticle concentrations as the sample is illuminated with a radiation flux of 280 Suns for a period of 5 min.

Zhang et al. [21, 145] and Neumann [156] calculated the energy absorbed by the nanofluid during the sensible heating period using the following relation in Eq. (5.1) where only one temperature sensor was used to represent the bulk fluid temperature;

$$Q = c_p m \Delta T \tag{5.1}$$

where c_p, m and ΔT are the specific heat capacity, mass of the sample taken and temperature change of the fluid volume over the specified time. The change in temperature ΔT was replaced by $\Delta \bar{T}$, i.e., the average temperature difference by Jin et al. [146, 147], in which more than one thermocouple were used. As clearly seen from **Fig. 5.6 (a)** that the fluid temperature is highly non-uniform, the temperature measured by only one thermocouple is clearly not representative of the fluid temperature. The calculated absorbed energy may be overestimated or under-estimated depending upon the position of the thermocouple. Even the average value of the temperature may also be misleading depending upon several factors, including the type of nanoparticles, their concentrations, colour of the nanofluid and intensity of radiation flux.

Here we use a more realistic method to calculate the energy absorbed by the nanofluid volume. The fluid volume is divided into various temperature dependent sections as shown in **Fig. 5.6 (b)**. The absorbed energy of each section is calculated independently and the overall absorbed energy is evaluated using the relation given in Eq. 5.2;

$$Q = c_p \sum_{i=1}^{n} (m_i \Delta T_i) \tag{5.2}$$

The overall photothermal conversion efficiency (η_{PTC}) including sensible heating and latent heat is subsequently calculated from Eq. 5.3, which is a modified version of the equation used by Jin et al. [147];

$$\eta_{PTC} = \frac{c_p \sum_{i=1}^{n} (m_i \Delta T_i) + \int_0^t L_v m_v dt}{\int_0^t I A_a dt} \tag{5.3}$$

where I is the solar irradiance, A_a is the area of the aperture, L_v is the latent heat of vaporization of water and m_v is mass of the condensed vapours in time dt.

Fig 5.8 (a) shows the photothermal conversion efficiency during the first phase, i.e. surface heating which is typically less than 30 seconds after the heating. The efficiency includes the sensible and latent heat contributions. The position of the thermocouple has a great influence in determining the photothermal efficiency. If only one thermocouple is used for the measurement of temperature change as in [21, 145, 156] and the optical length of the fluid volume is significant, the obtained photothermal efficiency would be underestimated if the thermocouple is away from the surface (as TC3 here in this study) and overestimated if it is close to the surface (as TC1 in this study). This underestimation or overestimation is because the temperature of the respective thermocouple is used to represent the temperature of the whole fluid volume at any instant, but actually it is not as already shown in **Fig. 5.6 (a)**.

Using the proposed method of calculating the photothermal efficiency, i.e. taking the temperature distribution into account, gives more realiable results and is necessitated particulary when the temperature remains below the boiling temperaure of the nanofluid.

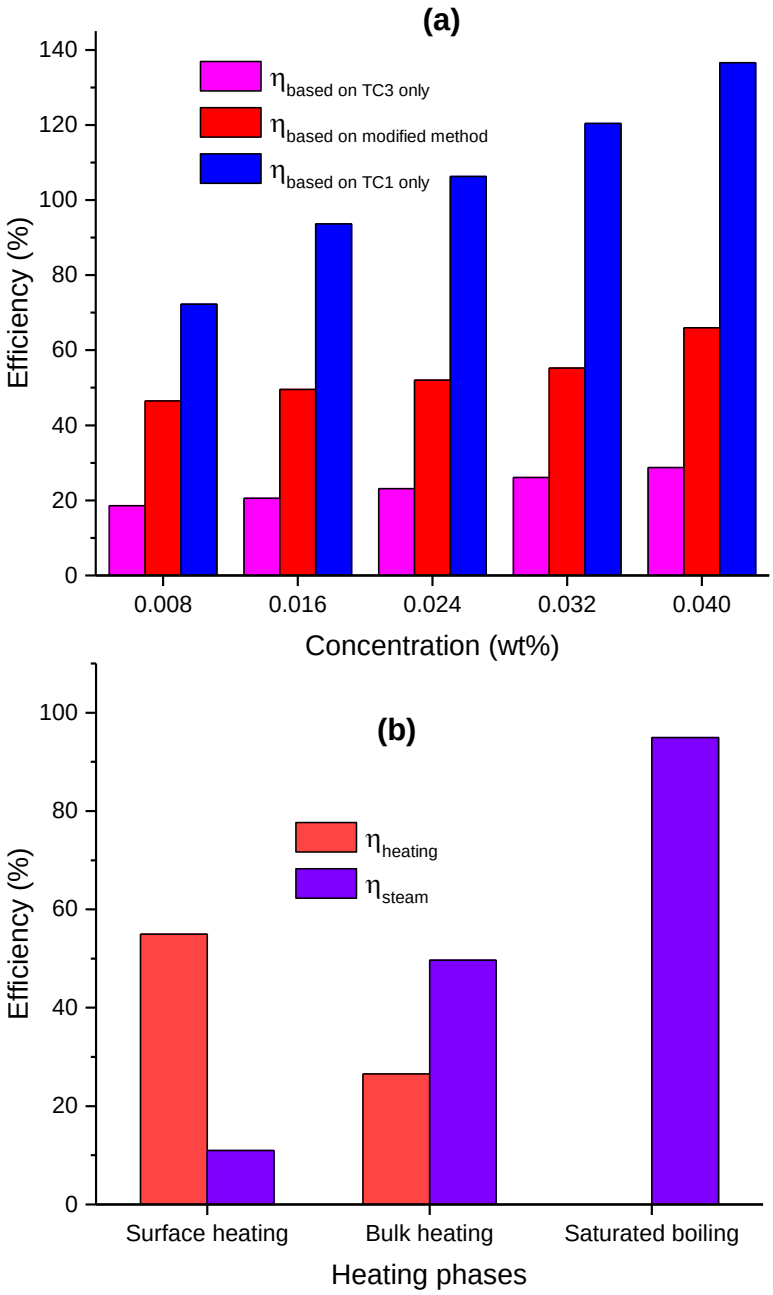

Figure 5. 8 (a) Efficiency (including latent heat) based on individual thermocouple and modified method at various nanoparticle concentrations during the phase 1 only and (b) Efficiency of sensible heating and steam generation during the three heating phases of 0.040% gold nanofluid sample where $\eta_{heating}$ is based on modified method.

Fig. 5.8 (b) shows the variation in the efficiency of sensible heating and steam generation in the proposed three phases during the irradiance time of 5 min for a nanoparticle concentration of 0.040 wt%. During the surface heating, most of the absorbed energy is used in the sensible heating of the nanofluid, together with some vapor generated.while in case of DI water, no vapours were observed on the surface of heated phase. Hence the presence of nanoparticles enhances the steam generation efficiency even under subcooled conditions as also observed by Jin et al. [147]. The steam generation efficiency of about 95% in the saturated boiling is very attractive and gives an enhancement of 117.5% over the base fluid.

Fig. 5.9 shows the overall efficiency of the plasmonic gold nanofluid at various concentrations compared to the base fluid. The photothermal efficiency is dramatically enhanced by gold nanoparticles. At a concentration of 0.040 wt%, the overall photothermal efficiency or in a broader term the energy efficiency is enhanced by 95% over the base fluid in the experimental domain. This enhancement increases almost linearly with the nanoparticle concentration. It can also be noticed that the efficiency difference among the three modes of its evaluation is negligibly small when there are no nanoparticles in the base fluid. But with the addition and increase in the concentation of the nanoparticles, this difference is magnified. This is due to the non-uniform temperature distribution caused by the presence of the nanoparticles. This non-uniform temperature distribution is very supportive in evaporating the fluid from the surface while keeping the bulk volume under subcooled conditions. This phenomenon can be used to produce clean water by evaporating the water from the surface and keep circulating the underneath volume like in forward osmosis desalination.

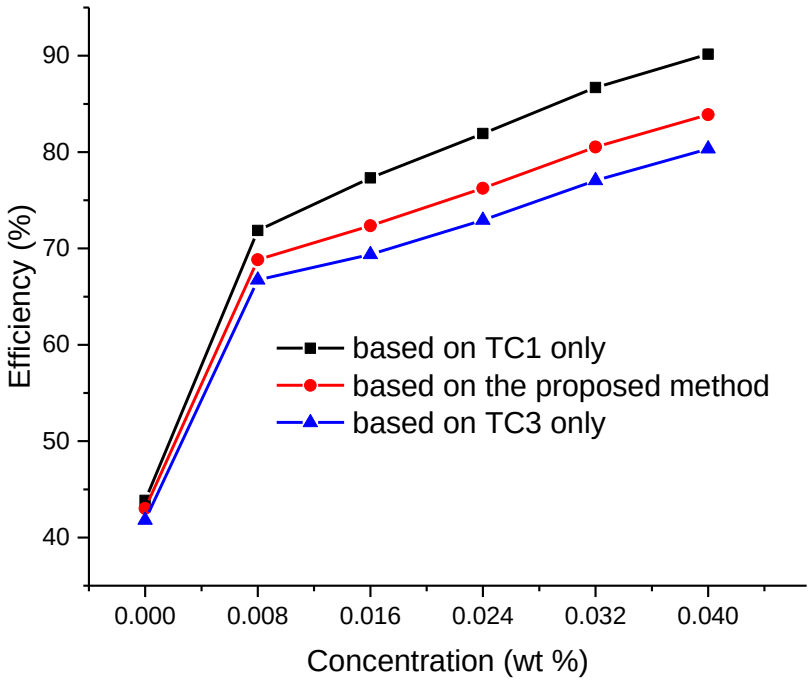

Figure 5. 9 Photothermal conversion efficiency (η_{PTC}) based on three methods at various nanoparticle concentrations over an irradiation time of 5 min.

5.3.3 Analysis of nanoparticles after experiments

The remaining concentrated nanosuspension after the photothermal experiments was examined in terms of stability, nanoparticle size distribution and morphological appearance it had undergone. **Fig. 5.10 (a) and (b)** represent the TEM micrograph and hydrodynamic size distribution of the particles after boiling, repectively. Compared with the characterization results before the experiment, the size and shape of the gold nanoparticles is almost the same after the experiment. The hydrodynamic size distribution of the nanoparticle is slightly changed and has a maximum intensity at 44 nm, which was at 49 nm before the experiments.

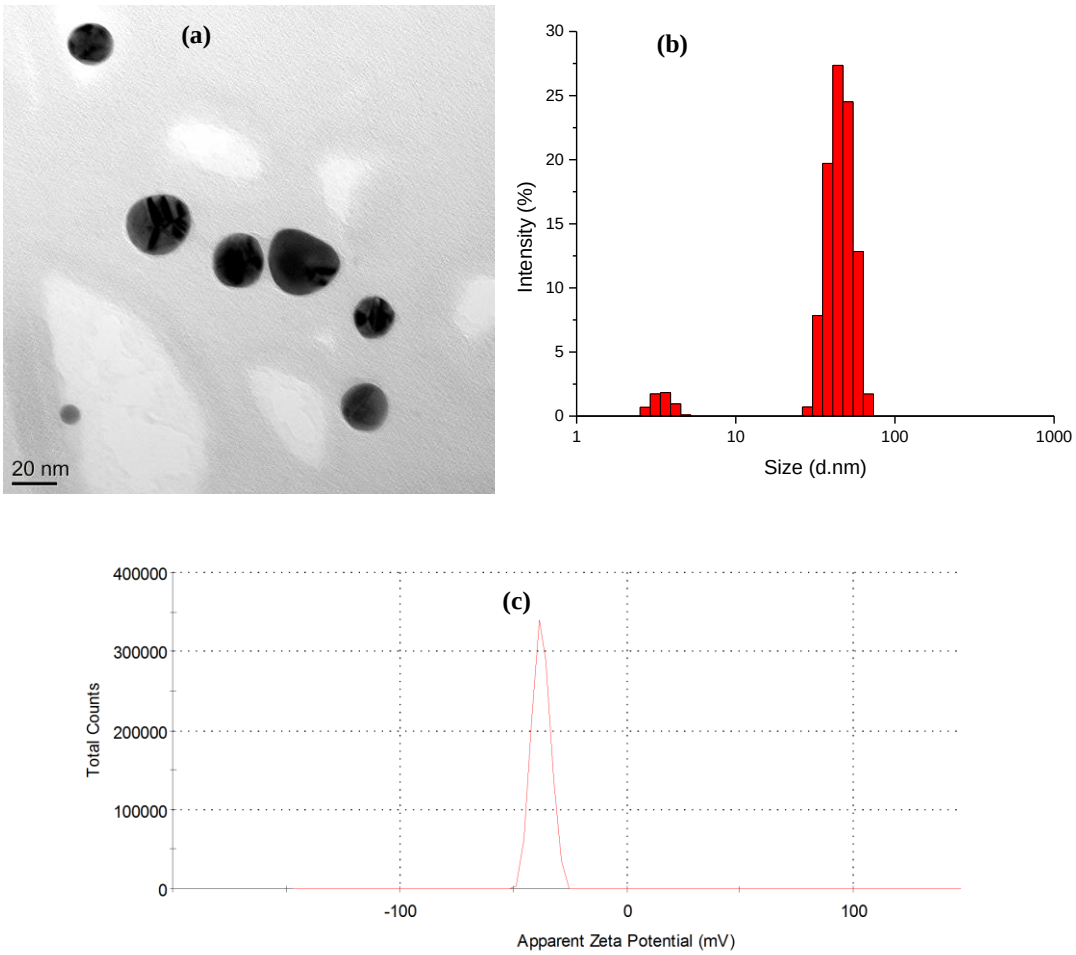

Figure 5. 10 Characterization of nanoparticles after the steam generation experiment. (a) TEM micrograph, (b) particle size distribution, and (d) zeta potential graph.

The size inensity distribution is more compact and peaked after the photothermal coversion experiments. An additional smaller peak is observed in the DLS size distribution. This might be due to the collapse of the surfactant layer on the surface of the nanoparticles. The zeta potential of the nanofluid after the steam generation experiement is about -37 mV as shown in in **Fig. 5.10 (c)**, which indicates a good stability of the suspension.

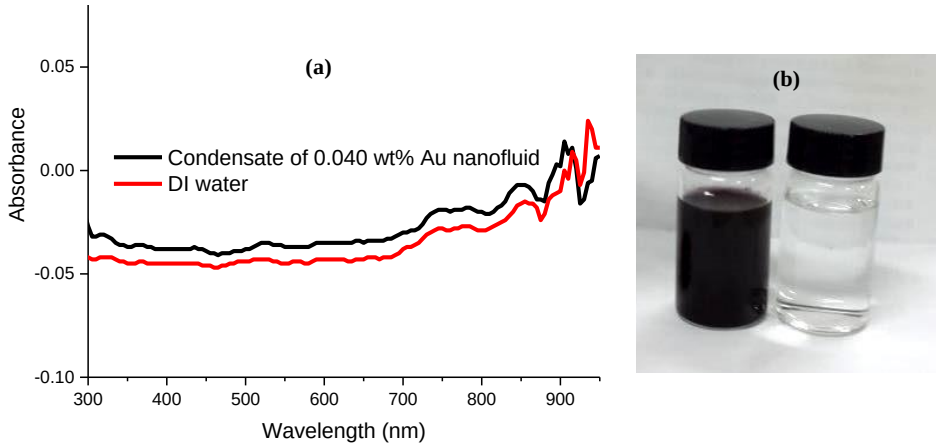

Figure 5. 11 (a) Optical absorbance spectrums of the condensate and that of deionized water showing the absence of gold nanoparticles and (b) Gold nanofluid (on left side) and the clear condensed vapours as water (on right side)

As to the possible nanoparticle entrainment phenomenon, **Fig. 5.11(b)** shows that the remaining concentrated gold nanofluid in dark red wine color and the condensate is transparent i.e. there is no gold nanoparticles in the condensate. This was further confirmed by the UV/Vis spectrum of the condensate presented in **Fig 5.11 (a)** which shows an almost overlapping otical absorbance spectrum of the condensate and deionized water and the absensce of any absorbance peak at 533 nm wavelength indicates that no particles were blown out with the steam even under strong boiling conditions.

5.4 Chapter summary

A well-controlled steam generation experiment was performed by using gold nanofluids under a concentrated solar flux of 280 Suns. The temperature distribution was highly non-uniform and three phases were identified as surface heating, subcooled boiling and saturated boiling during the nanofluid exposure to concentrated solar radiation flux. The photothermal performance and steam generation efficiency was directly dependant on the concentration of the Au nanoparticles. An enhancement of about 95% in the photothermal performance over the base fluid was observed with a nanoparticle concentration of 0.04 wt% only. The analysis of condensed steam proved that no nanoparticles were entrained even under vigorous boiling. These results confirmed that nanoparticle assisted solar steam generation can be realistically used to produce potable water using solar energy in arid areas.

Chapter 6

FO Performance of Nanofluid based Draw Solutions

This chapter deals with the experimental results regarding FO performance of the direct absorptive nanofluid based novel draw solutions in terms of osmotic pressure, water flux, reverse solute flux. It also includes the solar energy based regeneration of the novel draw solutions and recovery of product water. The quality of product water is analysed and compared with potable water standards.

6.1 Introduction

Osmotically driven forward osmosis (FO) process has numerous advantages over the pressure-driven reverse osmosis (RO) such as low energy intensity, less membrane fouling, minimum environmental impact of the salt concentrate, reversibility of membrane fouling, low reverse solute flux [5, 92-95] and high water recovery [106, 166]. However, appropriate draw solutions (DS) having high osmosis pressure, low revers flux of solute particles, easy regeneration and causing minimum membrane propensity are still to be developed to make FO a viable solution for potable water issues.

Various types of media have been experimented as FO draw solutions which can be broadly categorized as conventional DS including gas or volatile compounds [115, 116, 166, 167], inorganic [168-171] and organic solutes [172-174], and organic coated-nanoparticles dispersed in different solvents [175-180]. Organic coated magnetic nanoparticles (MNPs) are a recent addition to FO draw solutions which can be regenerated using a strong electric or magnetic field followed by ultrafiltration process as discussed in detail in section 2.3.3.3 of chapter 2. Nanoparticles have the advantage of high surface area to volume ratio and larger size in comparison with ions and molecules of organic and inorganic draw solutions.

The studies discussed in chapter 2 have shown a number of problems arising from the use of MNPs as draw solutes in FO desalination. Though these investigations are preliminary results, they are facing the problems of agglomeration, reduced water flux after several runs and recovery problem of the nanoparticles even after using strong

magnetic field and nano filtration. Hence there is a strong prospective to develop and explore nanofluid based draw solutions using other nanoparticles and renewable energy based regeneration.

Dual function potassium doped carbon nanofibers (K/CNF) in tri ethylene glycol (TEG) aqueous solution are evaluated as novel draw solution (NDS) for producing potable water. The NDS not only have high osmotic pressure to develop a high water flux across the FO membrane but also a high solar absorption capability to separate product water and regenerate draw solution. This is a unique work of its kind and utilizes the solar energy for water desalination using osmotically driven forward osmosis process. Several surface treatments were implemented to make the TEG-K/CNF composite osmotically active and a laboratory scale cross flow FO cell was used to evaluate the performance of the NDS experimentally. The photothermal performance in water recovery phase was evaluated using a simulated solar flux and the quality of water was examined though several water quality tests and were compared with water standards.

6.2 Experimental settings

The performance of K/CNF as a novel draw solution (NDS) was investigated using a laboratory scale cross flow forward osmosis cell (CF042 FO, Sterlitech, USA) as shown schematically in **Fig. 6.1**.The FO cell has active membrane area of 42 cm^2. A pre-wetted forward osmosis flat sheet membrane (Aquaorin Inside) was used to measure the water flux of NDS against deionized water and synthetic brackish water as feed solution. The FO membrane was used in FO mode i.e active layer facing the feed solution (AL-FS). NDS with various concentrations of K/CNF and TEG was

used to experiment the water permeation rate across the FO membrane. The water permeation was measured over a period of two hours after giving a first 15 minute time to settle the flow fluctuations. A crossflow velocity of 8.50 cm/s was used on both the draw side and the feed side. A digital balance (AND, EK-3000I) was used to measure the weight change of the feed solution over the experiment time.

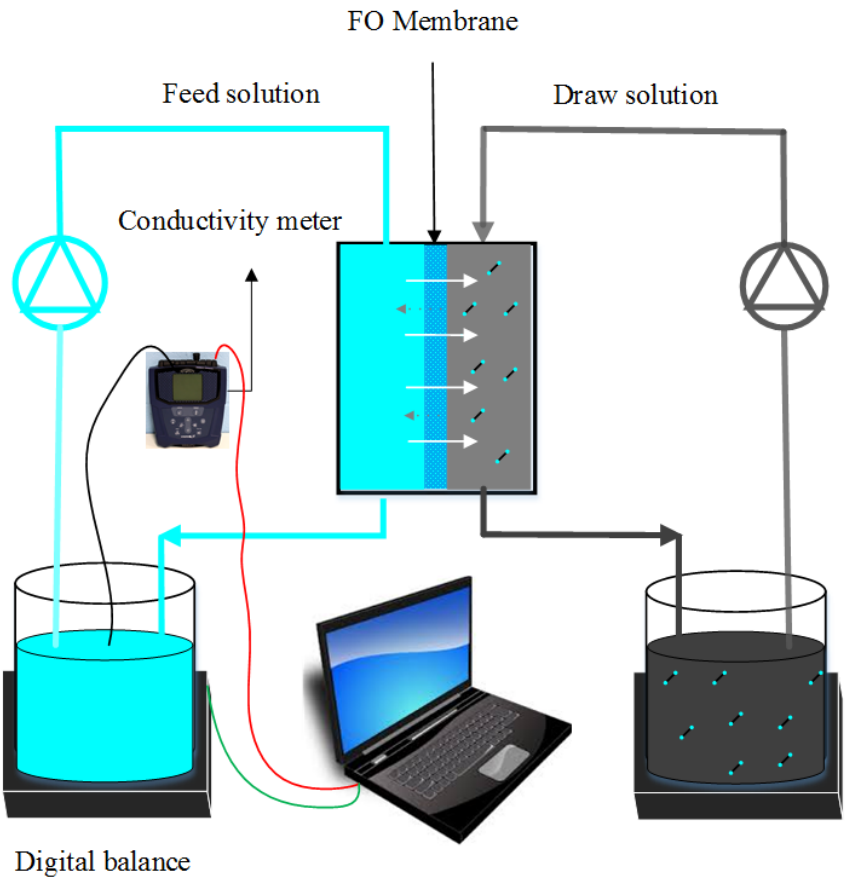

Figure 6. 1 A Schematic of the experimental laboratory scale FO setup for the investigation of water flux and reverse solute flux

The water permeation flux (J_w) in $Lm^{-2}h^{-1}$ (known as LMH) was calculated by measuring the weight change of the feed solution over predetermined time using relation [181] given in Eq. (6.1);

$$J_w = \frac{\Delta m}{\rho_f A \Delta t} = \frac{\Delta V}{A \Delta t} \quad (6.1)$$

where Δm is the weight change of feed solution over predetermined time (Δt), ΔV is change in volume (L) of the feed solution in time Δt (h) and A is active membrane area (m^2).

The reverse solute flux was calculated by measuring the conductivity of the feed solution at an interval of every 5 min with a calibrated conductivity meter (VWR, SB70C) using the following relation (6.2);

$$J_s = \frac{C_t V_t - C_o V_o}{A \Delta t} \quad (6.2)$$

where J_s is the reverse solute flux in $gm^{-2}h^{-1}$ (also known as GMH), C_o and C_t are the concentrations of the feed solution at start of the experiment and at time Δt respectively, V_o and V_t are the volumes of the feed solution (L) at start and at Δt respectively.

The regeneration of the nanofluid based NDS and the product water separation was achieved through simulated solar radiation flux. The same solar simulator was used as a source of solar flux, already explained in Section 4.2 of Chapter 4. A vessel made of high temperature quartz glass with the inner and outer diameter of 30 mm and 34 mm respectively was used as sample container. The vessel was put accurately under the solar radiation flux to enable a uniform heating as shown schematically in **Fig. 6.2**. A sample fluid of 27 ml (~38.2 mm depth) was irradiated for a time of 20 min. A transparent quartz cover and a condenser was integrated with the vessel to collect water vapours for a prolonged irradiation time to analyse the quality of product water.

Holes of 1 mm diameter were fabricated in the vessel to insert the thermocouples at 8, 16, 24 and 32 mm depths from the top.

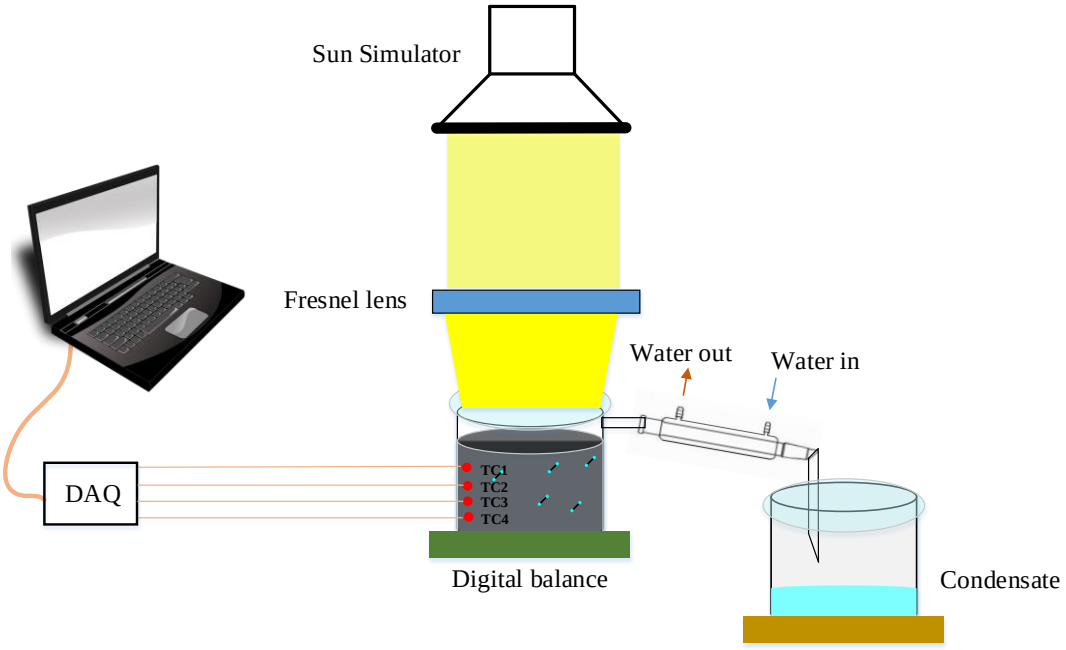

Figure 6. 2 Schematic of the draw solution regeneration setup

Four K-type (Omega 5TC-TT-K-36-36) thermocouples (TC) were used to measure the bulk fluid temperature, positioned evenly along the optical depth of the sample. The data were registered by a data acquisition device (NI SCXI-1303) using LabVIEW software at a sampling rate of 1 Hz. The uncertainty in temperature measurement was ±0.5 ^{o}C. A digital balance (Ohaus, Mettler Toledo) with uncertainty of ±0.001 g was used to measure the mass change over time as the sample was radiated with solar flux. Various weight concentrations of K/CNF were used to investigate the solar absorption for draw solution re-concentration.

6.3 Results and discussion

6.3.1 Osmotic pressure analysis

The driving force for osmotically driven FO process is the osmotic pressure. The osmotic pressure of the NDS was measured in terms of osmolality using an osmometer (Advance Instruments, 3900) based on the principle of freezing point depression. The osmolality of samples containing various concentrations of K/CNF and TEG is presented in **Fig. 6.3**.

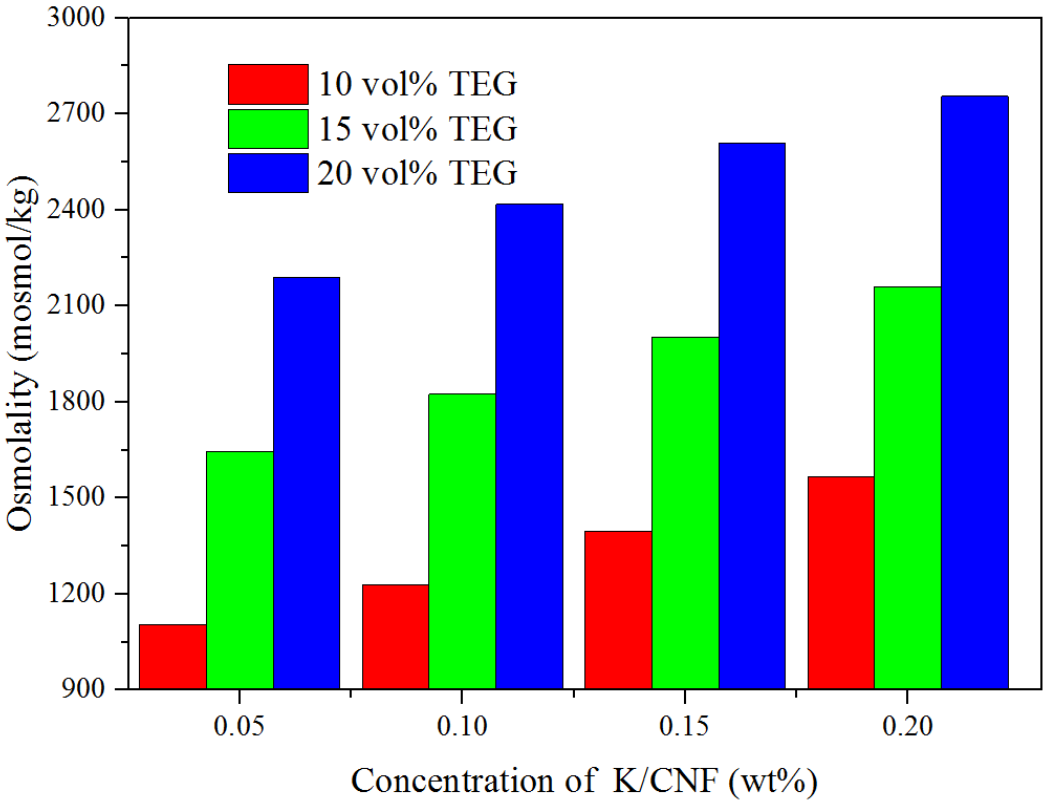

Figure 6. 3 Osmotic pressure in terms of osmolality of the novel DS at various concentrations

The osmolality of DS is almost linearly dependent on the concentration of novel draw solute (K/CNF) from 0.05 to 0.20 wt% as well as TEG. The osmotic pressure (π) can

be calculated from the osmolality value using the relation ($\pi = 19.3 \times$ Osmolality) given by [182] where osmolality is in mosmol/kg and osmotic pressure in mm of Hg which can be converted into bar by multiplying by 1.32 x 10^{-3}. The osmolality of NDS with TEG concentration from 10 to 20 vol% ranges from 1104 to 2754 mosmol/kg which corresponds to osmotic pressure from 28 to 70.3 bar, respectively.

The NDS in the present work are osmotically more active as compared with the other nanomaterial based FO draw solutions, yet with an innovative solar energy based easy regeneration. For example Guo et al. [183] used Na-functionalized carbon quantum dots (Na-CQDs) with a 50 wt% concentration of Na-CQDs which could develop osmotic pressure of 54.3 bar only and regeneration was carried out by complex membrane distillation. Similarly, Zhao et al. [184] used up to 30 wt% of citrate coated MNPs as FO draw solution which could only develop 58.4 bar osmotic pressure to be used for protein enrichment. The NDS fabricated in this work exhibited an osmotic pressure of 70.3 bar with a much smaller concentration of the draw solute compared to above mentioned draw solutions.

Compared with osmotic pressure of seawater which is around 26 bar [184], the osmotic pressure of the DS with K/CNF and TEG concentration of 0.2 wt% and 20 vol% respectively was about 70.3 bar and has the potential to desalinate seawater. The structure of TEG-K/CNF composite enriched with hydroxyl (-OH), carboxylic (-COOH) groups and K-species which could result in easy and increased intermolecular hydrogen bonding. The hydrogen bonding in the presence of these rich ionic species resulted in higher osmolality values [185] and thus higher water permeation flux in FO experiments.

6.3.2 FO performance of novel draw solution

The performance of NDS was investigated in terms of water permeation flux (LMH) and reverse solute flux (gMH) through a laboratory scale cross flow FO cell against deionised water and synthetic brackish water as feed solutions. The FO experiments were performed in FO mode i.e. the active layer of the membrane facing the feed solution. The water permeation flux and reverse solute flux of NDS having various concentrations of K/CNF and TEG against deionized water as feed solution are presented in **Fig. 6.4**. The water flux increased linearly with the increase in concentration of K/CNF at a given TEG volume concentration. For example, with 20 vol% of TEG, the water permeation flux increased from 10. 5 LMH to 13.3 LMH as the concentration of K/CNF was increased from 0.05 wt% to 0.2 wt% respectively. This is because the increasing concentration of K/CNF causes an increase in the net osmotic driving force.

The concentration of TEG also enhances the water flux for a given concentration of K/CNF because of its hydrophilic nature. For a concentration of 0.2 wt% of K/CNF, the water flux was increased from 7.5 LMH to 13.3 LMH when the volume concentration of TEG was increased from 10 vol% to 20 vol% respectively. The presence of hydroxyl and carboxylic functional groups in TEG-K/CNF hybrid made them highly hydrophilic and thus increased water flux across the membrane.

Several investigations used magnetic nanoparticles (MNPs) with different coating agents to evaluate their performance in FO process. For example, Bai et al. [186] investigated dextran coated magnetic nanoparticle based draw solution where they used about 78 wt% dextran in the solution and could only achieved a water flux of

about 4 LMH with deionized water as feedstock, Na et al. [117] experimented citrate coated MNP with 48.5 wt% concentration of sodium citrate and observed a water flux of 6.2 LMH in the first 5min of FO operation which was exponentially declined with time.

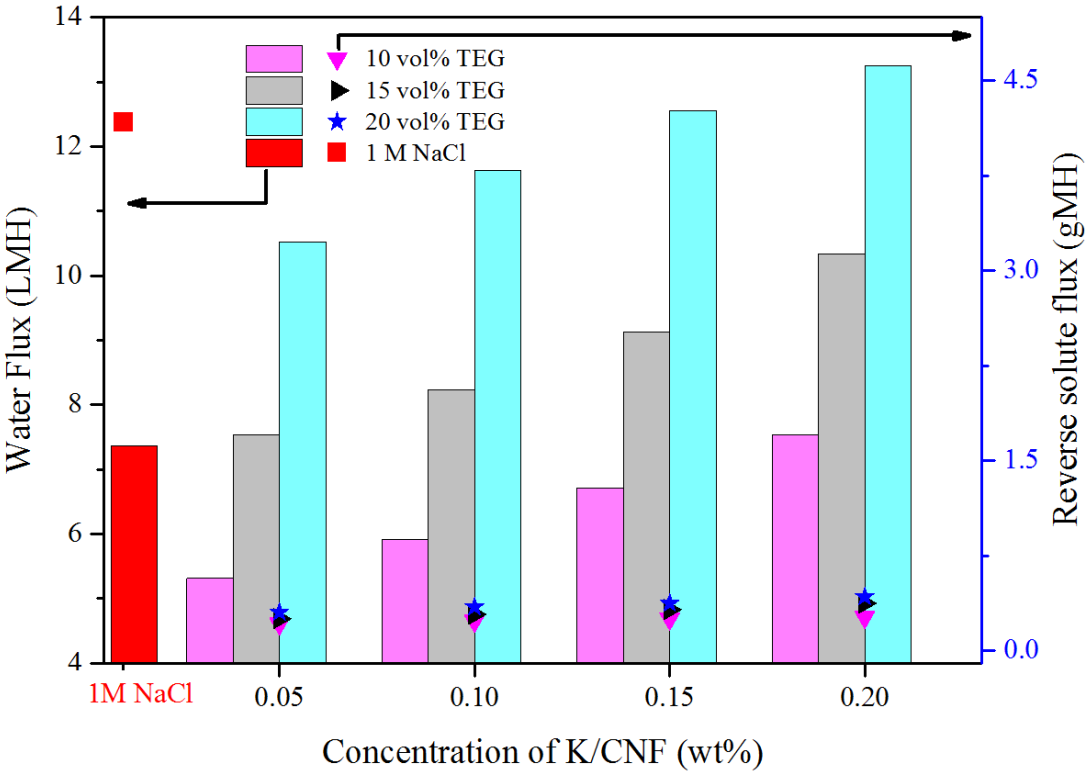

Figure 6. 4 Water flux and reverse solute flux against various concentrations of K/CNF and TEG with deionized water as feed solution

Similarly, Ge et al. [119] observed a water flux of 9 LMH in first 30 min using PEG coated MNPs and Ling et al. [118] achieved 7.7 LMH with PAA acid coated MNPs with deionized water as feed solution. Compared with the above mentioned coated MNPs in FO process and their complexity and deteriorating performance during regeneration under strong magnetic field, the novel draw solution in the present work

only contained maximum of 20 vol% TEG and developed a water flux of 13.3 LMH yet with an easy regeneration using solar energy.

The water flux of NDS was compared with that of a widely used model FO draw solute, sodium chloride with 1M concentration. As shown in **Fig. 6.4**, the water flux for 1.0 M NaCl draw solution was around 7.4 LMH which is almost equal to that of 0.05 wt% K/CNF in 15 vol% TEG. With this much of water flux, if the solute leakage (J_s) across the membrane is considered, it can be seen from **Fig. 6.4** that the reverse solute flux for 1M NaCl as DS was 4.2 gMH while it is only 0.25 gMH for the TEG-K/CNF draw solution. The maximum experimental reverse solute flux for the NDS was even less than 0.5 gMH. A very lower value of J_s in case of TEG-K/CNF draw solution shows a strong binding between the K, CNF and TEG which suppressed solute diffusion across the membrane. The reverse solute flux results in membrane fouling and a decline in water flux in long term operations as well as loss of draw solution [187].

The ratio of reverse solute flux to water flux (J_s/J_w) is known as specific solute flux and is one of the important parameters to judge the performance of FO process. The specific solute flux (gL^{-1}) is the amount of solute leakage from the draw side to the feed side for one litre of water permeation. The specific solute flux in case of 1M NaCl as DS was 0.56 g/L while it is only 0.031 g/L for the maximum concentration of TEG-K/CNF draw solution within the domain of this work which is negligibly small. Very small value of specific solute flux for the novel DS implies its long term operation in the FO process.

The FO performance of the novel draw solution was also checked against synthetic brackish water containing 3 wt% NaCl solution as feed water. **Fig. 6.5** shows the water flux at different TEG-K/CNF concentrations against synthetic water as feed solution. Though, the water permeation flux is reduced with NaCl solution as feed water but still the novel DS have enough osmotic force to produce a water flux of 5.7 LMH at a K/CNF concentration of only 0.05 wt% in 20 vol% TEG aqueous solution. A water flux of 8.6 LMH was observed with 0.2 wt% K/CNF concentration when TEG was 20 vol% in the draw solution and 3 wt% NaCl solution as feed water indicating that the NDS was still osmotically strong enough in the domain of this work to desalinate brackish water with even higher salinity level.

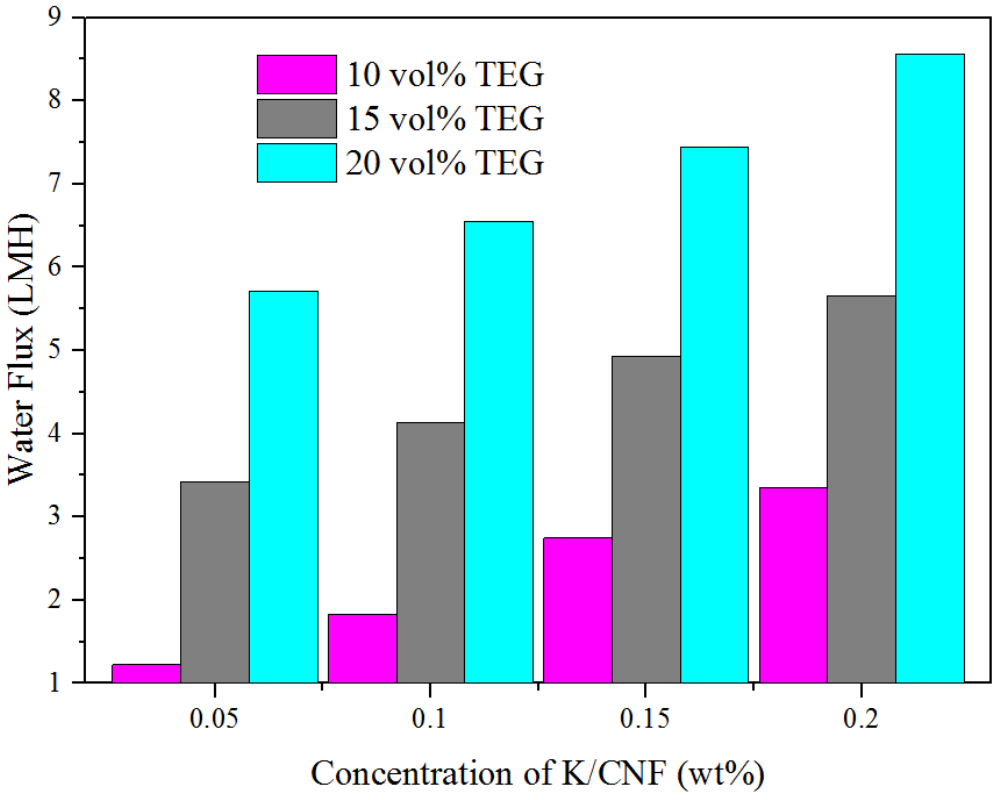

Figure 6. 5 Performance of novel draw solution at various concentration with synthetic brackish water (3 wt% NaCl solution) as feed solution

Fig. 6.6 shows the FO performance of the novel DS with concentrations of 0.2 wt% and 20 vol% of K/CNF and TEG respectively over 5 runs with DI water as feed solution. The diluted DS after every cycle was concentrated by evaporating the water to bring it back to the original concentration. The water flux of 13.3 LMH was observed in first run and then though, there was a slight decline but still it was 12.9 LMH for the fifth run. A very small decline in water flux over the five runs shows the suitability for long term performance of the novel DS.

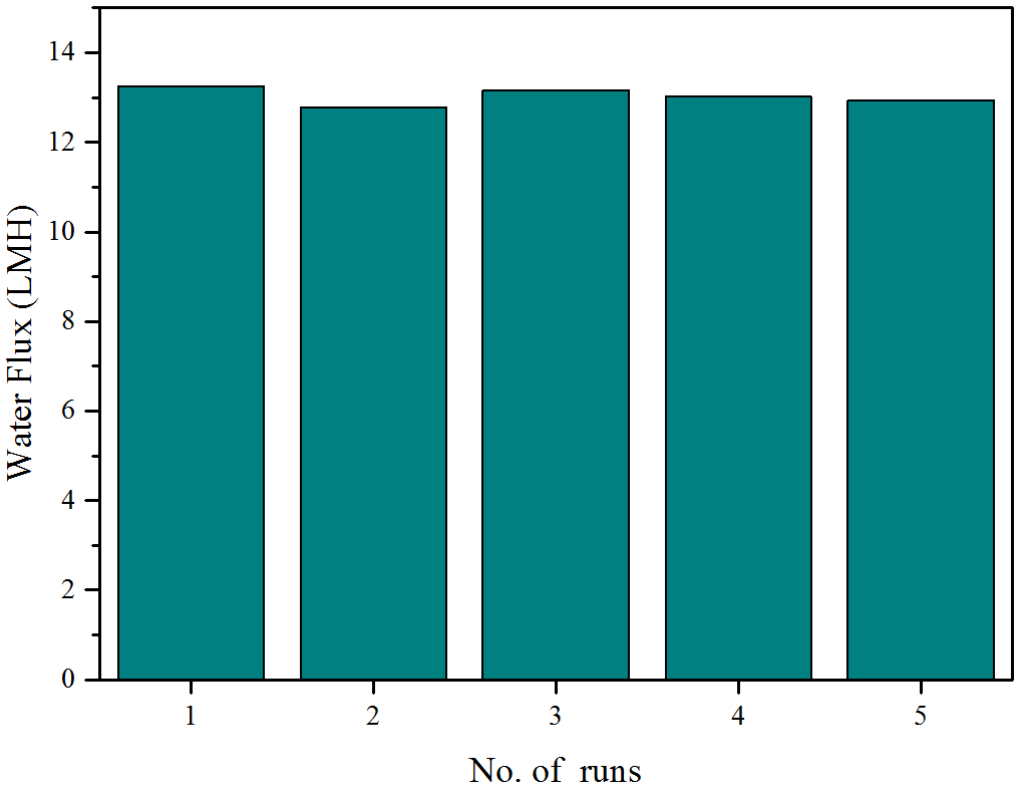

Figure 6. 6 Cyclic FO performance of novel draw solution having 0.2 wt% K/CNF in 20 vol% TEG

6.3.3 Solar energy based regeneration of draw solutions

Draw solution regeneration and product water recovery is the second phase in FO desalination. The NDS did not only developed high osmotic pressure and thus enhanced water flux across the FO membrane but was also highly absorptive to the solar radiation influx. The optical absorbance spectra of the TEG-K/CNF solutions given in **Fig. 6.7** shows that with a given TEG volume concentration, the absorbance was directly dependant on the concentration of K/CNF in the solution.

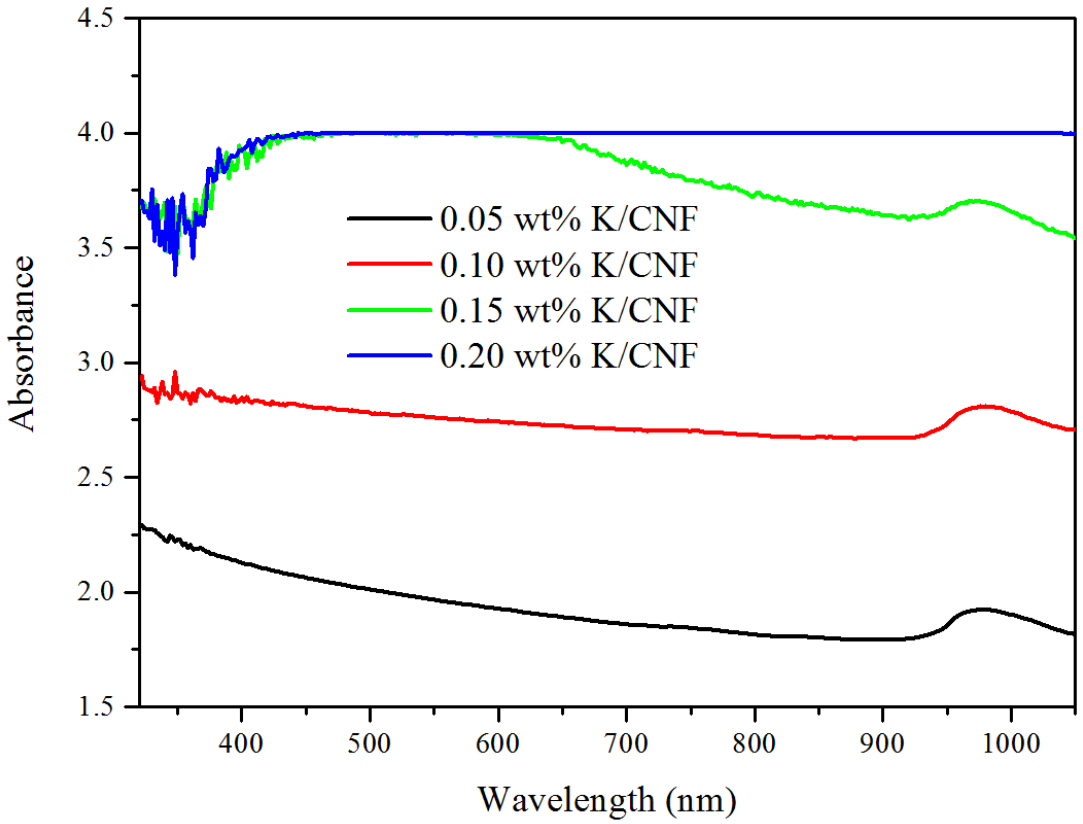

Figure 6. 7 Optical absorbance of novel draw solution samples at different concentrations of K/CNF suspended in 20 vol% TEG aqueous solution

While the optical absorbance was slightly decreased with the TEG increased concentration for a given K/CNF concentration as shown in **Fig. 6.8** where with 0.05

wt% of K/CNF, the optical absorbance was decreased when the concentration of TEG increased from 10 to 20 vol%.

The photothermal performance of NDS was evaluated by the experimental setup as described in Section 6.2. A sample volume of 27 ml was used to evaluate the temperature rise by means of four K-type thermocouples installed at 8, 16, 24 and 32 mm along the optical depths of the sample volume. A digital balance was used to measure the change in mass as the sample was exposed to the simulated radiation flux of 10 suns (one sun being equal to 937 W/m^2) over 20 min duration. The change in temperature as well as in mass was measured when the NDS sample was exposed to radiation flux.

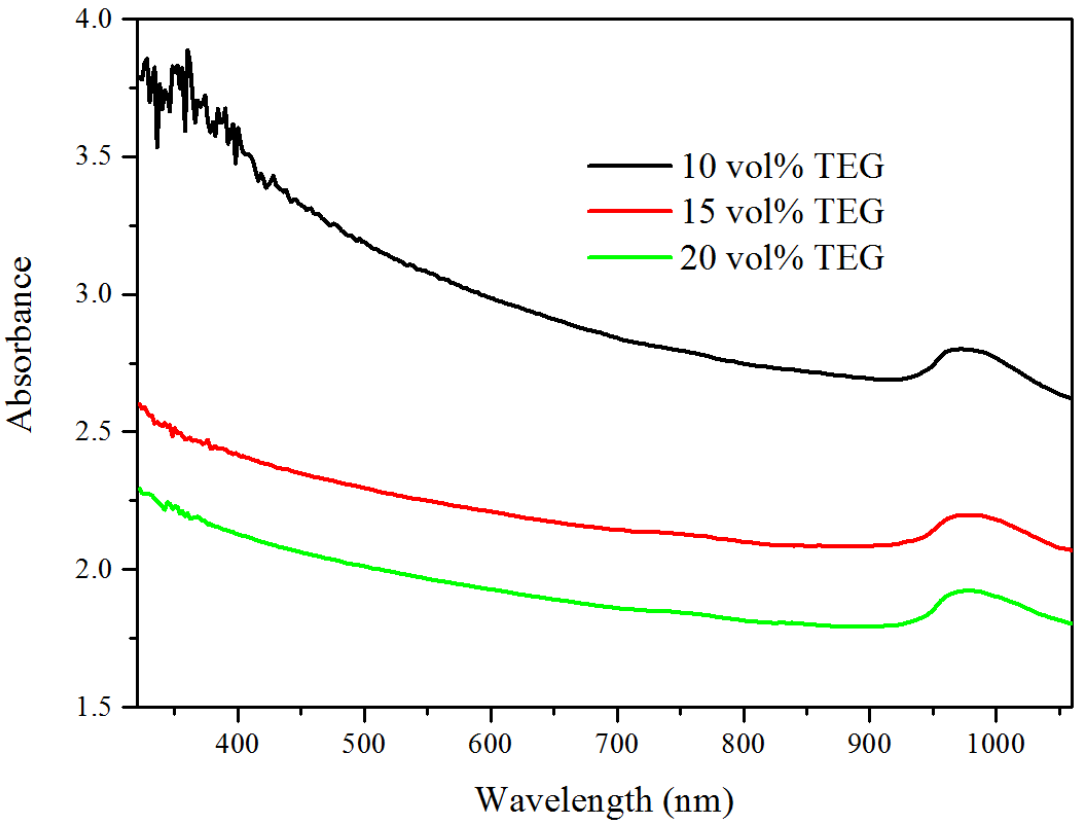

Figure 6. 8 Optical absorbance spectra of novel draw solutions samples having various TEG volume concentrations with only 0.05 wt% K/CNF concentration

Fig. 6.9 shows the temperature variation in 1M NaCl solution sample and **Fig. 6.10** shows the temperature change in NDS sample containing only 0.2 wt% solar absorptive K/CNF and 10 vol% TEG, when exposed to radiation flux for 20 min. It could be seen that the temperature distribution was almost uniform along the optical depth of the salt solution sample (**Fig. 6.9**). Most of the radiation flux passed through the sample volume due to its very poor solar absorption and transparent nature.

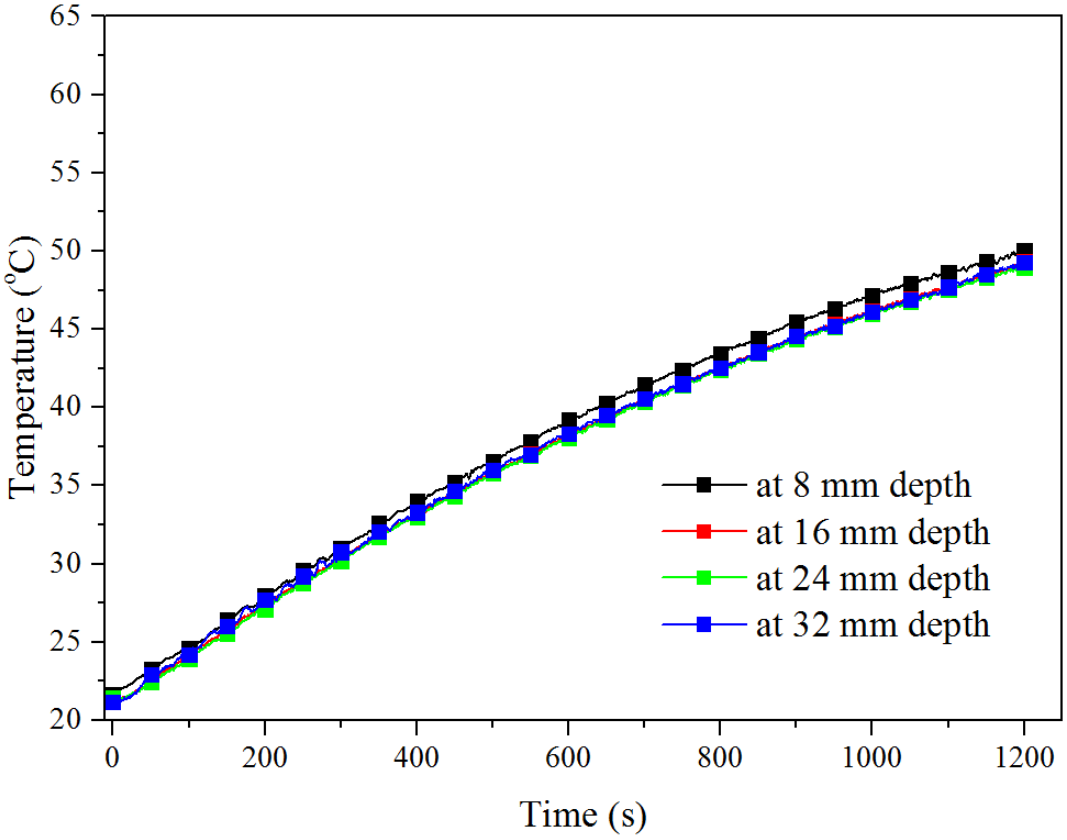

Figure 6. 9 Change in temperature of 1M NaCl solution sample along the optical depth when radiated under a flux of 10 suns

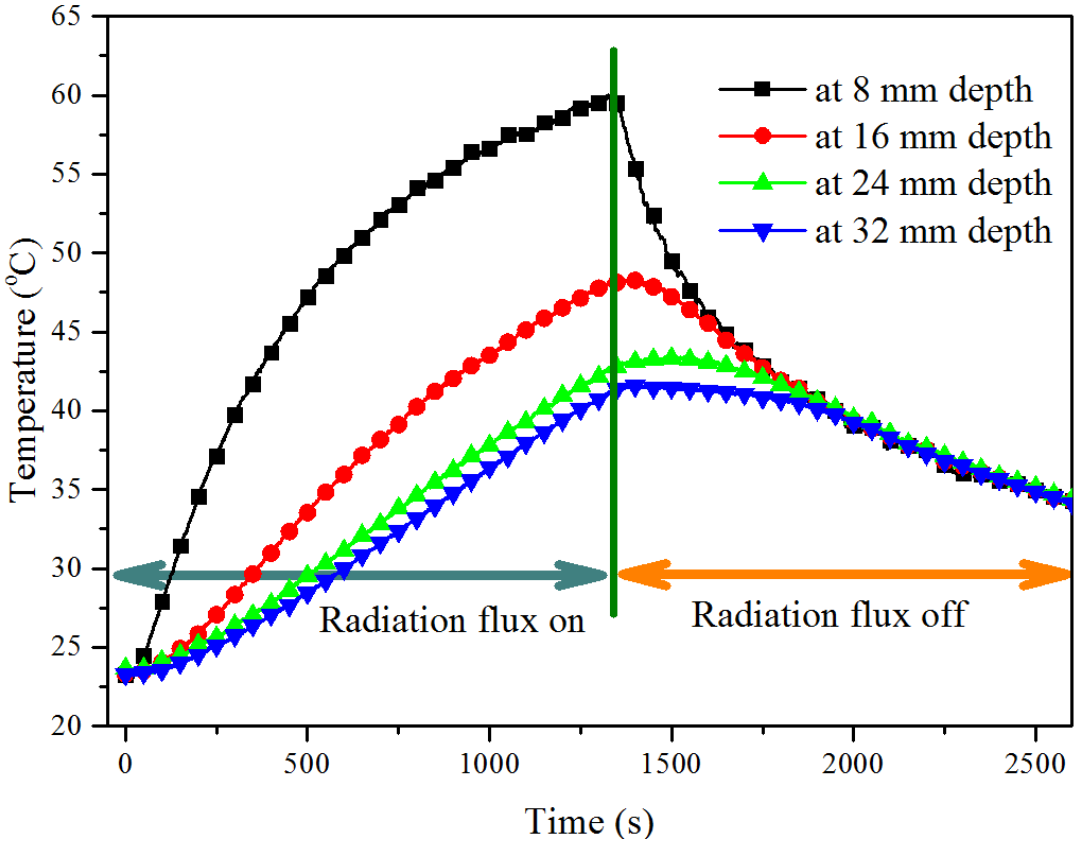

Figure 6. 10 Temperature distribution along the optical depth of NDS with 0.2 wt% in 10 vol% TEG when irradiated for 20 min under 10 suns

Whereas, there was a clear non-uniform temperature distribution in case of NDS sample and the rate of rise in temperature at a depth 8 mm (surface temperature) was much higher than that of lower depths (**Fig. 6.10**). The clear non-uniform temperature distribution along the optical depth of NDS sample showed that most of the radiation energy was absorbed at the surface due to highly absorptive nature of the sample.

The water flux based on the change in mass of the samples over the irradiation time, calculated using Eq. 6.1 is given in **Fig. 6.11**. With salt solution sample, a water flux of even less than 1.0 LMH was achieved because water and salt contents had poor solar absorption capability and the radiations passed through the sample volume due

to their transparent nature, thereby increasing the temperature very slowly from the bottom. On the other hand, the water flux ranges in three to four folds in case of NDS with concentrations in the experimental domain of this work as compared to 1M NaCl solution as presented in **Fig. 6.11**.

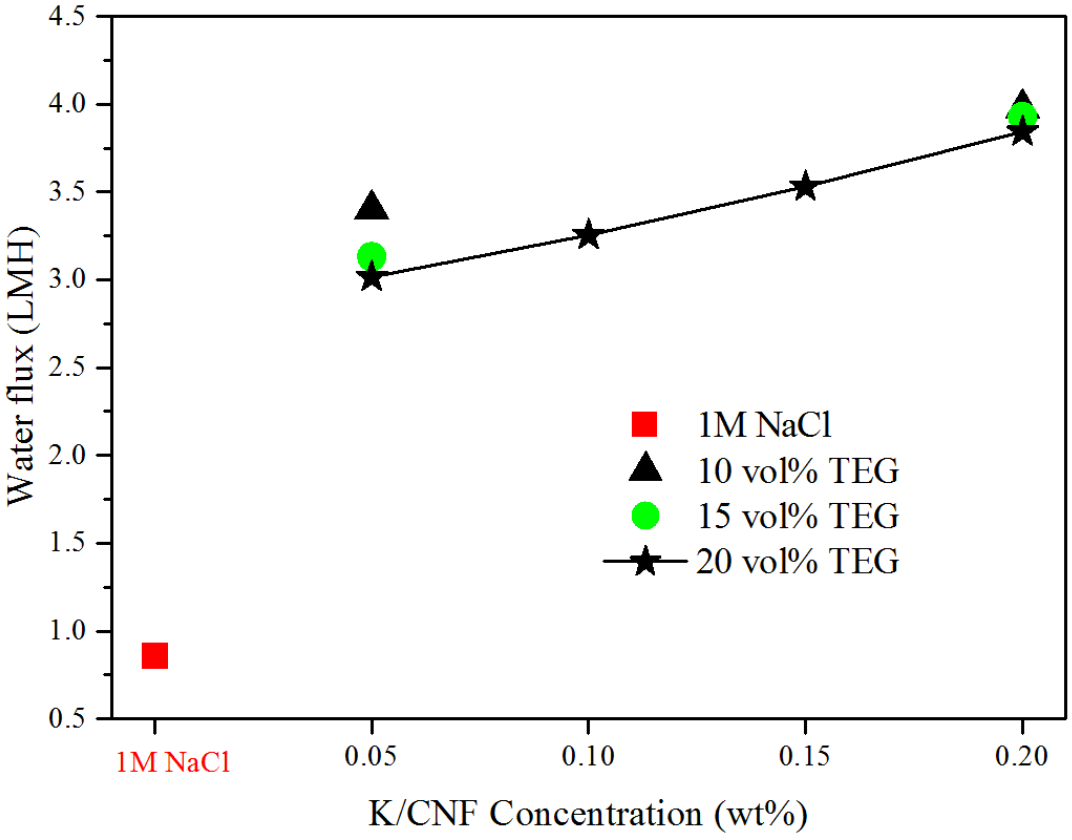

Figure 6. 11 Water flux of NDS with various concentrations of K/CNF and TEG in the regeneration phase of FO process

The water flux increases linearly with the concentration of K/CNF for a given volume concentration of TEG. For example, for 20 vol% of TEG, water flux increased from 3.02 to 3.84 LMH when the K/CNF concentration was increased from 0.05 to 0.2 wt% respectively. This enhancement was associated with increased photo absorptivity of the NDS sample with K/CNF concentration. The radiations were absorbed at the

surface layer thereby increasing the temperature (**Fig. 6.10**) and resulting in more and more evaporation from the surface liquid layer. With the increase in K/CNF concentration, the ability to absorb radiation flux was increased which resulted in higher evaporation of the liquid from the top surface for a given TEG volume concentration.

However, the vapour generation and thus the water flux was slightly reduced when TEG concentration was increased from 10 vol% to 20 vol% for a given K/CNF concentration. For 0.05 wt% concentration of K/CNF, the water flux was slightly decreased from 3.40 to 3.02 LMH when TEG concentration was increased from 10 to 20 vol% respectively. This slight decline in water flux was associated with a relatively lowered water potential with increased TEG concentration in the solution.

In addition to temperature distribution and water flux, photothermal performance was also analysed in terms of photothermal conversion efficiency (PTE) and its enhancement over 1 M NaCl solution. **Fig. 6.12** shows the photothermal efficiency and **Fig. 6.13** presents the PTE enhancement. PTE was calculated using the same modified method (Eq. 5.3) as given in Section 5.3.2 of Chapter 5.

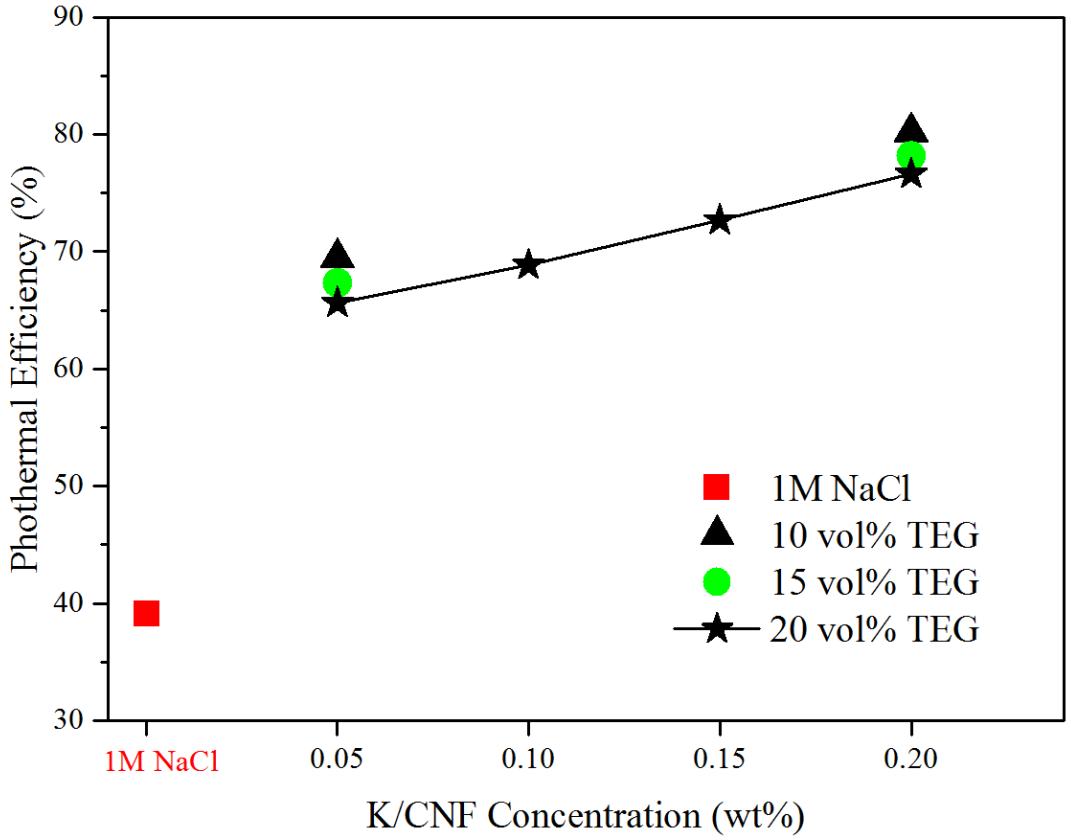

Figure 6. 12 Photothermal efficiency of NDS at various concentrations of K/CNF and TEG as a result of exposure to radiation flux of 10 suns for 20 min

PTE includes both the components of heat i.e. sensible heat as well as latent heat absorbed by the sample during the irradiation time. PTE for 1 M NaCl sample was observed to be 39% while it was related almost linearly with the K/CNF concentration for a given volume concentration of TEG in case of NDS. PTE was increased from 65% to 77% when the K/CNF concentration was increased from 0.05 to 0.20 wt% with 20 vol% TEG concentration.

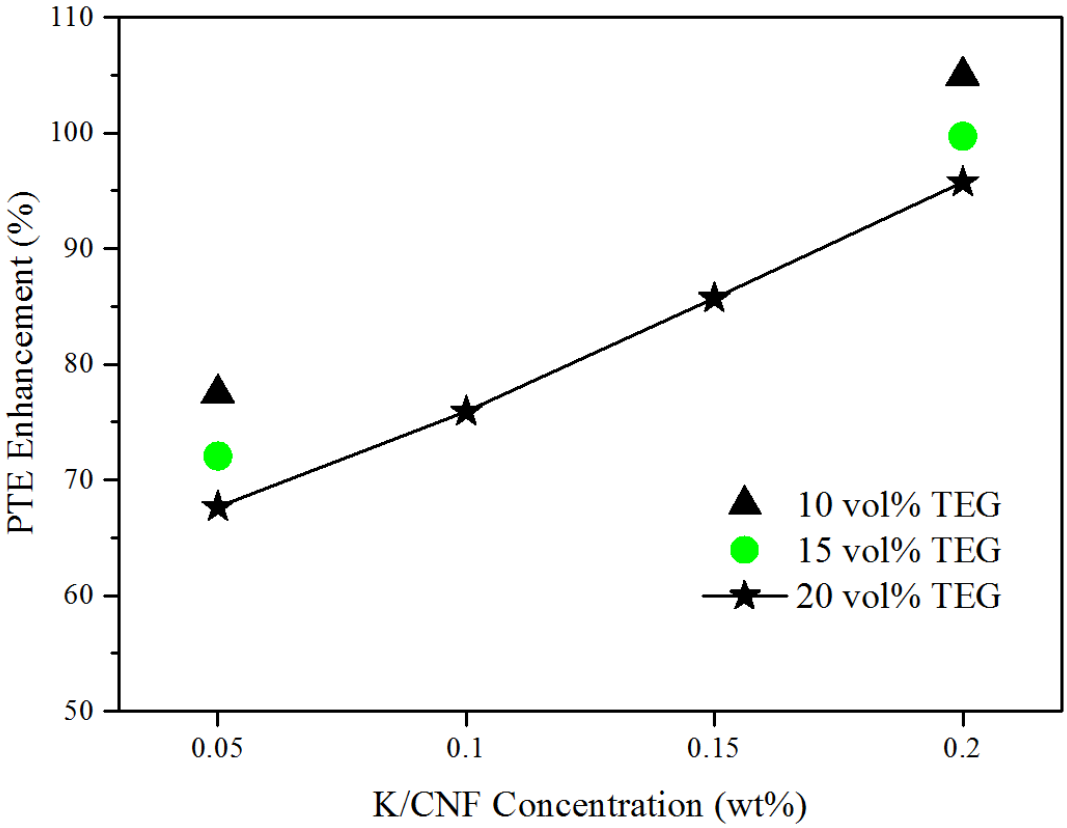

Figure 6. 13 Enhancement in photothermal efficiency of NDS

This increase in PTE was associated with enhanced solar absorption capability of the sample with increased K/CNF concentration. In addition, the extinction effect of the sample was also increased meaning the colour became darker with increased K/CNF concentration and thus most of the radiations were absorbed instead of passing through the sample as in case of salt solution.

However, PTE was slightly decreased with an increase in the concentration of TEG for a given K/CNF concentration. Photothermal efficiency was decreased from 69 to 65% when the TEG concentration was increased from 10 to 20 vol% respectively with 0.05 wt% K/CNF concentration. Similarly with 0.20 wt% K/CNF, PTE decreased from 80 to 76% when TEG concentration was increased from 10 to 20 vol% as given

in **Fig. 6.12**. The reason of a slight decrease in PTE with increasing TEG concentration was thought of the decrease in water contents and also the coverage of K/CNF surface in the presence of TEG which can also be verified from the optical absorbance spectra of samples having different TEG concentrations with same K/CNF concentration as given in **Fig. 6.8**. Furthermore, the boiling temperature of TEG is almost three times higher that of water, so more energy is required to detach water molecules from TEG molecules. The increasing concentration of TEG in the mixture definitely increased water flux in FO phase but it had a little negative effect in the regeneration phase of FO process.

The enhancement in PTE is given in **Fig. 6.13** which is a further and easy elaboration of the effect of K/CNF and TEG concentrations on the photothermal performance of NDS in regeneration phase of FO process. Compared with 1M salt solution, an enhancement of 105% was observed with 0.20 wt% K/CNF in 10 vol% TEG. The osmotic pressure and thus water permeation flux was amplified with increased concentration of both K/CNF and TEG in the first phase of FO process. However, the higher concentration of TEG slightly suppressed the photothermal performance of NDS in the second phase i.e. regeneration.

6.3.4 Quality analysis of product water

The quality of the product water was analysed by measuring the pH, total dissolved solids (TDS) and turbidity. The absorbance and transmittance spectra from UV-Vis spectrometer and FTIR respectively were also compared to see any difference between DI water and product water and to examine the presence of TEG and/or K/CNF traces. The pH and TDS [188] of the product water were 6.2 and 22 mg/L

which were within the acceptable range prescribed by WHO [189]. The Turbiscan spectra for transmission and backscattering of the product water sample and DI water were overlapping as shown in **Fig. 6.14**, showing the same turbidity.

Fig. 6.15 (a) shows the FTIR spectra of the product water sample and DI water which were overlapping showing the absence of any TEG in the product water. Similarly **Fig. 6.15 (b)** shows the UV-Vis spectra of the product water and DI water samples which were again the same showing that the product was not containing any of K/CNF or TEG traces.

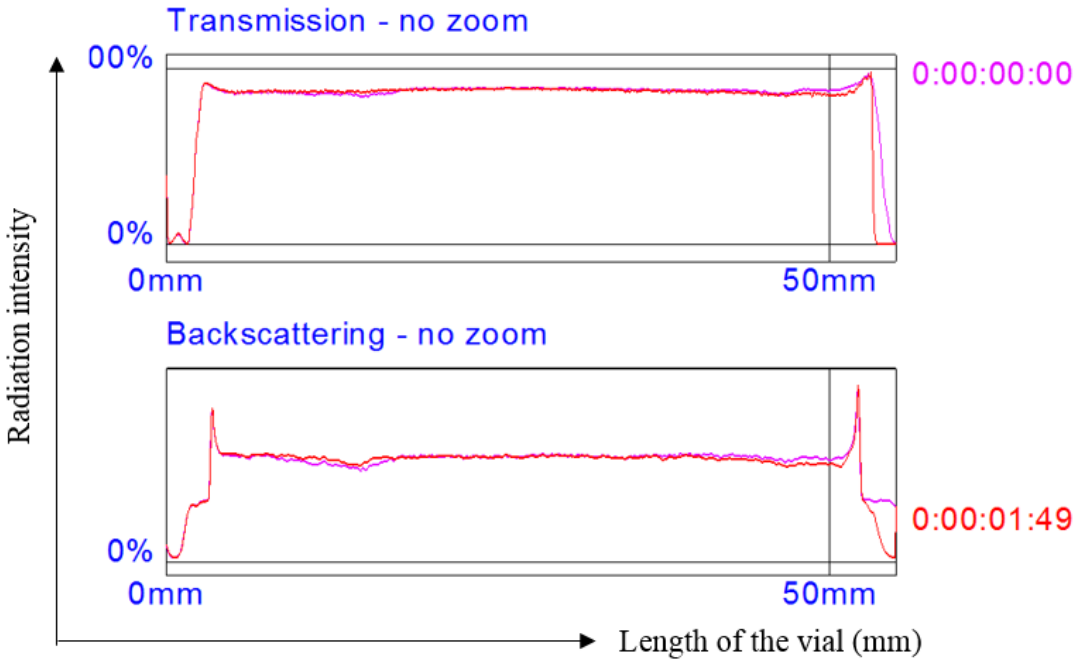

Figure 6. 14 Transmission and backscattering spectra of deionized water and the product water from Turbiscan

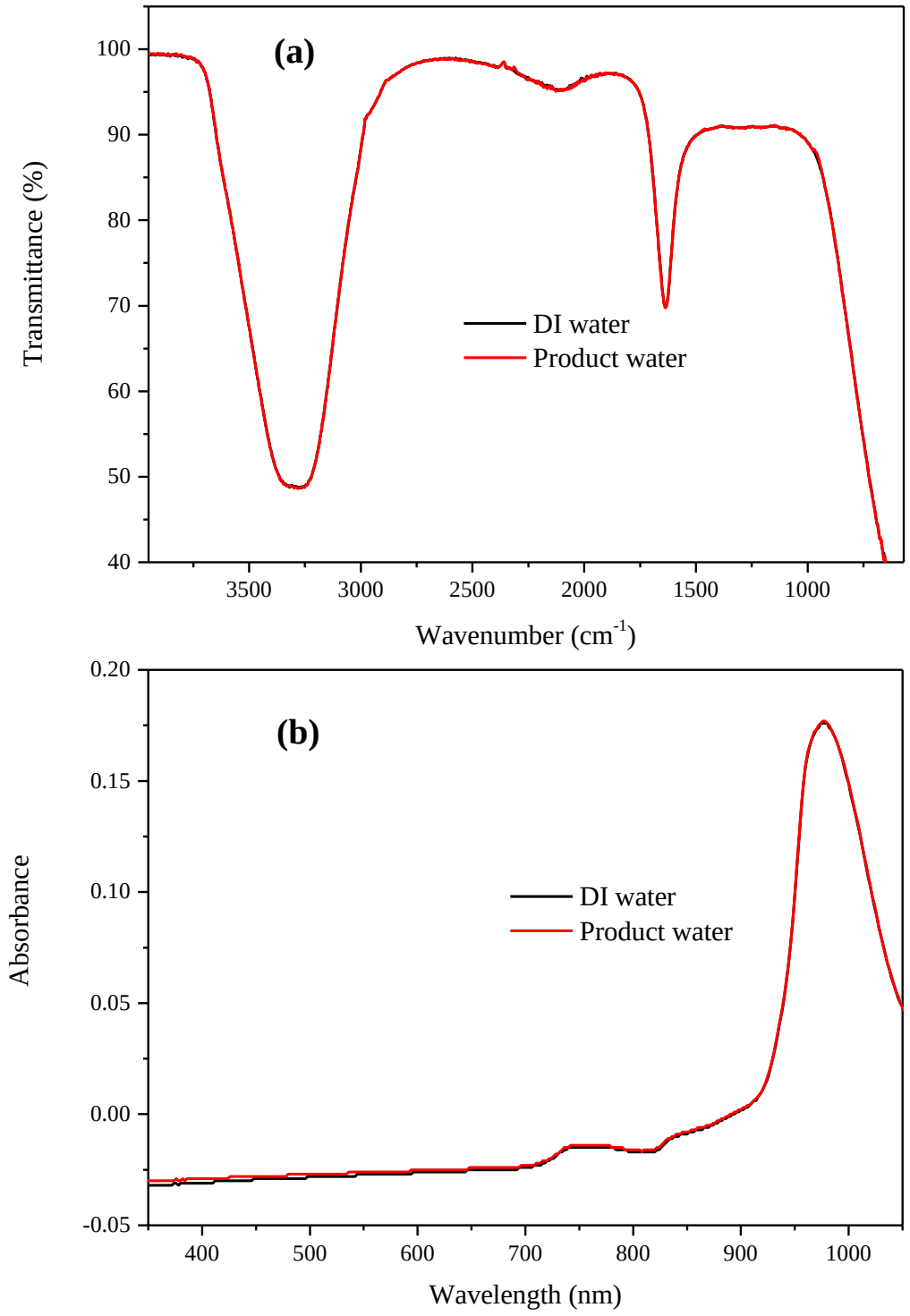

Figure 6. 15 Spectra of the product water and DI water from (a) FTIR and (b) UV-VIS spectrometer

6.4 Chapter summary

Novel draw solutions with very good stability, high osmotic pressure, negligible reverse solute flux and high photo absorption were used to evaluate their FO performance and product water separation based on direct solar absorption. Osmolality, water flux and reverse solute flux of the NDS with K/CNF and TEG concentration range from 0.05 to 0.20 wt% and 10 to 20 vol%, respectively were evaluated using a laboratory scale FO test cell. The FO performance of the NDS was directly related with the concentrations of K/CNF and TEG. An osmotic pressure of 70.3 bar was developed with a concentration of 0.20 wt% and 20 vol% of K/CNF and TEG, respectively thereby developing water flux of 13.3 LMH which was 80% higher than that of 1M salt solution. The specific solute flux of 1M salt solution was 0.56 g/L while it was only 0.031 g/L for the maximum concentration of TEG-K/CNF in the NDS which was negligibly small. There was a clear non-uniform temperature distribution along the optical depth of the NDS sample due to its high photo absorptivity and an enhancement of 105% was observed in the photothermal efficiency as compared to salt solution. The quality of the product water was analysed using different water tests and the results were in the acceptable range of potable water as prescribed in guidelines for drinking water quality.by WHO. The consistent FO performance, enhanced direct solar absorption and quality analysis of product water proved the nanofluid based novel draw solutions a potential candidate for solar desalination based on forward osmosis process.

Chapter 7

Conclusions and Future Work

7.1 Conclusions

The ever increasing world population and industrialization causing the sources of drinking water polluted and scarce and a number water treatment technologies have been developed to augment the supply of potable water and are being modified to use renewable energy. Forward osmosis (FO) is an emerging technique for water treatment and has many advantages over the existing technologies including minimum and reversible membrane fouling, high salt rejection rate, low energy intensity, no hydraulic pressure, etc. With a significant advancement on membrane side, one of the major limitations of FO to its commercialization is the availability of proper draw solutions which provide sufficient osmotic pressure to transport water across the membrane and their easy and efficient regeneration.

This work presents a novel concept of purposely synthesized novel nanofluids having two unique functions i.e. to absorb the solar energy efficiently and directly and to enhance the osmotic pressure for FO water desalination. Photothermal performance of various nanofluids was investigated experimentally in terms of direct absorption and direct steam generation and the most absorptive one was examined for FO performance. The capability of nanofluids to directly absorb solar energy efficiently for volumetric heating and to produce steam was investigated in terms of optical absorbance, change in bulk fluid temperature, photothermal efficiency and specific absorption rate. The FO performance of direct absorptive nanofluid based novel draw solutions was checked in terms of osmotic pressure, water permeation flux and reverse solute flux. The quality of product water was analysed in terms of presence of any nanoparticle entrained through various water quality tests and the results were

compared with potable water quality guidelines prescribed by WHO. The conclusions can be summarized as follows;

1. Several direct absorption nanofluids were formulated and characterized in terms of their morphological appearance, structural behaviour and elemental composition. These characterized nanofluids were experimented to analyse their performance in terms of direct volumetric bulk fluid heating, absorption at micro droplet level and ability to generate steam efficiently.
2. At bulk scale, the direct absorptive nanofluids of gold, silver and carbon nanofibers exhibited a photothermal efficiency enhancement of about 95%, 100% and 105% respectively over the basefluid due their high absorptivity while silicon/silver hybrid nanofluid enhanced the evaporation rate by 55.5% at micro droplet scale.
3. A highly non-uniform temperature distribution was observed along the optical depth of the gold and carbon nanofiber nanofluid samples. A novel integration method was proposed to calculate the sensible heating contribution in the photothermal efficiency calculation.
4. Steam generation based photothermal efficiency was increased almost linearly with the nanoparticle concentration. The analysis of the condensed vapour proved the absence of any nanoparticle, suggesting that the nanoparticles were not entrained by the vapour even under vigorous boiling, thus proving a safe method to produce potable water in arid areas with abundant solar energy.
7. The potential of direct solar absorptive nanofluids as novel draw solutions for forward osmosis desalination was investigated experimentally for the first time of its kind and evaluated in terms of enhanced osmotic pressure, water

flux, reverse solute flux and solar absorption for the regeneration of draw solution.

8. The highly absorptive carbon nanofibers based nanofluid was surface functionalized with potassium and mixed with triethylene glycol to augment the osmotic pressure by enhancing its hydrophilicity. The novel draw solution being rich in osmotically active species, exhibited an osmotic pressure of 70.3 bar and water flux of 13.3 LMH (almost 80% higher than that of 1M NaCl solution) when deionized water was used as feed solution. The specific solute flux was 0.031 g/L only which was negligibly small as compared to 1M NaCl as draw solution. Moreover, the performance of novel DS was consistent over multiple runs which showed its potential for long term FO operation.
9. The regeneration of novel draw solution was accomplished by irradiating it with a simulated solar flux and condensing the vapours as potable water. The quality of the product water was analysed and the values of pH and TDS were within the acceptable range of potable water guidelines given by WHO and the exactly overlapping spectra of turbidity, FTIR and UV/Vis for the product water and deionized water proved the absence of any nanoparticle or polymer traces in the product water.

The experimental results stated above proved that direct solar absorptive nanofluids as novel draw solutions not only enhanced the photothermal performance significantly but also developed osmotic pressure sufficiently to permeate water across the FO membrane. Moreover, the quality of product water being within the permissible range of potable water guidelines and the absence of nanoparticles in the product water

proved these direct absorptive nanofluid based novel draw solutions a potential candidate for future FO solar water desalination in arid areas.

7.2 Recommendations for future work

Direct solar absorptive nanofluids were first time coupled with FO desalination as novel draw solutions for enhanced osmotic pressure and renewable energy based regeneration. Photothermal conversion performance of the various nanofluids was investigated experimentally and their potential as a novel draw solution was evaluated in terms of high osmotic pressure. The results of this experimental work proved that nanofluid based direct solar absorptive draw solutions are a viable potential alternative to the conventional FO draw solution whose regeneration and product water recovery is very complex and difficult. However, to explore this field further, following are the recommendations for possible future work;

1. Photothermal performance and FO performance of the novel draw solutions was evaluated separately. In future work, these two separate phases should be integrated together and water flux in FO phase and that in regeneration phase can be balanced by process intensification.
2. Osmotic pressure and photo absorption capabilities of the nanofluids being used as draw solutions must be augmented for high performance in FO desalination. Two or more than two types of nanoparticles, one having high osmotic activity like iron nanoparticles and the others having high solar absorptivity e.g K/CNF, CNT, graphene oxide, plasmonic nanoparticles, etc. can be composited with polymers for this augmented performance.

3. In draw solution regeneration phase, the solar energy should be absorbed by the surface liquid layer and the heat leakage to the downstream liquid layers should be minimum to have high photothermal efficiency. For this purpose, a nanofluid based membrane can be developed which is highly solar absorptive and allows minimum heat leakage to the bulk liquid for an increased surface evaporation and thus water flux at the second phase of the FO desalination process.
4. A simulation model can be developed to evaluate the osmotic pressure, water permeation flux and reverse solute flux of the draw solutions based on nanofluids in future work which will be very helpful in evaluating different nanofluids already proved to be highly photo absorptive.

List of References

1. El-Dessouky, H.T. and H.M. Ettouney, Chapter 1 - Introduction, in Fundamentals of Salt Water Desalination, H.T. El-Dessouky and H.M. Ettouney, Editors. 2002, Elsevier Science B.V.: Amsterdam. p. 1-17.
2. Wang, Y.-N., K. Goh, X. Li, L. Setiawan, and R. Wang, Membranes and processes for forward osmosis-based desalination: Recent advances and future prospects. Desalination, 2017.
3. Li, C., Y. Goswami, and E. Stefanakos, Solar assisted sea water desalination: A review. Renewable and Sustainable Energy Reviews, 2013. 19: p. 136-163.
4. Balch, O., Is solar-powered desalination answer to water independence for California? The Guradian 2014.
5. Cath, T.Y., A.E. Childress, and M. Elimelech, Forward osmosis: Principles, applications, and recent developments. Journal of Membrane Science, 2006. 281(1–2): p. 70-87.
6. Manickam, S.S. and J.R. McCutcheon, Understanding mass transfer through asymmetric membranes during forward osmosis: A historical perspective and critical review on measuring structural parameter with semi-empirical models and characterization approaches. Desalination, 2017. 421(Supplement C): p. 110-126.
7. What's so special about the nanoscale? accessed on 4 January, 2018; Available from: https://www.nano.gov/nanotech-101/special.

8. Loeb, S., C. Li, and J.-H. Kim, Solar Photothermal Disinfection using Broadband-Light Absorbing Gold Nanoparticles and Carbon Black. Environmental Science & Technology, 2018. 52(1): p. 205-213.

9. Gupta, H.K., G.D. Agrawal, and J. Mathur, An experimental investigation of a low temperature Al_2O_3-H_2O nanofluid based direct absorption solar collector. Solar Energy, 2015. 118(Supplement C): p. 390-396.

10. Otanicar, T.P., P.E. Phelan, and J.S. Golden, Optical properties of liquids for direct absorption solar thermal energy systems. Solar Energy, 2009. 83(7): p. 969-977.

11. Gupta, H.K., G.D. Agrawal, and J. Mathur, An experimental investigation of a low temperature Al_2O_3-H_2O nanofluid based direct absorption solar collector. Solar Energy, 2015. 118: p. 390-396.

12. Said, Z., M.A. Sabiha, R. Saidur, A. Hepbasli, N.A. Rahim, S. Mekhilef, and T.A. Ward, Performance enhancement of a Flat Plate Solar collector using Titanium dioxide nanofluid and Polyethylene Glycol dispersant. Journal of Cleaner Production, 2015. 92: p. 343-353.

13. Sokhansefat, T., A.B. Kasaeian, and F. Kowsary, Heat transfer enhancement in parabolic trough collector tube using Al_2O_3/synthetic oil nanofluid. Renewable and Sustainable Energy Reviews, 2014. 33: p. 636-644.

14. Salavati Meibodi, S., A. Kianifar, H. Niazmand, O. Mahian, and S. Wongwises, Experimental investigation on the thermal efficiency and performance characteristics of a flat plate solar collector using SiO_2/EG–water nanofluids. International Communications in Heat and Mass Transfer, 2015. 65: p. 71-75.

15. Liu, J., Z. Ye, L. Zhang, X. Fang, and Z. Zhang, A combined numerical and experimental study on graphene/ionic liquid nanofluid based direct absorption solar collector. Solar Energy Materials and Solar Cells, 2015. 136: p. 177-186.

16. Minardi, J.E. and H.N. Chuang, Performance of a “black” liquid flat-plate solar collector. Solar Energy, 1975. 17(3): p. 179-183.

17. Chen, M., Y. He, J. Zhu, Y. Shuai, B. Jiang, and Y. Huang, An experimental investigation on sunlight absorption characteristics of silver nanofluids. Solar Energy, 2015. 115: p. 85-94.

18. Luo, Z., C. Wang, W. Wei, G. Xiao, and M. Ni, Performance improvement of a nanofluid solar collector based on direct absorption collection (DAC) concepts. International Journal of Heat and Mass Transfer, 2014. 75: p. 262-271.

19. Mahian, O., A. Kianifar, S.A. Kalogirou, I. Pop, and S. Wongwises, A review of the applications of nanofluids in solar energy. International Journal of Heat and Mass Transfer, 2013. 57(2): p. 582-594.

20. Lee, B.J., K. Park, T. Walsh, and L. Xu, Radiative Heat Transfer Analysis in Plasmonic Nanofluids for Direct Solar Thermal Absorption. Journal of Solar Energy Engineering, 2012. 134(2): p. 021009.

21. Zhang, H., H.-J. Chen, X. Du, and D. Wen, Photothermal conversion characteristics of gold nanoparticle dispersions. Solar Energy, 2014. 100: p. 141-147.

22. Bandarra Filho, E.P., O.S.H. Mendoza, C.L.L. Beicker, A. Menezes, and D. Wen, Experimental investigation of a silver nanoparticle-based direct

absorption solar thermal system. Energy Conversion and Management, 2014. 84: p. 261-267.

23. Yousefi, T., F. Veysi, E. Shojaeizadeh, and S. Zinadini, An experimental investigation on the effect of Al_2O_3–H_2O nanofluid on the efficiency of flat-plate solar collectors. Renewable Energy, 2012. 39(1): p. 293-298.

24. Verma, V. and L. Kundan, Thermal Performance Evaluation of a Direct Absorption Flat Plate Solar Collector (DASC) using Al_2O_3-H_2O Based Nanofluids. IOSR Journal of Mechanical and Civil Engineering (IOSR-JMCE), 2013. 6(2): p. 29-35.

25. Said, Z., M.H. Sajid, M.A. Alim, R. Saidur, and N.A. Rahim, Experimental investigation of the thermophysical properties of Al_2O_3-nanofluid and its effect on a flat plate solar collector. International Communications in Heat and Mass Transfer, 2013. 48: p. 99-107.

26. Otanicar, T.P., P.E. Phelan, R.S. Prasher, G. Rosengarten, and R.A. Taylor, Nanofluid-based direct absorption solar collector. Journal of Renewable and Sustainable Energy, 2010. 2(3): p. 033102.

27. Zhang, L., J. Liu, G. He, Z. Ye, X. Fang, and Z. Zhang, Radiative properties of ionic liquid-based nanofluids for medium-to-high-temperature direct absorption solar collectors. Solar Energy Materials and Solar Cells, 2014. 130: p. 521-528.

28. Said, Z., M.A. Sabiha, R. Saidur, A. Hepbasli, N.A. Rahim, S. Mekhilef, and T.A. Ward, Performance enhancement of a Flat Plate Solar collector using TiO_2 nanofluid and Polyethylene Glycol dispersant. Journal of Cleaner Production, 2015.

29. Wu, J., R. Wang, H. Yu, G. Li, K. Xu, N.C. Tien, R.C. Roberts, and D. Li, Inkjet-printed microelectrodes on PDMS as biosensors for functionalized microfluidic systems. Lab on a Chip - Miniaturisation for Chemistry and Biology, 2015. 15(3): p. 690-695.

30. Choi, Y., J. Han, and C. Kim, Pattern formation in drying of particle-laden sessile drops of polymer solutions on solid substrates. Korean Journal of Chemical Engineering, 2011. 28(11): p. 2130-2136.

31. Grouchko, M., A. Kamyshny, and S. Magdassi, Formation of air-stable copper–silver core–shell nanoparticles for inkjet printing. Journal of Materials Chemistry, 2009. 19(19): p. 3057-3062.

32. Calvert, P., Inkjet printing for materials and devices. Chemistry of Materials, 2001. 13(10): p. 3299-3305.

33. Sefiane, K., On the Formation of Regular Patterns from Drying Droplets and Their Potential Use for Bio-Medical Applications. Journal of Bionic Engineering, 2010. 7, Supplement: p. S82-S93.

34. Sobac, B. and D. Brutin, Desiccation of a sessile drop of blood: Cracks, folds formation and delamination. Colloids and Surfaces A: Physicochemical and Engineering Aspects, 2014. 448: p. 34-44.

35. Fang, X., B. Li, E. Petersen, Y.S. Seo, V.A. Samuilov, Y. Chen, J.C. Sokolov, C.Y. Shew, and M.H. Rafailovich, Drying of DNA droplets. Langmuir, 2006. 22(14): p. 6308-6312.

36. Majumder, M., C.S. Rendall, J.A. Eukel, J.Y. Wang, N. Behabtu, C.L. Pint, T.Y. Liu, A.W. Orbaek, F. Mirri, J. Nam, A.R. Barron, R.H. Hauge, H.K. Schmidt, and M. Pasquali, Overcoming the "coffee-stain" effect by

compositional Marangoni-flow-assisted drop-drying. J Phys Chem B, 2012. 116(22): p. 6536-42.

37. Ward, C.A. and F. Duan, Turbulent transition of thermocapillary flow induced by water evaporation. Physical Review E, 2004. 69(5): p. 056308.

38. Zhong, X. and F. Duan, Flow regime and deposition pattern of evaporating binary mixture droplet suspended with particles. The European Physical Journal E, 2016. 39(2): p. 1-6.

39. Park, C.-S., H. Kim, and H.-C. Lim, Study of internal flow and evaporation characteristics inside a water droplet on a vertically vibrating hydrophobic surface. Experimental Thermal and Fluid Science, 2016. 78: p. 112-123.

40. Sempels, W., R. De Dier, H. Mizuno, J. Hofkens, and J. Vermant, Auto-production of biosurfactants reverses the coffee ring effect in a bacterial system. Nat Commun, 2013. 4: p. 1757.

41. Deegan, R.D., O. Bakajin, T.F. Dupont, G. Huber, S.R. Nagel, and T.A. Witten, Capillary flow as the cause of ring stains from dried liquid drops. Nature, 1997. 389(6653): p. 827-829.

42. Uchiyama, H., D. Shimaoka, and H. Kozuka, Spontaneous pattern formation based on the coffee-ring effect for organic-inorganic hybrid films prepared by dip-coating: effects of temperature during deposition. Soft Matter, 2012. 8(44): p. 11318-11322.

43. Hu, H. and R.G. Larson, Marangoni Effect Reverses Coffee-Ring Depositions. The Journal of Physical Chemistry B, 2006. 110(14): p. 7090-7094.

44. Gan, Y. and L. Qiao, Radiation-enhanced evaporation of ethanol fuel containing suspended metal nanoparticles. International Journal of Heat and Mass Transfer, 2012. 55(21–22): p. 5777-5782.

45. Chen, R.-H., T.X. Phuoc, and D. Martello, Effects of nanoparticles on nanofluid droplet evaporation. International Journal of Heat and Mass Transfer, 2010. 53(19–20): p. 3677-3682.

46. Sefiane, K. and R. Bennacer, Nanofluids droplets evaporation kinetics and wetting dynamics on rough heated substrates. Advances in Colloid and Interface Science, 2009. 147–148: p. 263-271.

47. Cui, L., J. Zhang, X. Zhang, Y. Li, Z. Wang, H. Gao, T. Wang, S. Zhu, H. Yu, and B. Yang, Avoiding coffee ring structure based on hydrophobic silicon pillar arrays during single-drop evaporation. Soft Matter, 2012. 8(40): p. 10448-10456.

48. Dou, R. and B. Derby, Formation of coffee stains on porous surfaces. Langmuir, 2012. 28(12): p. 5331-8.

49. Xiao, C., L. Zhou, Z. Sun, X. Du, and Y. Yang, Near-wall fluid flow near the pinned contact line during droplet evaporation. Experimental Thermal and Fluid Science, 2016. 72: p. 210-217.

50. Chen, C.-T., F.-G. Tseng, and C.-C. Chieng, Evaporation evolution of volatile liquid droplets in nanoliter wells. Sensors and Actuators A: Physical, 2006. 130–131: p. 12-19.

51. Van Nguyen Truskett, K.J.S., Influence of Surfactants on an Evaporating Drop:

Fluorescence Images and Particle Deposition Patterns. Langmuir, 2003. 19: p. 8271-8279.

52. Leonid V. Govor, G.H.B., Gu¨ nter Reiter, Elena Shevchenko, Horst Weller, and Ju¨ rgen Parisi, Self-Assembly of $CoPt_3$ Nanoparticle Rings Based on Phase-Separated Hexadecylamine Droplet Structure. Langmuir, 2003. 19: p. 9573-9576.

53. Still, T., P.J. Yunker, and A.G. Yodh, Surfactant-Induced Marangoni Eddies Alter the Coffee-Rings of Evaporating Colloidal Drops. Langmuir, 2012. 28(11): p. 4984-4988.

54. Gan, Y. and L. Qiao, Evaporation characteristics of fuel droplets with the addition of nanoparticles under natural and forced convections. International Journal of Heat and Mass Transfer, 2011. 54(23–24): p. 4913-4922.

55. Wei, Y., W. Deng, and R.-H. Chen, Effects of insoluble nano-particles on nanofluid droplet evaporation. International Journal of Heat and Mass Transfer, 2016. 97: p. 725-734.

56. Gan, Y. and L. Qiao, Optical Properties and Radiation-Enhanced Evaporation of Nanofluid Fuels Containing Carbon-Based Nanostructures. Energy & Fuels, 2012. 26(7): p. 4224-4230.

57. Andreea, T. and M.G. A., Total Internal Reflection Fluorescence (TIRF) Microscopy. Current Protocols in Microbiology, 2017. 10(1): p. 2A.2.1-2A.2.22.

58. Sun, Z., L. Zhou, C. Xiao, X. Du, and Y. Yang, Nanoparticle motion and deposition near the triple line in evaporating sessile water droplet on a

superhydrophilic substrate. Experimental Thermal and Fluid Science, 2016. 76: p. 67-74.

59. Jung, J.Y., Y.W. Kim, J.Y. Yoo, J. Koo, and Y.T. Kang, Forces acting on a single particle in an evaporating sessile droplet on a hydrophilic surface. Analytical Chemistry, 2010. 82(3): p. 784-788.

60. Franken, M.J.Z., C. Poelma, and J. Westerweel, Nanoscale contact line visualization based on total internal reflection fluorescence microscopy. Optics Express, 2013. 21(22): p. 26093-26102.

61. Zettner, C.M. and M. Yoda, Particle velocity field measurements in a near-wall flow using evanescent wave illumination. Experiments in Fluids, 2003. 34(1): p. 115-121.

62. Li, H., R. Sadr, and M. Yoda, Multilayer nano-particle image velocimetry. Experiments in Fluids, 2006. 41(2): p. 185-194.

63. Li, Q., J. Song, H. Yu, Z. Li, X. Pan, and B. Yang, Investigating the microstructures and surface features of seawater RO membranes and the dependencies of fouling resistance performances. Desalination, 2014. 352: p. 109-117.

64. Weerasekara, N.A. and K.-H. Choo, Synergistic combination of metal oxide adsorbents for enhanced fouling control and metal removal in a submerged membrane adsorber. Journal of Membrane Science, 2015. 490: p. 9-17.

65. Wang, J., Z. Wang, J. Wang, and S. Wang, Improving the water flux and bio-fouling resistance of reverse osmosis (RO) membrane through surface modification by zwitterionic polymer. Journal of Membrane Science, 2015. 493: p. 188-199.

66. Taylor, L.L., The Many Disadvantages of Reverse Osmosis Water Treatment. http://bestwaterblog.drupalgardens.com/ro, accessed on 02 January 2018.

67. Darwish, M.A. and A. Alsairafi, Technical comparison between TVC/MEB and MSF. Desalination, 2004. 170(3): p. 223-239.

68. Posnansky, M., Technical and economical aspects of solar desalination with particular emphasis on solar pond powered distillation plants. Desalination, 1987. 67: p. 81-95.

69. El-Sebaii, A.A., A.A. Al-Ghamdi, F.S. Al-Hazmi, and A.S. Faidah, Thermal performance of a single basin solar still with PCM as a storage medium. Applied Energy, 2009. 86(7–8): p. 1187-1195.

70. Tabrizi, F.F. and A.Z. Sharak, Experimental study of an integrated basin solar still with a sandy heat reservoir. Desalination, 2010. 253(1–3): p. 195-199.

71. Zeroual, M., H. Bouguettaia, D. Bechki, S. Boughali, B. Bouchekima, and H. Mahcene, Experimental investigation on a double-slope solar still with partially cooled condenser in the region of Ouargla (Algeria). Energy Procedia, 2011. 6: p. 736-742.

72. Arunkumar, T., R. Jayaprakash, D. Denkenberger, A. Ahsan, M.S. Okundamiya, S. kumar, H. Tanaka, and H.Ş. Aybar, An experimental study on a hemispherical solar still. Desalination, 2012. 286: p. 342-348.

73. Omara, Z.M., M.A. Eltawil, and E.A. ElNashar, A new hybrid desalination system using wicks/solar still and evacuated solar water heater. Desalination, 2013. 325: p. 56-64.

74. Al Hawaj, O. and M.A. Darwish, A solar pond assisted multi-effect desalting system. Desalination, 1994. 99(1): p. 119-135.

75. Ophir, A. and F. Lokiec, Advanced MED process for most economical sea water desalination. Desalination, 2005. 182(1–3): p. 187-198.

76. Sommarva, C., Utilisation of power plant waste heat steams to enhance efficiency in thermal desalination. Desalination, 2008. 222(1–3): p. 592-595.

77. Alajlan, S.A. and M.S. Smiai, Performance and development of PV - plant for water pumping and desalination for remote area in Saudi Arabia. Renewable Energy, 1996. 8(1–4): p. 441-446.

78. Parida, B., S. Iniyan, and R. Goic, A review of solar photovoltaic technologies. Renewable and Sustainable Energy Reviews, 2011. 15(3): p. 1625-1636.

79. Agha, K.R., The thermal characteristics and economic analysis of a solar pond coupled low temperature multi stage desalination plant. Solar Energy, 2009. 83(4): p. 501-510.

80. Shaobo, H., Z. Zhang, Z. Huang, and A. Xie, Performance optimization of solar multi-stage flash desalination process using Pinch technology. Desalination, 2008. 220(1–3): p. 524-530.

81. Trieb, F. and H. Müller-Steinhagen, Concentrating solar power for seawater desalination in the Middle East and North Africa. Desalination, 2008. 220(1–3): p. 165-183.

82. IL García, J.Á., D Blanco, Performance model for parabolic trough solar thermal power plants with thermal storage: comparison to operating plant data. Solar Energy, 2011. 85( ): p. pp. 2443–2460.

83. de Gunzbourg, J. and D. Larger, Cogeneration applied to very high efficiency thermal seawater desalination plants. Desalination, 1999. 125(1–3): p. 203-208.

84. Amer, E.H., H. Kotb, G.H. Mostafa, and A.R. El-Ghalban, Theoretical and experimental investigation of humidification–dehumidification desalination unit. Desalination, 2009. 249(3): p. 949-959.

85. Abdel Dayem, A.M. and M. Fatouh, Experimental and numerical investigation of humidification/dehumidification solar water desalination systems. Desalination, 2009. 247(1–3): p. 594-609.

86. Yamalı, C. and İ. Solmus, A solar desalination system using humidification–dehumidification process: experimental study and comparison with the theoretical results. Desalination, 2008. 220(1–3): p. 538-551.

87. Saffarini, R.B., E.K. Summers, H.A. Arafat, and J.H. Lienhard V, Technical evaluation of stand-alone solar powered membrane distillation systems. Desalination, 2012. 286: p. 332-341.

88. S Al-Obaidani, E.C., F Macedonio, G Di Profio, H Al-Hinai, E Drioli, Potential of membrane distillation in seawater desalination: thermal efficiency, sensitivity study and cost estimation. Journal of Membrane Science, 2008. 323: p. 85–98.

89. Velmurugan, V. and K. Srithar, Prospects and scopes of solar pond: A detailed review. Renewable and Sustainable Energy Reviews, 2008. 12(8): p. 2253-2263.

90. Chekli, L., S. Phuntsho, H.K. Shon, S. Vigneswaran, J. Kandasamy, and A. Chanan, A review of draw solutes in forward osmosis process and their use in modern applications. Desalination and Water Treatment, 2012. 43(1-3): p. 167-184.

91. Akther, N., A. Sodiq, A. Giwa, S. Daer, H.A. Arafat, and S.W. Hasan, Recent advancements in forward osmosis desalination: A review. Chemical Engineering Journal, 2015. 281: p. 502-522.

92. Altaee, A., G. Zaragoza, and H.R. van Tonningen, Comparison between Forward Osmosis-Reverse Osmosis and Reverse Osmosis processes for seawater desalination. Desalination, 2014. 336: p. 50-57.

93. Achilli, A., T.Y. Cath, E.A. Marchand, and A.E. Childress, The forward osmosis membrane bioreactor: A low fouling alternative to MBR processes. Desalination, 2009. 239(1–3): p. 10-21.

94. Field, R.W. and J.J. Wu, Mass transfer limitations in forward osmosis: Are some potential applications overhyped? Desalination, 2013. 318: p. 118-124.

95. Zhao, S., L. Zou, C.Y. Tang, and D. Mulcahy, Recent developments in forward osmosis: Opportunities and challenges. Journal of Membrane Science, 2012. 396: p. 1-21.

96. McGinnis, R.L. and M. Elimelech, Energy requirements of ammonia–carbon dioxide forward osmosis desalination. Desalination, 2007. 207(1–3): p. 370-382.

97. Darwish, M.A., F. Al Asfour, and N. Al-Najem, Energy consumption in equivalent work by different desalting methods: case study for Kuwait. Desalination, 2003. 152(1–3): p. 83-92.

98. Ali Shoeb Moon, M.L., Energy Consumption in Forward Osmosis Desalination Compared to other Desalination Techniques. International Scholarly and Scientific Research & Innovation, 2012. 6(5): p. 515-517.

99. Kim, Y., M. Elimelech, H.K. Shon, and S. Hong, Combined organic and colloidal fouling in forward osmosis: Fouling reversibility and the role of applied pressure. Journal of Membrane Science, 2014. 460: p. 206-212.

100. Zou, S., Y.-N. Wang, F. Wicaksana, T. Aung, P.C.Y. Wong, A.G. Fane, and C.Y. Tang, Direct microscopic observation of forward osmosis membrane fouling by microalgae: Critical flux and the role of operational conditions. Journal of Membrane Science, 2013. 436: p. 174-185.

101. Chun, Y., F. Zaviska, E. Cornelissen, and L. Zou, A case study of fouling development and flux reversibility of treating actual lake water by forward osmosis process. Desalination, 2015. 357: p. 55-64.

102. Zhang, G., H. Yan, S. Ji, and Z. Liu, Self-assembly of polyelectrolyte multilayer pervaporation membranes by a dynamic layer-by-layer technique on a hydrolyzed polyacrylonitrile ultrafiltration membrane. Journal of Membrane Science, 2007. 292(1–2): p. 1-8.

103. Lee, S., C. Boo, M. Elimelech, and S. Hong, Comparison of fouling behavior in forward osmosis (FO) and reverse osmosis (RO). Journal of Membrane Science, 2010. 365(1–2): p. 34-39.

104. Boo, C., M. Elimelech, and S. Hong, Fouling control in a forward osmosis process integrating seawater desalination and wastewater reclamation. Journal of Membrane Science, 2013. 444: p. 148-156.

105. Fang, Y., L. Bian, Q. Bi, Q. Li, and X. Wang, Evaluation of the pore size distribution of a forward osmosis membrane in three different ways. Journal of Membrane Science, 2014. 454: p. 390-397.

106. Coday, B.D., P. Xu, E.G. Beaudry, J. Herron, K. Lampi, N.T. Hancock, and T.Y. Cath, The sweet spot of forward osmosis: Treatment of produced water, drilling wastewater, and other complex and difficult liquid streams. Desalination, 2014. 333(1): p. 23-35.

107. Lutchmiah, K., A.R.D. Verliefde, K. Roest, L.C. Rietveld, and E.R. Cornelissen, Forward osmosis for application in wastewater treatment: A review. Water Research, 2014. 58: p. 179-197.

108. Klaysom, C., T.Y. Cath, T. Depuydt, and I.F.J. Vankelecom, Forward and pressure retarded osmosis: potential solutions for global challenges in energy and water supply. Chemical Society Reviews, 2013. 42(16): p. 6959-6989.

109. Valladares Linares, R., Z. Li, M. Abu-Ghdaib, C.-H. Wei, G. Amy, and J.S. Vrouwenvelder, Water harvesting from municipal wastewater via osmotic gradient: An evaluation of process performance. Journal of Membrane Science, 2013. 447: p. 50-56.

110. Zhang, S., P. Wang, X. Fu, and T.-S. Chung, Sustainable water recovery from oily wastewater via forward osmosis-membrane distillation (FO-MD). Water Research, 2014. 52: p. 112-121.

111. William A. Phillip, J.S.Y., Menachem Elimelech, Reverse Draw Solute Permeation in Forward Osmosis: Modeling and Experiments. Environmental Science & Technology, 2010. 44(13): p. 5170–5176.

112. Kong, F.-x., H.-w. Yang, X.-m. Wang, and Y.F. Xie, Rejection of nine haloacetic acids and coupled reverse draw solute permeation in forward osmosis. Desalination, 2014. 341: p. 1-9.

113. Kim, T.-w., Y. Kim, C. Yun, H. Jang, W. Kim, and S. Park, Systematic approach for draw solute selection and optimal system design for forward osmosis desalination. Desalination, 2012. 284: p. 253-260.

114. Glew, D.N., Process for liquid recovery and solution concentration. US Patent 3,216,930 1965.

115. McCutcheon, J.R., R.L. McGinnis, and M. Elimelech, A novel ammonia—carbon dioxide forward (direct) osmosis desalination process. Desalination, 2005. 174(1): p. 1-11.

116. Sato, N., Y. Sato, and S. Yanase, Forward osmosis using dimethyl ether as a draw solute. Desalination, 2014. 349: p. 102-105.

117. Na, Y., S. Yang, and S. Lee, Evaluation of citrate-coated magnetic nanoparticles as draw solute for forward osmosis. Desalination, 2014. 347: p. 34-42.

118. Ling, M.M., K.Y. Wang, and T.-S. Chung, Highly Water-Soluble Magnetic Nanoparticles as Novel Draw Solutes in Forward Osmosis for Water Reuse. Industrial & Engineering Chemistry Research, 2010. 49(12): p. 5869-5876.

119. Ge, Q., J. Su, T.-S. Chung, and G. Amy, Hydrophilic Superparamagnetic Nanoparticles: Synthesis, Characterization, and Performance in Forward Osmosis Processes. Industrial & Engineering Chemistry Research, 2011. 50(1): p. 382-388.

120. Alnaizy, R., A. Aidan, and M. Qasim, Copper sulfate as draw solute in forward osmosis desalination. Journal of Environmental Chemical Engineering, 2013. 1(3): p. 424-430.

121. Alnaizy, R., A. Aidan, and M. Qasim, Draw solute recovery by metathesis precipitation in forward osmosis desalination. Desalination and Water Treatment, 2013. 51(28-30): p. 5516-5525.

122. Kravath, R.E. and J.A. Davis, Desalination of sea water by direct osmosis. Desalination, 1975. 16(2): p. 151-155.

123. Ling, M.M. and T.-S. Chung, Surface-Dissociated Nanoparticle Draw Solutions in Forward Osmosis and the Regeneration in an Integrated Electric Field and Nanofiltration System. Industrial & Engineering Chemistry Research, 2012. 51(47): p. 15463-15471.

124. Li, D., X. Zhang, J. Yao, G.P. Simon, and H. Wang, Stimuli-responsive polymer hydrogels as a new class of draw agent for forward osmosis desalination. Chem Commun (Camb), 2011. 47(6): p. 1710-2.

125. Hartanto, Y., S. Yun, B. Jin, and S. Dai, Functionalized thermo-responsive microgels for high performance forward osmosis desalination. Water Research, 2015. 70: p. 385-393.

126. Tyagi, H., A. Kushwaha, A. Kumar, and M. Aslam, A Facile pH Controlled Citrate-Based Reduction Method for Gold Nanoparticle Synthesis at Room Temperature. Nanoscale Research Letters, 2016. 11: p. 362.

127. Chen, M., Y. He, J. Huang, and J. Zhu, Investigation into Au nanofluids for solar photothermal conversion. International Journal of Heat and Mass Transfer, 2017. 108: p. 1894-1900.

128. Kumar, R.V. and G. Raza, Photocatalytic disinfection of water with Ag–TiO_2 nanocrystalline composite. Ionics, 2009. 15(5): p. 579-587.

129. Chen, H.-J. and D. Wen, Ultrasonic-aided fabrication of gold nanofluids. Nanoscale Research Letters, 2011. 6(1): p. 198.

130. Zhou, J.-H., Z.-J. Sui, J. Zhu, P. Li, D. Chen, Y.-C. Dai, and W.-K. Yuan, Characterization of surface oxygen complexes on carbon nanofibers by TPD, XPS and FT-IR. Carbon, 2007. 45(4): p. 785-796.

131. Van Thu, L., N. Cao Long, L. Quoc Trung, N. Trinh Tung, N. Duc Nghia, and V. Minh Thanh, Surface modification and functionalization of carbon nanotube with some organic compounds. Advances in Natural Sciences: Nanoscience and Nanotechnology, 2013. 4(3): p. 035017.

132. Massoumi, B., V. Badr-Valizad, and M. Jaymand, In situ chemical oxidative graft polymerization of aniline from phenylamine end-caped poly(ethylene glycol)-functionalized multi-walled carbon nanotubes. RSC Advances, 2015. 5(51): p. 40840-40848.

133. Baykal, A., S. Güner, and A. Demir, Synthesis and magneto-optical properties of triethylene glycol stabilized $Mn1-xZnxFe_2O_4$ nanoparticles. Journal of Alloys and Compounds, 2015. 619: p. 5-11.

134. D. Pavia, G.L., G. Kriz, J. Vyvyan, Introduction to Spectroscopy. 2008.

135. Lee, H.-M., H.-R. Kang, K.-H. An, H.-G. Kim, and B.-J. Kim, Comparative studies of porous carbon nanofibers by various activation methods. Carbon letters, 2013. 14(3): p. 180-185.

136. Vakili, M., S.M. Hosseinalipour, S. Delfani, and S. Khosrojerdi, Photothermal properties of graphene nanoplatelets nanofluid for low-temperature direct absorption solar collectors. Solar Energy Materials and Solar Cells, 2016. 152: p. 187-191.

137. Chen, L., J. Liu, X. Fang, and Z. Zhang, Reduced graphene oxide dispersed nanofluids with improved photo-thermal conversion performance for direct absorption solar collectors. Solar Energy Materials and Solar Cells, 2017. 163: p. 125-133.

138. Chen, M., Y. He, and J. Zhu, Preparation of Au–Ag bimetallic nanoparticles for enhanced solar photothermal conversion. International Journal of Heat and Mass Transfer, 2017. 114: p. 1098-1104.

139. Menbari, A., A.A. Alemrajabi, and A. Rezaei, Heat transfer analysis and the effect of CuO/Water nanofluid on direct absorption concentrating solar collector. Applied Thermal Engineering, 2016. 104: p. 176-183.

140. He, Q., S. Wang, S. Zeng, and Z. Zheng, Experimental investigation on photothermal properties of nanofluids for direct absorption solar thermal energy systems. Energy Conversion and Management, 2013. 73: p. 150-157.

141. Saidur, R., T.C. Meng, Z. Said, M. Hasanuzzaman, and A. Kamyar, Evaluation of the effect of nanofluid-based absorbers on direct solar collector. International Journal of Heat and Mass Transfer, 2012. 55(21–22): p. 5899-5907.

142. Yousefi, T., E. Shojaeizadeh, F. Veysi, and S. Zinadini, An experimental investigation on the effect of pH variation of MWCNT–H_2O nanofluid on the efficiency of a flat-plate solar collector. Solar Energy, 2012. 86(2): p. 771-779.

143. Sadr, R., C. Hohenegger, H. Li, P.J. Mucha, and M. Yoda, Diffusion-induced bias in near-wall velocimetry. Journal of Fluid Mechanics, 2007. 577: p. 443-456.

144. Sadr, R., M. Yoda, Z. Zheng, and A.T. Conlisk, An experimental study of electro-osmotic flow in rectangular microchannels. Journal of Fluid Mechanics, 2004. 506: p. 357-367.

145. Zhang, H., H.-J. Chen, X. Du, G. Lin, and D. Wen, Dependence of Photothermal Conversion Characteristics on Different Nanoparticle Dispersions. Journal of Nanoscience and Nanotechnology, 2015. 15(4): p. 3055-3060.

146. Jin, H., G. Lin, L. Bai, M. Amjad, E.P. Bandarra Filho, and D. Wen, Photothermal conversion efficiency of nanofluids: An experimental and numerical study. Solar Energy, 2016. 139: p. 278-289.

147. Jin, H., G. Lin, L. Bai, A. Zeiny, and D. Wen, Steam generation in a nanoparticle-based solar receiver. Nano Energy.

148. Wen, D., Intracellular hyperthermia: Nanobubbles and their biomedical applications. International Journal of Hyperthermia, 2009. 25(7): p. 533-541.

149. Picknett, R.G. and R. Bexon, The evaporation of sessile or pendant drops in still air. Journal of Colloid and Interface Science, 1977. 61(2): p. 336-350.

150. Hong, S.-J., T.-H. Chou, Y.-Y. Liu, Y.-J. Sheng, and H.-K. Tsao, Advancing and receding wetting behavior of a droplet on a narrow rectangular plane. Colloid and Polymer Science, 2013. 291(2): p. 347-353.

151. Zhang, C., X. Zhu, and L. Zhou, Morphology tunable pinning force and evaporation modes of water droplets on PDMS spherical cap micron-arrays. Chemical Physics Letters, 2011. 508(1–3): p. 134-138.

152. Wang, F.-C. and H.-A. Wu, Pinning and depinning mechanism of the contact line during evaporation of nano-droplets sessile on textured surfaces. Soft Matter, 2013. 9(24): p. 5703-5709.

153. Ghasemi, H., G. Ni, A.M. Marconnet, J. Loomis, S. Yerci, N. Miljkovic, and G. Chen, Solar steam generation by heat localization. Nat Commun, 2014. 5.

154. Neumann, O., C. Feronti, A.D. Neumann, A. Dong, K. Schell, B. Lu, E. Kim, M. Quinn, S. Thompson, N. Grady, P. Nordlander, M. Oden, and N.J. Halas, Compact solar autoclave based on steam generation using broadband light-harvesting nanoparticles. Proc Natl Acad Sci USA, 2013. 110(29): p. 11677-81.

155. Ni, G., N. Miljkovic, H. Ghasemi, X. Huang, S.V. Boriskina, C.-T. Lin, J. Wang, Y. Xu, M.M. Rahman, T. Zhang, and G. Chen, Volumetric solar heating of nanofluids for direct vapor generation. Nano Energy, 2015. 17: p. 290-301.

156. Neumann, O., A.S. Urban, J. Day, S. Lal, P. Nordlander, and N.J. Halas, Solar vapor generation enabled by nanoparticles. ACS Nano, 2013. 7(1): p. 42-9.

157. Fang, Z., Y.-R. Zhen, O. Neumann, A. Polman, F.J. García de Abajo, P. Nordlander, and N.J. Halas, Evolution of Light-Induced Vapor Generation at a Liquid-Immersed Metallic Nanoparticle. Nano Letters, 2013. 13(4): p. 1736-1742.

158. Lukianova-Hleb, E., Y. Hu, L. Latterini, L. Tarpani, S. Lee, R.A. Drezek, J.H. Hafner, and D.O. Lapotko, Plasmonic nanobubbles as transient vapor nanobubbles generated around plasmonic nanoparticles. ACS Nano, 2010. 4(4): p. 2109-2123.

159. Jin, H., G. Lin, L. Bai, A. Zeiny, and D. Wen, Steam generation in a nanoparticle-based solar receiver. Nano Energy, 2016. 28: p. 397-406.

160. Baffou, G., J. Polleux, H. Rigneault, and S. Monneret, Super-heating and micro-bubble generation around plasmonic nanoparticles under cw illumination. Journal of Physical Chemistry C, 2014. 118(9): p. 4890-4898.

161. Carlson, M.T., A.J. Green, and H.H. Richardson, Superheating water by CW excitation of gold nanodots. Nano Letters, 2012. 12(3): p. 1534-1537.

162. Lombard, J., T. Biben, and S. Merabia, Kinetics of Nanobubble Generation Around Overheated Nanoparticles. Physical Review Letters, 2014. 112(10): p. 105701.

163. Hogan, N.J., A.S. Urban, C. Ayala-Orozco, A. Pimpinelli, P. Nordlander, and N.J. Halas, Nanoparticles heat through light localization. Nano Letters, 2014. 14(8): p. 4640-4645.

164. Liu, G., J. Xu, and K. Wang, Solar water evaporation by black photothermal sheets. Nano Energy, 2017. 41: p. 269-284.

165. Xu, J., C. Tang, Y. Cheng, Z. Li, H. Cao, X. Yu, Y. Li, and Y. Wang, Design, Construction, and Characterization of an Adjustable 70 kW High-Flux Solar Simulator. Journal of Solar Energy Engineering, 2016. 138(4): p. 041010-041010.

166. McGinnis, R.L., N.T. Hancock, M.S. Nowosielski-Slepowron, and G.D. McGurgan, Pilot demonstration of the NH_3/CO_2 forward osmosis desalination process on high salinity brines. Desalination, 2013. 312: p. 67-74.

167. McCutcheon, J.R., R.L. McGinnis, and M. Elimelech, Desalination by ammonia–carbon dioxide forward osmosis: Influence of draw and feed

solution concentrations on process performance. Journal of Membrane Science, 2006. 278(1–2): p. 114-123.

168. Nguyen, H.T., S.-S. Chen, N.C. Nguyen, H.H. Ngo, W. Guo, and C.-W. Li, Exploring an innovative surfactant and phosphate-based draw solution for forward osmosis desalination. Journal of Membrane Science, 2015. 489: p. 212-219.

169. Roy, D., M. Rahni, P. Pierre, and V. Yargeau, Forward osmosis for the concentration and reuse of process saline wastewater. Chemical Engineering Journal, 2016. 287: p. 277-284.

170. Ge, Q., F. Fu, and T.-S. Chung, Ferric and cobaltous hydroacid complexes for forward osmosis (FO) processes. Water Research, 2014. 58: p. 230-238.

171. Phuntsho, S., H.K. Shon, S. Hong, S. Lee, S. Vigneswaran, and J. Kandasamy, Fertiliser drawn forward osmosis desalination: the concept, performance and limitations for fertigation. Reviews in Environmental Science and Bio/Technology, 2012. 11(2): p. 147-168.

172. Hau, N.T., S.-S. Chen, N.C. Nguyen, K.Z. Huang, H.H. Ngo, and W. Guo, Exploration of EDTA sodium salt as novel draw solution in forward osmosis process for dewatering of high nutrient sludge. Journal of Membrane Science, 2014. 455: p. 305-311.

173. Nguyen, H.T., N.C. Nguyen, S.-S. Chen, H.H. Ngo, W. Guo, and C.-W. Li, A new class of draw solutions for minimizing reverse salt flux to improve forward osmosis desalination. Science of The Total Environment, 2015. 538: p. 129-136.

174. Zhao, P., B. Gao, Q. Yue, J. Kong, H.K. Shon, P. Liu, and Y. Gao, Explore the forward osmosis performance using hydrolyzed polyacrylamide as draw solute for dye wastewater reclamation in the long-term process. Chemical Engineering Journal, 2015. 273: p. 316-324.

175. Dey, P. and E.L. Izake, Magnetic nanoparticles boosting the osmotic efficiency of a polymeric FO draw agent: Effect of polymer conformation. Desalination, 2015. 373: p. 79-85.

176. Dey, P. and E.L. Izake, Mixed Polymer-Coated Magnetic Nanoparticles as Forward Osmosis Draw Agents of Tuned Hydrophilicity. Chemistry – A European Journal, 2016. 22(32): p. 11253-11260.

177. Mino, Y., D. Ogawa, and H. Matsuyama, Functional magnetic particles providing osmotic pressure as reusable draw solutes in forward osmosis membrane process. Advanced Powder Technology, 2016. 27(5): p. 2136-2144.

178. Park, S.Y., H.-W. Ahn, J.W. Chung, and S.-Y. Kwak, Magnetic core-hydrophilic shell nanosphere as stability-enhanced draw solute for forward osmosis (FO) application. Desalination, 2016. 397: p. 22-29.

179. Zhao, Q., N. Chen, D. Zhao, and X. Lu, Thermoresponsive Magnetic Nanoparticles for Seawater Desalination. ACS Applied Materials & Interfaces, 2013. 5(21): p. 11453-11461.

180. Ge, Q., L. Yang, J. Cai, W. Xu, Q. Chen, and M. Liu, Hydroacid magnetic nanoparticles in forward osmosis for seawater desalination and efficient regeneration via integrated magnetic and membrane separations. Journal of Membrane Science, 2016. 520: p. 550-559.

181. Hoover, L.A., W.A. Phillip, A. Tiraferri, N.Y. Yip, and M. Elimelech, Forward with Osmosis: Emerging Applications for Greater Sustainability. Environmental Science & Technology, 2011. 45(23): p. 9824-9830.

182. Rasouli, M., Basic concepts and practical equations on osmolality: Biochemical approach. Clinical Biochemistry, 2016. 49(12): p. 936-941.

183. Guo, C.X., D. Zhao, Q. Zhao, P. Wang, and X. Lu, Na^{+}-functionalized carbon quantum dots: a new draw solute in forward osmosis for seawater desalination. Chem Commun (Camb), 2014. 50(55): p. 7318-21.

184. Zhao, D., S. Chen, C. Guo, Q. Zhao, and X. Lu, Multi-functional Forward Osmosis Draw Solutes for Seawater Desalination. Chinese Journal of Chemical Engineering, 2016.

185. Świergiel, J. and J. Jadżyn, Structure of hydrogen bonded supramolecular self-assembles controlled by the structure of monomers: 1,1- and 1,3-diethylureas. Reactive and Functional Polymers, 2016. 105: p. 129-133.

186. Bai, H., Z. Liu, and D.D. Sun, Highly water soluble and recovered dextran coated Fe_3O_4 magnetic nanoparticles for brackish water desalination. Separation and Purification Technology, 2011. 81(3): p. 392-399.

187. Qasim, M., F. Mohammed, A. Aidan, and N.A. Darwish, Forward osmosis desalination using ferric sulfate draw solute. Desalination, 2017. 423: p. 12-20.

188. Walton, N.R.G., Electrical Conductivity and Total Dissolved Solids—What is Their Precise Relationship? Desalination, 1989. 72(3): p. 275-292.

189. WHO, Guidelines for drinking-water quality. 2017, World Health Organization, Switzerland.